A Study on Wideband/Multiband Analog Front-end Components for Wireless Communication Systems

January 2009

Shingo Tanaka

Contents

List of Figures

List of Tables

Abstract

In the field of wireless communications, multiband/wideband handsets are in great demand. One background to this demand is that many wireless communication systems that use different frequency ranges have been already installed. The software defined radio and cognitive radio architectures are expected to accelerate the introduction of multimode terminals. Another background to this demand is the increase in data transmitted. High speed data transmission is being demanded from wireless communication systems so the bandwidth of each system is expected to increase. In order to realize high speed data transmission, analog front-end circuits with excellent linearity is a key demand.

Despite the obvious need, analog front-end components including antennas, switches, divider/combiners, amplifiers and so on, have been basically designed for operation at a single frequency with narrow frequency band. Moreover, wireless communication systems are still using many non-linear (active) devices, and their distortion triggers in-band and out-of-band spurious components. Given these facts, therefore, the research and development of multiband/wideband analog front-end components with high-linearity is strongly needed.

In this dissertation, several key analog front-end components for multiband/wideband operation and high-linearity are proposed. First, studies on wideband/multiband antenna and switches are described and discussed in Chapters 2 and 3. Next, studies on radio-on-fiber links for wideband and high speed transmission are described and discussed in Chapters 4, 5 and 6.

Chapter 1 introduces the background to and motivation of this study on wideband/multiband analog front-end components with high linearity.

Chapter 2 proposes single-pole double-throw switches composed of pin diodes for multi-band operation. Isolation greater than 20 dB and insertion loss under 2 dB are achieved in experiments at three frequency bands: 1.6 GHz, 2.5 GHz, and 5.8 GHz. Ladder circuit configuration instead of conventional compensating inductance realizes multiband operation.

Chapter 3 proposes wideband folded dipole antennas. An experimental result focusing on 1.7 GHz for 50 ohm impedance matching shows an antenna prototype with bandwidth of over 55 % (VSWR $\leq$ 2). The gain values of the antenna are basically constant (2 dBi) in this frequency band and the radiation patterns are very similar to those of a normal dipole antenna. Ground plane of conventional folded

loop antenna is removed while maintaining wideband property.

In Chapter 4, a predistortion type equi-path linearizer is created for an RoF system based on W-CDMA. Experimental and calculated results agree well, and more than 20 dB improvement in the third order intermodulation components is obtained over the bandwidth of 60 MHz. The optical circuit and control circuit are more simplified than the conventional feedforward technique.

In Chapter 5, three distortion reduction filters for RoF systems are proposed and evaluated from the standpoint of improving the in-band third order intermodulation (IM3) components (spurious components), insertion loss, temperature stability and so on. The RF comb filter and RF-DBRF can reduce the IM3 components by more than 20 dB and noise level by more than 3 dB. These filters can be applied to wideband system and do not need control circuit.

In Chapter 6, in order to realize a balanced RF interface at the input, an RoF link with a dual-drive Mach-Zender modulator as a wideband balan is proposed. An experiment using mixed-mode S parameters shows that the proposed arrangement offers common mode rejection ratio of at least 15 dB and insertion loss of 41 ± 2 dB from 20 MHz to 6 GHz (bandwidth $\approx$ 199 %). Furthermore, the addition of an erbium-doped fiber amplifier improves the performance (CMRR over 30 dB and insertion loss of 8 ± 2 dB).

Finally, this dissertation is concluded in Chapter 7, with the summery of each chapter and future prospects.

Chapter 1

General Introduction

1.1 Background of This Study

The field of wireless communications is being driven by strong demand for multiband/wideband handsets that can support several wireless communication systems [1.1][1.2]. The background to this demand is the acknowledgment of the many dedicated wireless communication systems that have been established in different frequency ranges. Given the continued growth in personal mobility, it is impractical to carry one each of the handsets needed to access all the systems; the optimum approach is to integrate all the handsets into one multimode terminal. Recent research advances such as software defined radio and cognitive radio architectures are expected to accelerate the introduction of multimode terminals [1.3]–[1.5]. A key stumbling block is, however, the poor performances of analog front-end components including antennas, switches, divider/combiners, and amplifiers. Existing devices were basically designed for operation at a single frequency within a narrow frequency band [1.6][1.7].

Another trend is the continued increase in the amount of transmitted data. The emergence of new services, especially video-based services, is driving rapid increases in the data transmission rates demanded of wireless communication systems, as some examples of required bandwidth and data transmission rate are summerized on Table 1.1. In order to realize high speed data transmission, the analog front-end circuits must be highly linear. However, current wireless communication systems contain so many non-linear (active) devices used for wireless communication systems, that the resulting distortion triggers excessive levels of in-band and out-of-band spurious components [1.8].

Against this background, therefore, effective research and development efforts leading to multiband/wideband analog front-end components with high-linearity are urgently needed. It may be said that the performance of multiband/wideband wireless communication systems is now mainly dependent on the performances of the analog front-end components.

Table 1.1: Examples of required bandwidth and data transmission rate.

	Required bandwidth [MHz]	Transmission rate [Mb/s]
2G (GSM1993)	0.2	0.104
3G (WCDMA)	5	0.384
WiMAX	20	96

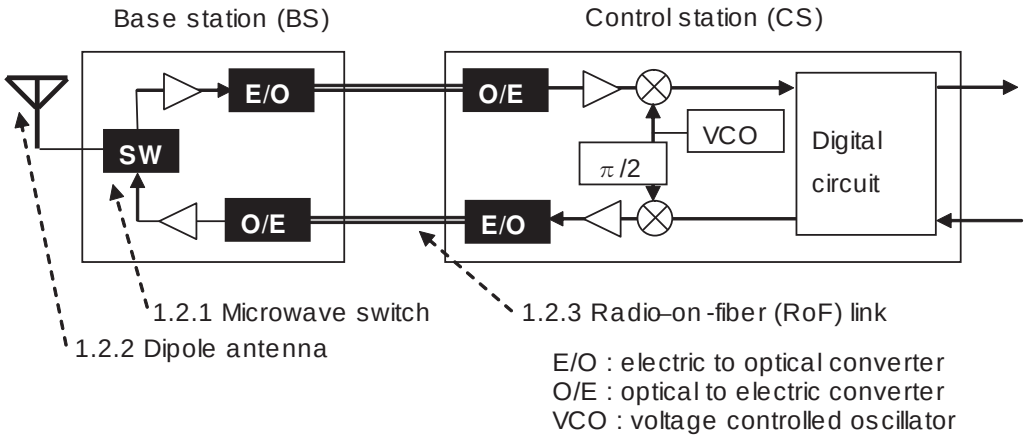

Figure 1.1: Example of system block diagram for radio-on-fiber wireless communication systems

1.2 Purpose and Position of This Study

This section provides a general overview of analog front-end components for a radio-on-fiber (RoF) wireless system as shown in Fig.1.1. The purpose and position of our proposals for multiband/wideband operation components are shown together with the results of past studies and their problems. The components consist of microwave switches, dipole antennas, and RoF links. As is described in Section 1.2.3 in detail, RoF systems have two merits. The one is the system expandability realized by the low insertion loss of optical fiber, and the other is that RoF systems can support precise electromagnetic field measurements. An example of a system block diagram for RoF wireless communication systems with these components is shown in Fig.1.1. The problems of existing research and effect of this research are summerized on Table 1.2.

Table 1.2: The problems of existing research and effect of this research.

Chapter 2 (1.2.1)	Target	Realization of multiband RF switch by PIN diode.
	Problems of existing research	Only effective near a single resonance frequency. Miniaturization of CP value by MMIC enables wideband operation, but this technique is not effective at higher frequency.
	Proposed method	Ladder circuit is introduced in order to obtain multi-pararell resonances. Semi-microstrip configuration for frequency variation reduction is also proposed.
	Effect of proposed research	Multiband operation is realized with PIN diode. Design method for bandwidth control is also proposed. Frequency variation is reduced to around 25% by semi-microstrip configuration.
Chapter 3 (1.2.2)	Target	Realization of wideband omni-directional antenna.
	Problems of existing research	Dipole is not suitable for wideband operation. Folded loop with ground plane do not have omni-directional radiation pattern nor self-balanced
	Proposed method	Wideband folded loop and folded dipole antenna without ground plane. Wideband impedance matching is realized by parameter value studies.
	Effect of proposed research	values distribution for wideband operation is shown. The mechanism of wideband opearation is clarified. Wideband self-balanced property is also obtained.
Chapter 4 (1.2.3)	Target	Realization of linearizer for Radio-on-Fiber(RoF) with simple optical circuit, simple control circuit, and large improvement in IM3.
	Problems of existing research	Feedforward technique requires large optical circuits (but large improvement in IM3). Diode predistortion technique offers less improvement in IM3 than feedforward (but circuit is simple). Both techniques need complex control circuits to handle temperature changes.
	Proposed method	Predistortion type equi-path linearizer is applied to RoF. Phase shifters and pre-amplifiers are newly added for optimized operation.
	Effect of proposed research	IM3 improvement more than 20dB is realized with simple optical circuit. Control circuit is also simplified. Addition of pre-amplier can save power consumption. It is found that the IM3 components of LD is shifted by around 90 degrees, so phase shifters are added.
Chapter 5 (1.2.3)	Target	Realization of simpler distortion cancellation technique for Radio-on-Fiber(RoF) than that proposed in Chapter 4.
	Problems of existing research	Optical circuit is simplified but RF circuit is still large. Simple control circuit is still needed.
	Proposed method	Filter techniques (optical comb, RF comb, RF-dual band rejection filter (DBRF)) are applied and compared.
	Effect of proposed research	RF circuits are more simplified than method in Chapter 4. No control circuit is needed. Effective even in the saturation region. Suitable for wideband system. Three filters are compared. Especially, RF comb and RF-DBRF can reduce IM3 more than 20 dB and insertion loss is under 2 dB for bandwidth with 100 MHz.
Chapter 6 (1.2.3)	Target	Realization of wideband balun of Radio-on-Fiber (RoF) link.
	Problems of existing research	Difficult to realize wideband balun.
	Proposed method	Dual-drive Mach-Zender modulator (DD-MZM) is applied.
	Effect of proposed research	Wideband balun is realized. Addition of erbium-doped fiber amplifier (EDFA) improved the performance. The optimum received light powers at photo diodes are studied.

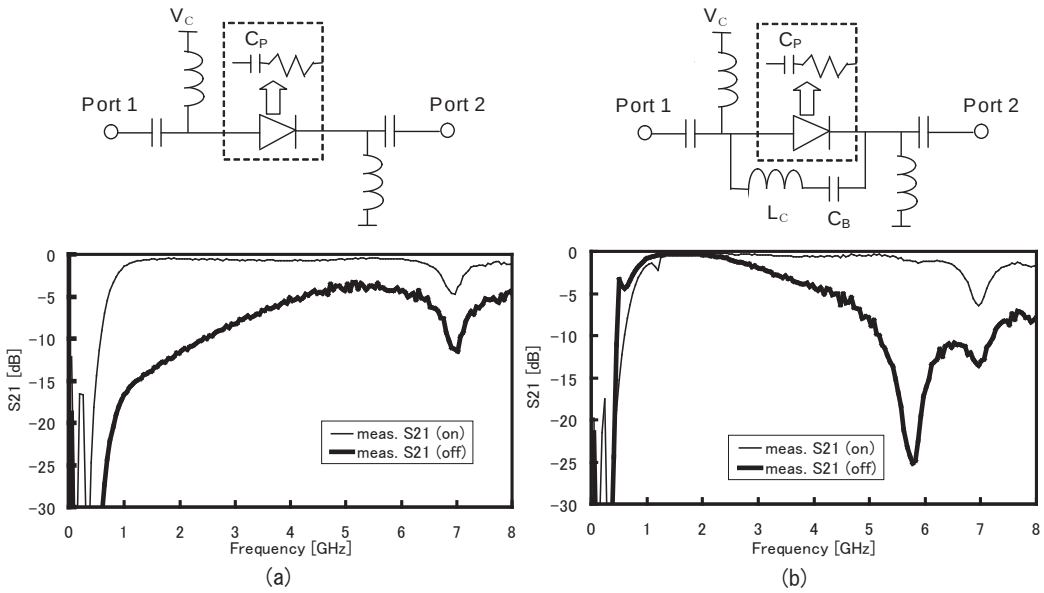

Figure 1.2: Circuit configuration and measured S_{21} of SPST pin diode switch in on/off states, (a) without compensating inductor and (b) with compensating inductor.

1.2.1 Microwave Switches

The microwave switch is one of three key control circuits used extensively for controlling signal flow at microwave frequencies. A pin diodes, which have an intrinsic or i-region between p- and n-type contact regions, and GaAs metal-semiconductor field effect transistors (MESFETs) are the most commonly employed devices for microwave switches. In both cases, the parasitic capacity (C_P) of the device in the off state decreases the isolation of the switch at high frequencies [1.6]. Figure 1.2(a) shows the circuit configuration and the measured S_{21} (S parameter that represents transmission characterisctics from port 1 to port 2) of a single-pole single-throw (SPST) switch employing a commercially available pin diode with C_P value of 0.35pF [1.9]. In the case of the SPST switch, the switch is in the on (off) state when control voltage (V_C) is high (low), and vice versa. As is shown in Fig.1.2(a), the isolation of the switch in the off state is under 10dB if the signal frequency is higher than 3GHz. The standard single band switch [1.6] uses a compensating inductance (L_C) to form a parallel resonant circuit with C_P. Figure 1.2(b) shows the circuit configuration and S_{21} of the standard single band switch with the same pin diode, designed for 5.8GHz application. C_B is a DC blocking capacitor. However, as is found in Fig.1.2(b), this technique is only effective near a single resonance frequency. For example, the isolation at 1-2GHz is degraded compared to the performance without L_C.

Several studies have tried to obtain wideband switches in the presence of the

limitation caused by C_P[1.10][1.11]. Recent commercial wideband switches cover the DC-6GHz range [1.12][1.13]. These switches, employ monolithic microwave integrated circuit (MMIC) technologies to minimize the value of C_P, which makes them are much more expensive than switches that use discrete circuit elements. As the C_P value is small, but not zero, these approaches become ineffective at high operation frequencies.

In Chapter 2 of this dissertation, we propose a pin diode switch that can operate efficiently at multiple frequencies. The ladder circuit [1.14] introduced here has a simple configuration, which lowers the manufacturing cost significantly. The circuit configuration and the design method are described in Chapter 2.2. Two examples of fabricated switches are described in Chapter 2.3; one is made of all lumped elements (Section 2.3.1) while the other employs a microstrip planar circuit configuration (Section 2.3.2). The latter offers more stable resonance characteristics than the former and so permits mass production. Performance reproducibility of those two types of switches will be investigated in detail. In addition, the temperature characteristics, the switching speed, and the signal distortion characteristics of the switches are investigated in Section 2.3.3. A higher isolation switch is also investigated for SPST dual band use in Section 2.3.4.

1.2.2 Dipole Antennas

The most basic antenna configuration is the half-wavelength dipole antenna [1.7][1.15][1.16]. It was used in the first wireless electromagnetic system demonstrated by Professor Heinrich Rudolph Hertz in 1886 [1.7]. The radiation of this antenna is caused by half-wavelength resonance, so the bandwidth is as narrow as a few percent. Figure 1.3 shows the construction of a half-wavelength dipole antenna and its simulated voltage standing wave ratio (VSWR). When width w=0.2mm and VSWR is under 2, the bandwidth is around 5 %. In order to obtain wider bandwidth, dipoles with cylindrical or wide elements are used. Figure 1.3(b) also shows the simulated VSWR of a dipole antenna with wide elements. It is observed that this arrangement increases the bandwidth when element width is increased. However, the maximum bandwidth obtained with this technique is about 15 %. The biconical or bow-tie antenna has much wider bandwidth due to its self-complimentary construction, but its characteristic impedance is much greater than the 50 ohms normally used when designing analog front-end components.

In the field of antennas for mobile handsets, a dipole based antenna with bandwidth of more than 40 % has been reported [1.17]. Figure 1.4 shows the antenna configuration and its measured and simulated VSWRs. Named the folded loop antenna, it is basically constructed by folding the ends of a folded dipole antenna [1.18]–[1.20]. The antenna includes a ground plane, as it is intended for mobile handset use. In this case, the ground plane decreases the antenna's impedance, but the the folded dipole construction counters this decrease. Since the ground plane must be placed near the antenna elements, the antenna fails to offer omnidirectional use.

The folded dipole antenna is known to have self-balanced characteristics. This

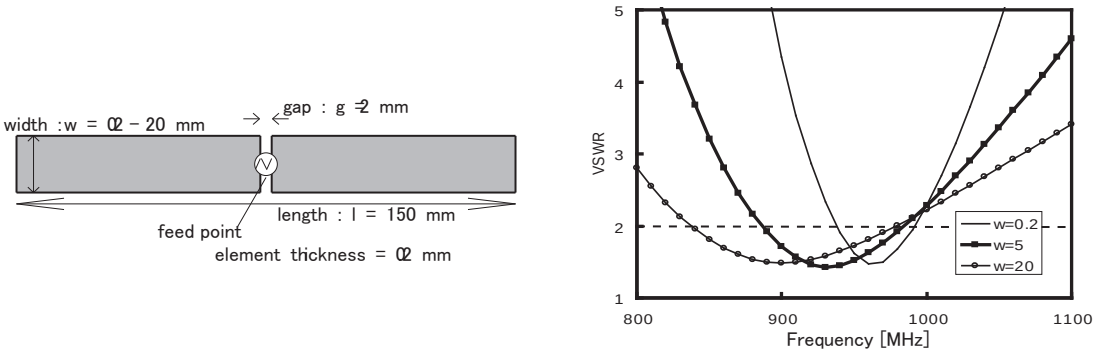

Figure 1.3: Half-wavelength dipole antennas; (a) construction, (b) simulated VSWRs for various w values.

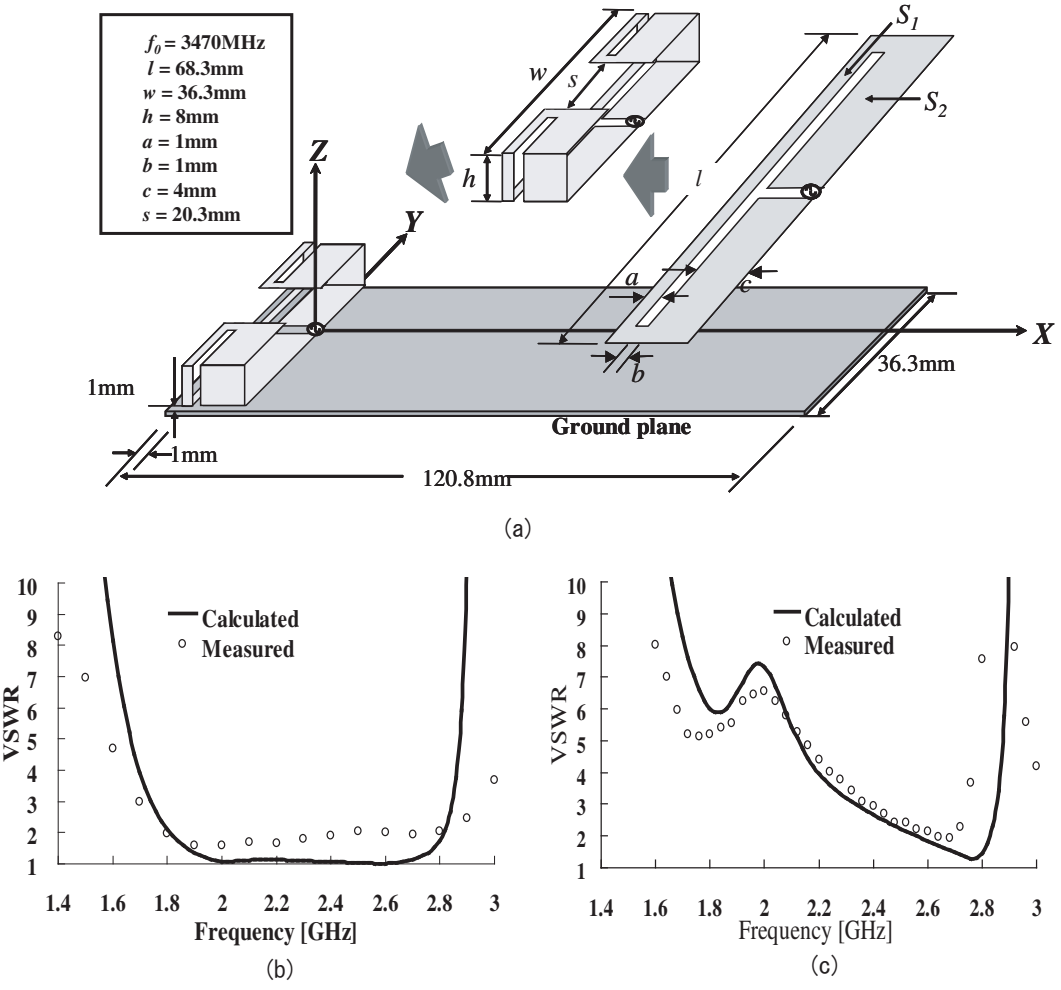

Figure 1.4: Folded loop antenna for handsets; (a) construction, (b) measured and simulated VSWRs with balanced feed, (c) measured and simulated VSWRs with unbalanced feed.

makes it unnecessary to use a balun (the interface between antenna and coaxial feed line that converts balanced mode to unbalanced mode), unlike the normal dipole antenna. However, in case of the wideband folded loop antenna, the self-balanced characteristics are observed only in a narrow band, so a balun is still needed for wideband operation, as shown in Figs.1.4(b)(c) [1.17].

The goal of Chapter 3 of this dissertation is to remove the ground plane from the wideband folded loop antenna in handset use, while still maintaining wideband characteristics. This advance is described in Chapter 3.2. The antenna configuration of the folded loop antenna with folded elements is then simplified, that is, the folding parts at both ends of the element are removed, while still maintaining the original wideband properties. This advance is described in Chapter 3.3. With this modification, the antenna can be planar and so easy to assemble. Balanced and unbalanced feeds are evaluated in order to examine the self-balanced properties.

1.2.3 Radio-on-Fiber (RoF) Links

Radio-on-fiber (RoF) technology involves modulating an optical carrier with a microwave subcarrier for distribution over a fiber network. The configuration of an RoF system is shown in Fig.1.5. The loss of optical fiber (0.2dB/km at 1.55μm=193THz) is much smaller than that of coaxial cable (around 9dB/m at 60GHz), so middle/long distance transmission is available. Recently, RoF links are used for mobile communication systems that must cover areas with weak radio power, e.g. inside tunnels, buildings or underground shopping areas. RoF links are also used for precise antenna measurements, as the effect of RoF link interferes much less with the measured electric field than conventional coaxial cable [1.21]–[1.23].

Linearizers for Radio-on-Fiber (RoF) Links

RoF links can transmit several wideband microwave subcarriers simultaneously, however, data transmission speed and distance depend on their dynamic range. The dynamic range of an RoF link is mainly determined by its third order distortion and noise characteristics. The distortion is mainly caused by the laser diode (LD) used as the E/O (electric to optical) converter, in the microwave frequency range. Therefore, various linearization techniques have been created to reduce the nonlinear distortion generated by the use of LDs. The circuit configuration of the feedforward technique, as applied to an RoF link, is shown in Fig.1.6(a). With this technique, at the 1st loop, the signal without distortion and the signal after the LD are combined with opposite phase so only distortion components are obtained. At the 2nd loop, the distortion components and the signal after the LD (with distortion) are combined with opposite phase yielding the signal without distortion. The feedforward technique is superior since it offers a large improvement in the third order intermodulation (IM3) components and less intensity noise [1.24][1.25]. However, it has a drawback in that

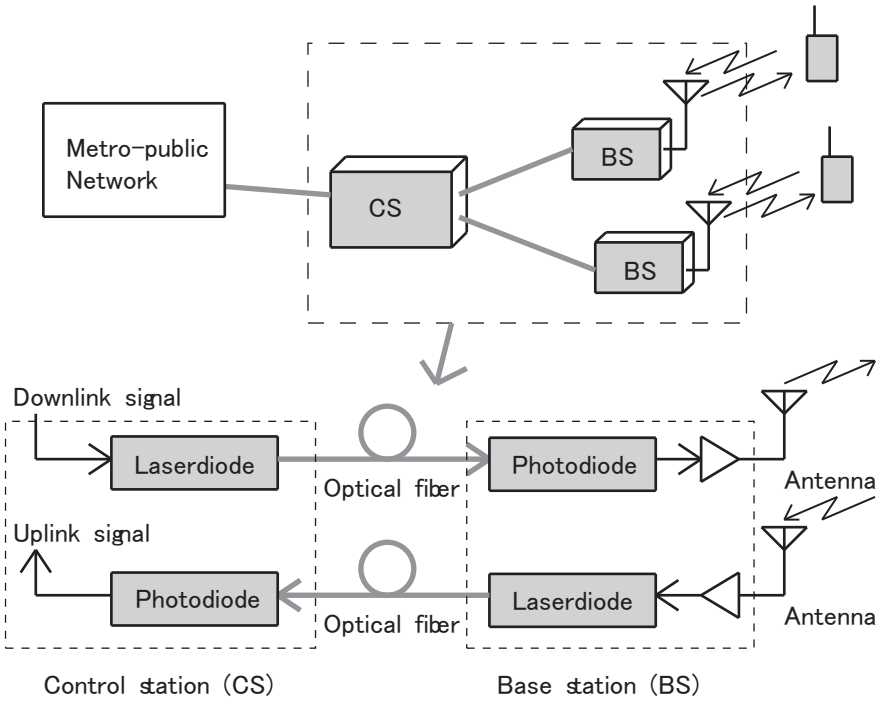

Figure 1.5: Configuration of radio-on-fiber (RoF) system

it requires additional optical components such as LD, photodiode (PD), and optical couplers.

The circuit configuration of the diode predistortion technique,as applied to an RoF link, is shown in Fig.1.6(b). With this technique, the diode circuit placed in front of the LD generates distortion with opposite phase (signal predistortion). By tuning the signal level with amplifiers, the distortion of the LD signal with distortion is cancelled by the predistortion. Predistortion with diodes is a simple approach but it offers less improvement in IM3 components than the feedforward technique [1.26][1.27]. Moreover, these techniques need complex control circuits to handle the temperature changes expected and these circuits consume a lot of power [1.8][1.28]. There is strong demand for a linearizer that has a simple optical circuit configuration, a minimal control circuit, and a large improvement in IM3 components.

Chapter 4 of this dissertation proposes an RoF link with a predistortion type equi-path (PTEP) linearizer [1.29]. The PTEP linearizer uses predistortion and demonstrates good temperature characteristics without a control circuit. As an example, the linearizer is combined with a Fabry-Perot LD for a W-CDMA RoF system. Fabry-Perot LDs are cost-effective but their distortion characteristics are worse than those of distributed feedback (DFB) LDs. Section 4.2 describes the circuit configuration and design method of the PTEP linearizer for an RoF system. Experiments on a linearizer with two types of LDs are presented in Section 4.3; one is Fabry-Perot LD

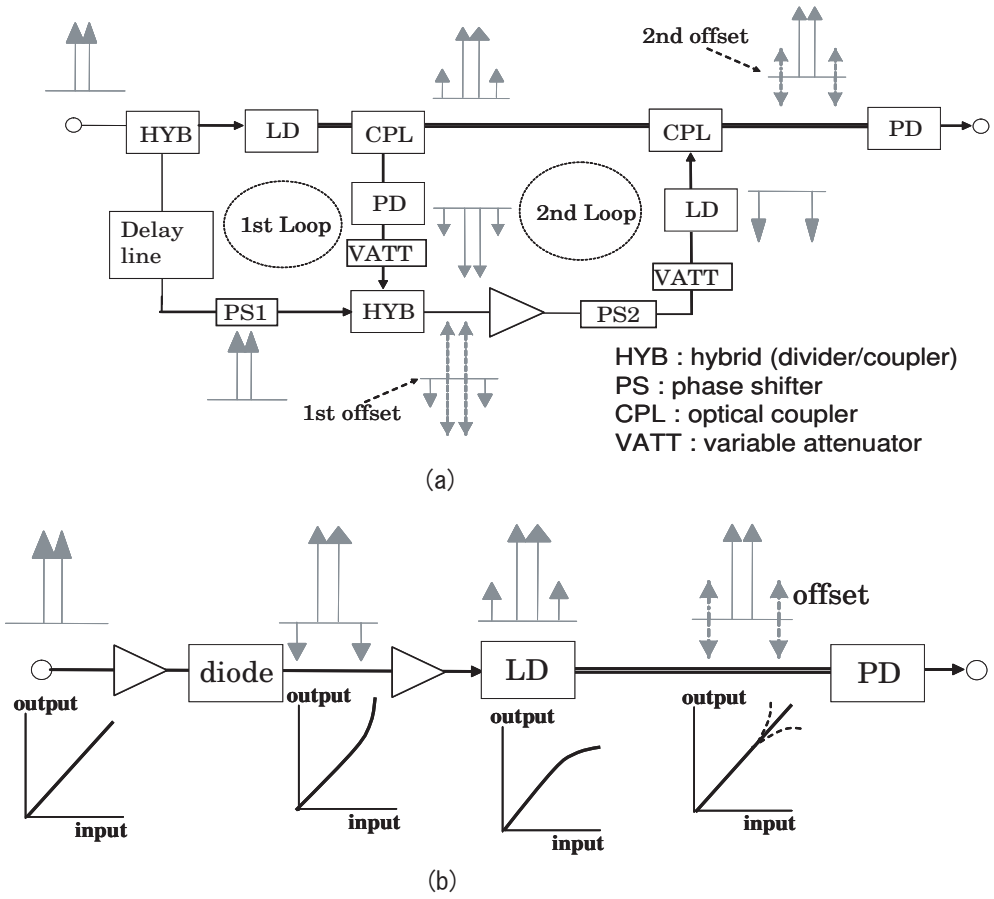

Figure 1.6: Circuit configuration (a) feedforward technique and (b) diode predistortion technique applied to radio-on-fiber (RoF) system.

and the other is a DFB-LD. The observed phase shift between the carrier and the IM3 component seen with both types of LDs is discussed in Section 4.4.

Chapter 5 of this dissertation proposes distortion reduction filters for RoF systems. Filtering techniques that use all-passive devices are shown to reduce the circuit size and effective in supporting to wideband systems like ultra wideband (UWB) systems [1.30]. The circuit configuration and design method of three kinds of filter, optical comb filter [1.31] based on the interferometer configuration [1.32][1.33], radio frequency (RF) comb filter, and RF dual band rejection filter (RF-DBRF) [1.34] are described and compared in Section 5.2. RoF links with these filters are then evaluated and compared in Section 5.3, from the standpoint of their improvement in IM3 components, insertion loss, noise level, temperature stability and so on. A comparison of the techniques is summarized in Table 1.3.

Table 1.3: Comparison between feedforward, diode predistortion, predistortion type equi-path, distortion reduction filter techniques applied to radio-on-fiber link.

techniques	Feedforward	Diode predistortion	Predistortion type equi-path	Distortion reduction filter
circuit scale	large	small	middle	small
improvement in IM3	large ($\geq$ 30dB)	small ($\approx$ 10dB)	middle ($\approx$ 20dB)	large ($\geq$ 30dB)
needed control circuit	large size	large size	simple	no need
effect on in-band spurious	effective	effective	effective	not effective
noise reduction	effective	not effective	not effective	effective

Wideband Balun for Radio-on-Fiber (RoF) Links

RoF links have RF input (E/O) and output (O/E) ports, and most ports are unbalanced (single-ended). However, in the RF circuit field, balanced ports are often used for microwave communication systems, e.g., mobile phone terminals [1.35]. Even systems in the millimeter wave region have started to adopt balanced ports [1.36]. In another important trend, RoF systems are also being used in precise electric field measurement systems as they can reduce measurement distortion and realize long distance transmission [1.37]. Many of the antennas in commercial use have balanced ports (e.g. the dipole antenna described in Chapter 1.2.2). These facts confirm that baluns are needed between balanced RF devices and RoF systems.

There are many kinds of baluns, e.g. bazooka balun, and quarter wavelength coaxial balun, etc. Unfortunately, these baluns operate in a single narrow frequency band as they based on resonance [1.7][1.15][1.16]. Figure 1.7(a) shows the circuit configuration of the rat-race coupler [1.38] used as a balun. In this case, the rat-race coupler is designed for use in the 2 GHz band so the length of each transmission line is are determined by wavelength λ at 2 GHz. One arm of the coupler is terminated by a 50 ohm resistance. Port 1 is single-ended (unbalanced) while Port 2 is a balanced port. The mixed-mode S parameters [1.39] were measured and are shown in Fig.1.7(b). S_{DS21}, the transmission characteristics from single-ended Port 1 to difference mode Port 2, represents the desired transmission signal. On the other hand, S_{CS21}, the transmission characteristics from single-ended Port 1 to common mode Port 2, represents the undesired signal. The common mode rejection ratio (CMRR), the figure of merit for the balun is defined by the balance between S_{DS21} and S_{CS21}. From Fig.1.7(b), it can be seen that the rat-race coupler is good as a balun since its CMRR is more than 15 dB at the single frequency band around 2 GHz. Ferrite

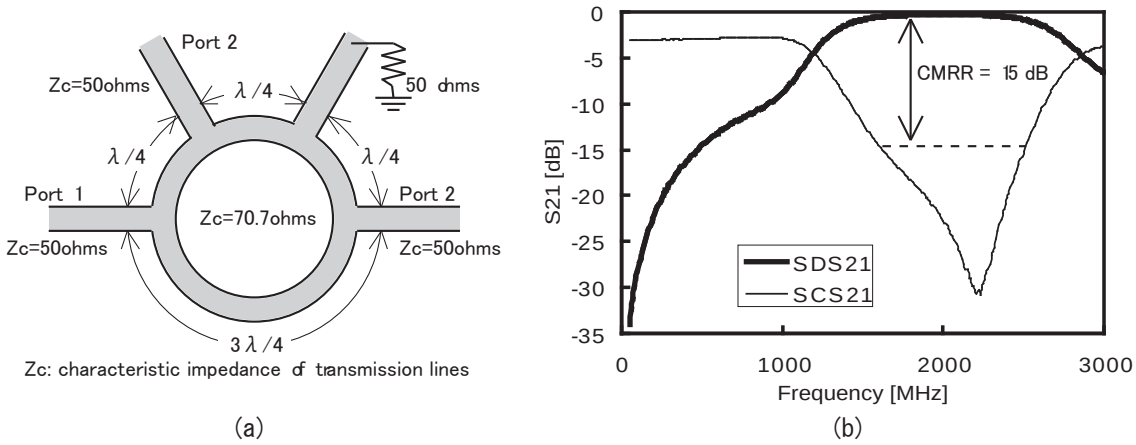

Figure 1.7: Rat-race coupler balun; (a) circuit configuration and (b) measured results.

core transformers can be wideband baluns but their upper frequency limit is around 1 GHz. There are difficulties in implementing a wideband balun [1.40], that can be used together with an RoF link.

Chapter 6 of this dissertation proposes an RoF link that uses two input ports of a dual-drive Mach-Zender modulator (DD-MZM) [1.41] to realize a balun with wideband properties. The link has a balanced input RF port and an unbalanced output RF port. Our target is to obtain a CMRR of at least 15 dB. The circuit configuration of the proposed RoF link is shown in Section 6.2. The measured performance results of the balun are shown and discussed in Section 6.3. Additionally, in Section 6.4 the optimized received light power at the PD from the standpoint of insertion loss, CMRR, and return loss is shown. This proposal can, from the standpoint of RF circuits, be considered as a wideband balun implemented by microwave photonics technology.

1.3 Outline of the Dissertation

This dissertation is organized as follows. Chapter 1, the present chapter, has introduced the background to and motivation of this study on wideband/multiband analog front-end components with high linearity. Chapters 2 and 3 describe and discuss studies on wideband/multiband antennas and switches. A multiband pin diode switch with ladder circuit configuration is proposed in Chapter 2 and a wideband folded dipole antenna with self-balanced impedance properties is introduced in Chapter 3. In Chapters 4, 5 and 6, studies on radio-on-fiber links for wideband and high speed transmission are detailed. Distortion reduction techniques are proposed in Chapters 4 and 5, and a wideband balun for radio-on-fiber link use is introduced in Chapter 6. Chapter 3 and Chapter 6 are related to wideband conversion between

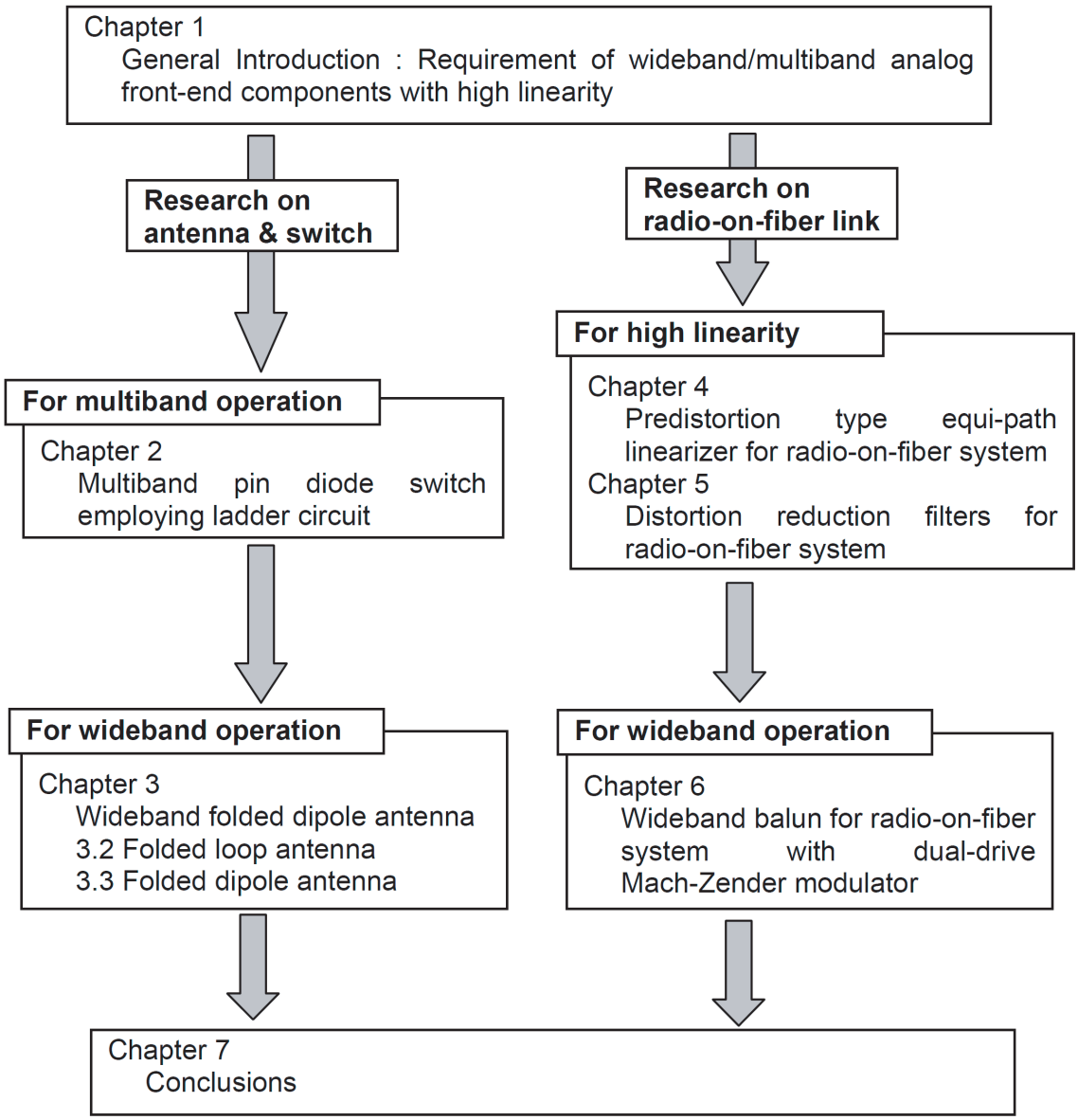

Figure 1.8: Outline of the dissertation.

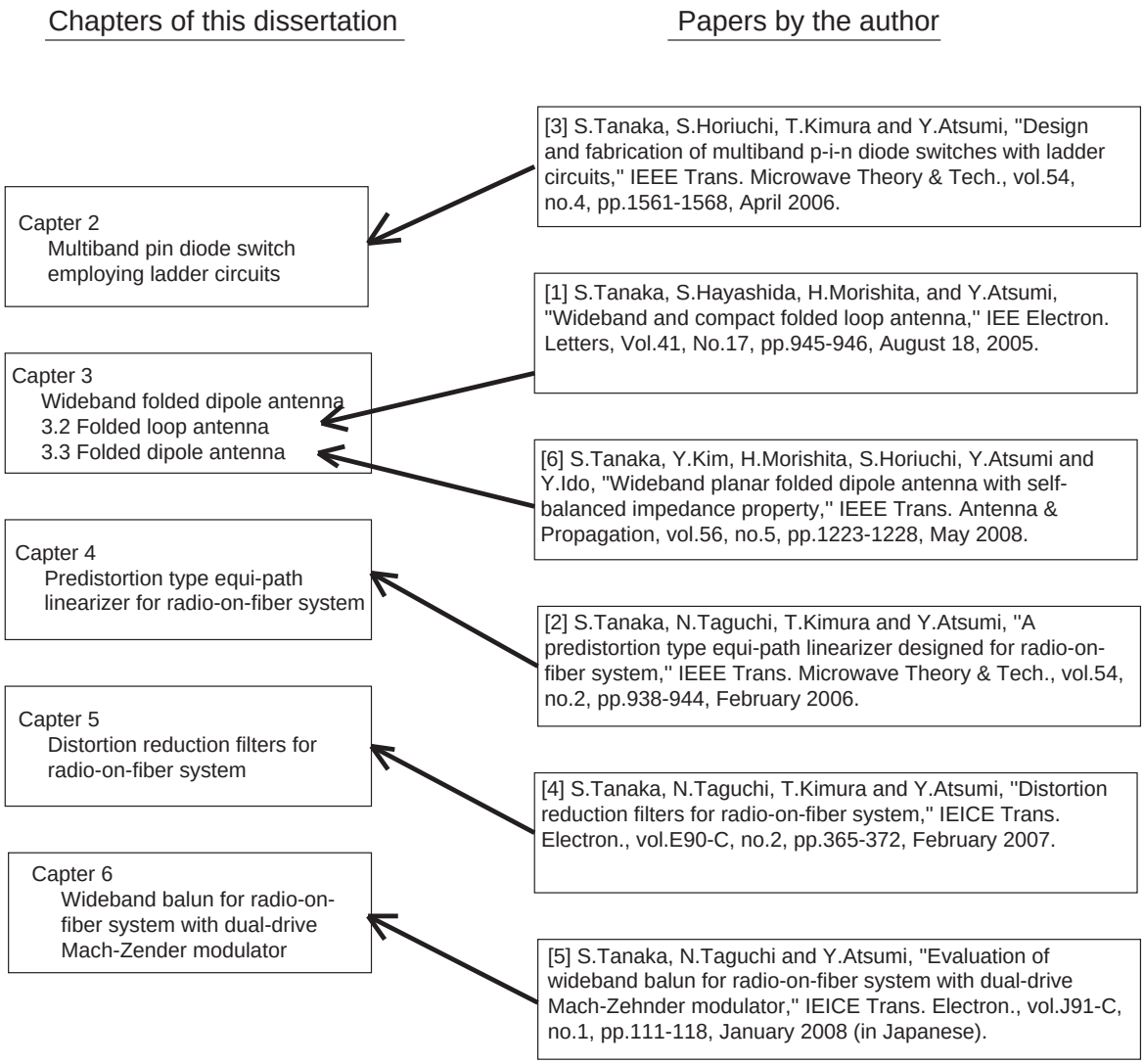

Figure 1.9: Comparison between chapters of this dissertation and the papers by the author.

balanced and unbalanced modes. Finally, this dissertation is concluded in Chapter 7. An outline of this dissertation is shown in Fig.1.8 The comparison between chapters of this dissertation and the papers by author is also shown in Fig.1.9.

1.4 References

[1.1] M.Ali, G.J.Hayes, H.S.Hwang, and R.A.Sadler, "Design of a multiband internal antenna for third generation mobile phone handsets," IEEE Trans. Antennas & Propagation, vol.51, no.7, pp. 1452-1461, July 2003.

[1.2] Y.L.Kuo and K.L.Wong, "Printed double-T monopole antenna for 2.4/5.2GHz dual-band WLAN operations," IEEE Trans. Antennas & Propagation, vol.51, no.9, pp. 2187-2192, September 2003.

[1.3] J.Mitola, III, "Software radio architecture: a mathematical perspective," IEEE J. Select. Areas Commun., vol.17, no.4, pp. 514-538, April 1999.

[1.4] R.Kohno, "Structures and theories of software antennas for software defined radio," IEICE Trans. Commun., vol.E83-B, no.6, pp.1189-1199, June 2000.

[1.5] H.Harada, M.Kuroda, H.Morikawa, H.Wakana, F.Adachi, "The overview of the new generation mobile communication system and the role of software defined radio technology," IEICE Trans. Commun., vol.E86-B, no.12, pp.3374-3384, December 2003.

[1.6] I.Bahl and P.Bhartia, "Microwave Solid State Circuit Design," John Wiley & Sons, 1988.

[1.7] C.A.Balanis, "Antenna Theory,"John Wiley & Sons, 1997.

[1.8] P.B.Kenington, "High-Linearity RF Amplifier Design,"Artech House, 2000.

[1.9] Hitachi, Ltd., "HVD142 data sheet Rev.0,"January 2001.

[1.10] D.D.Henson, D.J.Seymour and D.Zych, "100MHz to 20GHz monolithic single-pole, two, three, and four-throw GaAs pin diode switches," 1991 IEEE MTT-S Int. Microwave Symp. Dig., pp.429-432, June 1991.

[1.11] J.L.Lee, D.Zych, E.Reese, and D.M.Drury, "Monolithic 2-18 GHz low loss, on-chip biased PIN diode switches," IEEE Trans. Microwave Theory & Tech., vol.43, no.2, pp. 250-256, February 1995.

[1.12] Skyworks Solutions, Inc., "AS218-000 data sheet."

[1.13] M/A-COM, Inc., "MASWSS0070 data sheet."

[1.14] G.Matthaei, L.Young and E.M.T.Jones, "Microwave Filters, Impedance-Matching Networks, and Coupling Structures," Artech House, 1980.

[1.15] J.D.Krauss and R.J.Marhefka, "Antennas 3rd edition," McGraw-hill, 2001.

[1.16] H.Uchida and Y.Mushiake, "VHF- antenna," Corona Publishing, Japan, 1961.

[1.17] S.Hayashida, H.Morishita, K.Fujimoto, "A wideband folded loop antenna for handsets," IEICE Trans. Commun., vol.J86-B, no.9, pp.1799-1805, September 2003.

[1.18] C.W.Harrison, Jr. and R.W.P.King, "Folded dipoles and loops," IRE Trans. Antenna & Propagation, vol. AP-9, no.2, pp.171-187, March 1961.

[1.19] G.A.Thiele, P.Ekelman, Jr. and L.W.Henderson, "On the accuracy of the transmission line model of the folded dipole," IEEE Trans. Antenna & Propagation, vol. AP-28, no.5, pp.700-703, September 1980.

[1.20] Ross W. Lampe, "Design formulas for an asymmetric coplanar strip folded dipole," IEEE Trans. Antenna and Propagation, vol. AP-33, no.9, pp.1028-1030, September 1985. (See correction, vol. AP-34, no.4, p.611, April 1986.)

[1.21] W.I.Way, "Optical fiber-based microcellular systems: an overview," IEICE Trans. Commun., vol.E76-B, no.9, pp. 1091-1102, September 1993.

[1.22] H.Al-Raweshidy and S.Komaki, "Radio over fiber technologies for mobile communications networks," Artech House, 2002.

[1.23] T.Nagatsuma, "Recent progress in microwave photonics technologies," IEICE Trans. Electron., vol.J87-C, no.4, pp.357-368, April 2004.

[1.24] L.S.Fock, A.Kwan and R.S.Tucker, "Reduction of semiconductor laser intensity noise by feedforward compensation: experiment and theory," IEEE J. Lightwave Technol., vol.10, no.12, pp. 1919-1925, December 1992.

[1.25] D.Hassin and R.Vahldieck, "Feedforward linearization of analog modulated laser diodes – theoretical analysis and experimental verification," IEEE Trans. Microwave Theory & Tech., vol.41, no.12, pp. 2376-2382, December 1993.

[1.26] L.Roselli, V.Borgioni, F.Zepparelli, F.Ambrosi, M.Comez, P.Faccin and A.Casini, "Analog laser predistortion for multiservice radio-over-fiber systems," IEEE J. Lightwave Technol., vol.21, no.5, pp. 1211-1223, May 2003.

[1.27] R.A.Adb-Alhameed, P.S.Excell, J.G.Gardiner and N.T.Ari, "Volterra series analysis of a laser diode predistorter for mobile communication systems," Microwave J., vol.47, no.9, pp. 190-197, September 2004.

[1.28] N.Pothecary, "Feedforward Linear Power Amplifiers," Artech House, 1999.

[1.29] N.Suematsu, T.Takagi, A.Iida and S.Urasaki, "A predistortion type equi-path linearizer in Ku-band," The 3rd Asia-Pacific Microwave Conference Proc., pp. 1077-1080, 1990.

[1.30] R.Kohno, "Collaboration among industry, academia and government for R&D of ultra wideband wireless technologies and contribution in standardization in wireless PAN," IEICE Trans. Fundamentals, vol.J86-A, no.12, pp. 1274-1283, December 2003

[1.31] S.Tanaka, N.Taguchi, T.Kimura and Y.Atsumi, "Distortion canceller for radio-on-fiber link employing comb filter," 1st Asia-Pacific Microwave Photonics Conference, L-5, pp.366-369, April 2006.

[1.32] X.Shu, S.Jiang and D.Huang, "Fiber grating Sagnac loop and its multiwavelength-laser application," IEEE Photon. Technol. Lett., vol.12, no.8, pp. 980-982, August 2000.

[1.33] N.Taguchi, S.Tanaka, T.Kimura and Y.Atsumi, "Relative-intensity-noise reduction technique for frequency-converted radio-on-fiber system," IEEE Trans. Microwave Theory & Tech., vol.54, no.2, pp.945-950, February 2006.

[1.34] H.Uchida, H.Kamino, K.Totani, N.Yoneda, M.Miyazaki, Y.Konishi, S.Makino, J.Hirokawa, and M.Ando, "Dual-band-rejection filter for distortion reduction in RF transmitters," IEEE Trans. Microwave Theory & Tech., vol.52, no.11, pp.2550-2556, November 2004.

[1.35] "SAWEP835MCM0F00 data sheet," Murata Manufacturing Co., Ltd., Japan, November 29, 2005.

[1.36] J.Lynch, E.Entchev, B.Lyons, A.Tessmann, H.Massler, A.Leuther and M.Schlechtweg, "Design and analysis of a W-band multiplier chipset," in IEEE MTT-S Int. Microwave Symp. Dig., June 2004, pp.227-230.

[1.37] S.Horiuchi, K.Yamada, S.Tanaka, Y.Yamada and N.Michishita, "Comparisons of simulated and measured electric field distributions in a cabin of simplified scale car model," IEICE Trans. Commun., vol.E90-B, no.9, pp.2408-2415, September 2007.

[1.38] J.Reed and J.Wheeler, "A method of analysis of symmetrical four-port networks," IRE Trans. Microwave Theory & Tech., Vol.4, No.5, pp.246-252, October 1956.

[1.39] D.E.Bockelman and W.R.Eisenstadt, "Combined differential and common-mode analysis of power splitters and combiners," IEEE Trans. Microwave Theory & Tech., Vol.43, No.11, pp.2627-2632, November, 1995.

[1.40] A.C.Chen et al, "Development of low-loss broad-band planar baluns using multilayered organic thin films," IEEE Trans. Microwave Theory & Tech., Vol.53, No.11, pp.3648-3655, November, 2005.

[1.41] J.L.Corral, J.Marti and J.M.Fuster, "General expressions for IM/DD dispersive analog optical links with external modulation or optical up-conversion in a Mach-Zender electrooptical modulator," IEEE Trans. Microwave Theory & Tech., Vol.49, No.10, pp.1968-1976, October, 2001.

Chapter 2

Multiband PIN Diode Switch Employing Ladder Circuits

Single-pole double-throw switches composed of pin diodes are proposed for multi-band operations. A ladder resonance circuit is introduced to simplify their configuration and to reduce the cost. The isolation greater than 20 dB and the insertion loss less than 2 dB are achieved in experiments at three frequency bands: 1.6 GHz, 2.5 GHz and 5.8 GHz. Resonance frequency variations are investigated in detail for two types of switches consisting of (1) lumped circuit elements and (2) semi-microstrip elements. The variations on the semi-microstrip configuration are about 25 % of those with lumped circuit elements. The proposed switch does not influence the switching speed and signal distortion characteristics. It also showed good temperature stability from -30 ℃to +85 ℃.

2.1 Introduction

In the field of wireless communications, the development of multi-band handsets are in strong demand and they have been studied to support several systems [2.1][2.2]. The software radio architecture is expected to accelerate the introduction of multiband wireless communication systems [2.3]–[2.6]. One of the key elements is the single-pole double-throw (SPDT) switch with high isolation at desired multiple frequencies.

Pin diode switches are widely used for radio and microwave operation [2.6]–[2.11]. In a pin diode switch, the parasitic capacity (C_P) of the pin diode in the off state decreases the isolation of the switch at high frequencies. The standard single band switch [2.8]uses a compensating inductance (L_C) to form a parallel resonant circuit with C_P. However, this technique is only effective near a single resonance frequency.

In this Chapter, we propose a pin diode SPDT switch that can operate at multiple frequencies. The ladder circuit [2.12] introduced here has a simple configuration and lowers the manufacturing cost significantly. The circuit configuration and the design method more specifically focused on triple-band uses than [2.13] are described in

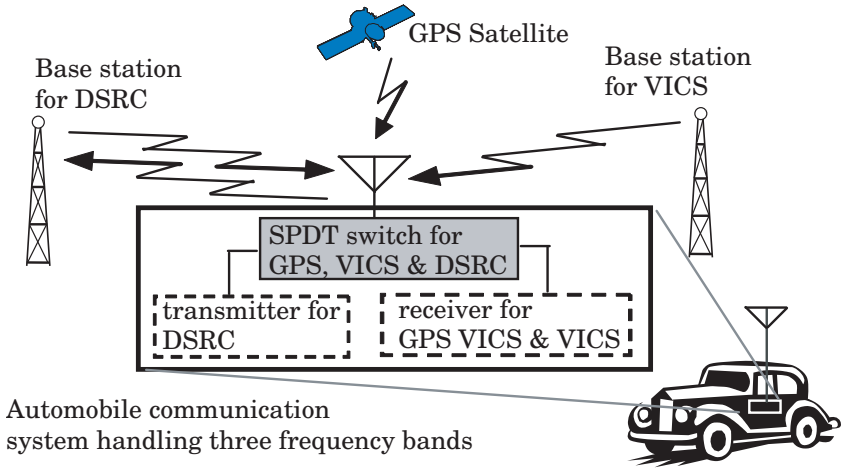

Figure 2.1: Triple-band automobile communication system.

Section 2.2. Then two examples of fabricated switches are described in Section 2.3, where one is made of all lumped elements proposed in [2.13] and the other is made of a newly proposed microstrip planar circuit configuration. The latter is newly introduced to obtain the stable resonance frequencies than those of the former in order to permit mass production. Variation characteristics of those two types of switch will be investigated in more detail than [2.13]. In addition, the temperature characteristics, the switching speed and the signal distortion characteristics of the switch are newly investigated. A higher isolation switch by adding more than one pin diode is also newly investigated for single-pole single throw (SPST) dual band uses.

As an example, we design an SPDT switch to support our previously proposed triple-layered patch antenna that operates in three frequency bands: the 1.6GHz band for global positioning system(GPS), the 2.5GHz band for the vehicle information and communication system (VICS), and the 5.8GHz band for a dedicated short-range communication system / electric toll collection system (DSRC/ETC) [2.14][2.15]. Figure 2.1 illustrates an automobile communication system that employs a triple-band patch antenna and the triple-band switch.

There are commercially available wideband switches covering DC-6GHz, e.g. [2.16][2.17]. These switches made by MMIC technology consist of expensive components such as the pHEMT and are much more expensive compared with the switches made of a discrete circuit elements proposed in this Chapter. The triple-band automobile communication systems strongly require inexpensive switches to make cheap equipment and to spread the use of these systems in Japan as quickly as possible. Also the resonant type switches have an advantage to filter out out-of-band noise.

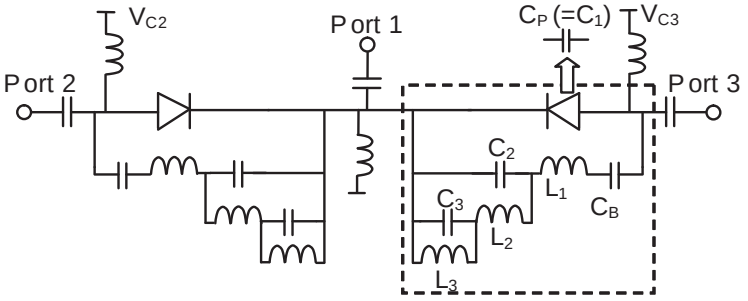

Figure 2.2: Circuit configuration of proposed SPDT switch for three frequency-bands.

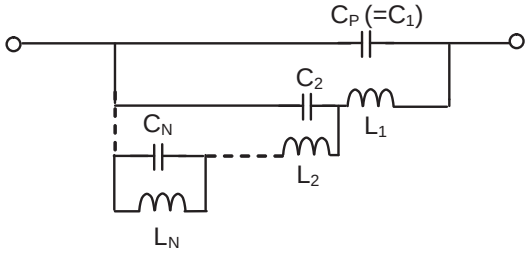

Figure 2.3: The ladder circuit for general N-parallel resonance frequencies.

2.2 Circuit Configuration and Design Method

2.2.1 Circuit Configuration with Ladder Circuit

Figure 2.2 shows the circuit configuration of the proposed SPDT switch for three frequency-band use. The SPDT switch has symmetrical construction. If V_{C2} (V_{C3}) is on and V_{C3} (V_{C2}) is off, S_{21} (S_{31}) is in the low insertion loss state and S_{31} (S_{21}) is in the high isolation state. The parallel resonance circuit with C_P and L_C in the standard single band switch is replaced by the ladder circuit which offers three different resonance frequencies. The ladder circuit in Fig.2.2 is shown by the dotted lines. In order to obtain parallel resonance in multiband frequencies, plural L_Cs are connected by shunt capacitances. As a result, the ladder circuit configuration with L and C is employed. The ladder circuit for general N-parallel resonance frequencies is shown in Fig.2.3. The parasitic capacitance C_P is expressed as C_1 for convenience in the following calculation. DC blocking capacitance C_B is omitted from Fig.2.3 as the value is selected to minimize its effect on the resonance frequencies.

In order to investigate the isolation characteristics of the switch, the impedance of the ladder circuit with the pin diode in the off-state is calculated. We assume that the parasitic elements of the inductances and capacitances shown in Fig.2.2 are negligible, as the parasitic elements are small. In general, impedance Z_N of the ladder

circuit for N-parallel resonance frequencies is expressed as follows:

$$Z_N = \cfrac{1}{j\omega C_1 + \cfrac{1}{j\omega L_1 + \cfrac{1}{j\omega C_2 + \cfrac{1}{j\omega L_2 + \cfrac{1}{\cdots + \cfrac{\cdots}{j\omega C_N + \cfrac{1}{j\omega L_N}}}}}}} \tag{2.1}$$

where ω is the angular frequency, C_k and L_k (k=1,2,$\cdots$,N) are the capacitances and inductances shown in Fig.2.3. As a special case for (2.1), Z_3 are expressed as (2.2),

$$Z_3 = \frac{j\omega\{A_1\omega^4 + A_2\omega^2 + A_3\}}{B_1\omega^6 + B_2\omega^4 + B_3\omega^2 + 1} \tag{2.2}$$

where,

$$\begin{aligned}
A_1 &= C_2C_3L_1L_2L_3 \\
A_2 &= -(C_2L_1L_2 + C_2L_1L_3 + C_3L_1L_3 + C_3L_2L_3) \\
A_3 &= L_1 + L_2 + L_3 \\
B_1 &= -C_1C_2C_3L_1L_2L_3 \\
B_2 &= C_1C_2L_1L_2 + C_1C_2L_1L_3 + C_1C_3L_1L_3 + C_1C_3L_2L_3 + C_2C_3L_2L_3 \\
B_3 &= -(C_1L_1 + C_1L_2 + C_1L_3 + C_2L_2 + C_2L_3 + C_3L_3).
\end{aligned}$$

The denominator of (2.2) is a cubic equation for ω^2. Therefore, there are three positive ωs for Z_3=infinity. This means that there exist three resonance frequencies. The number of N is not limited to three, so this technique is applicable to dual band switches and switches with more than three frequency bands.

2.2.2 Bandwidth Design Method

In the denominator of (2.2), there are five adjustable parameters (excluding C_1=C_P determined by the chosen pin diode). As the number of adjustable parameters exceeds that of the parallel resonance frequencies, more than one set of parameters provides specified three resonance frequencies.

Some examples of S_{21} calculated by (2.2) for the parallel resonance frequencies of 1.6, 2.5 and 5.8 GHz are shown in Fig.2.4. In the inset a1-a3 and b1-b3 are two pairs of three sets of parameter values used. Parasitic capacitance C_P = 0.35 pF are chosen in the calculation, because the pin diode of the prototype switch has this value.

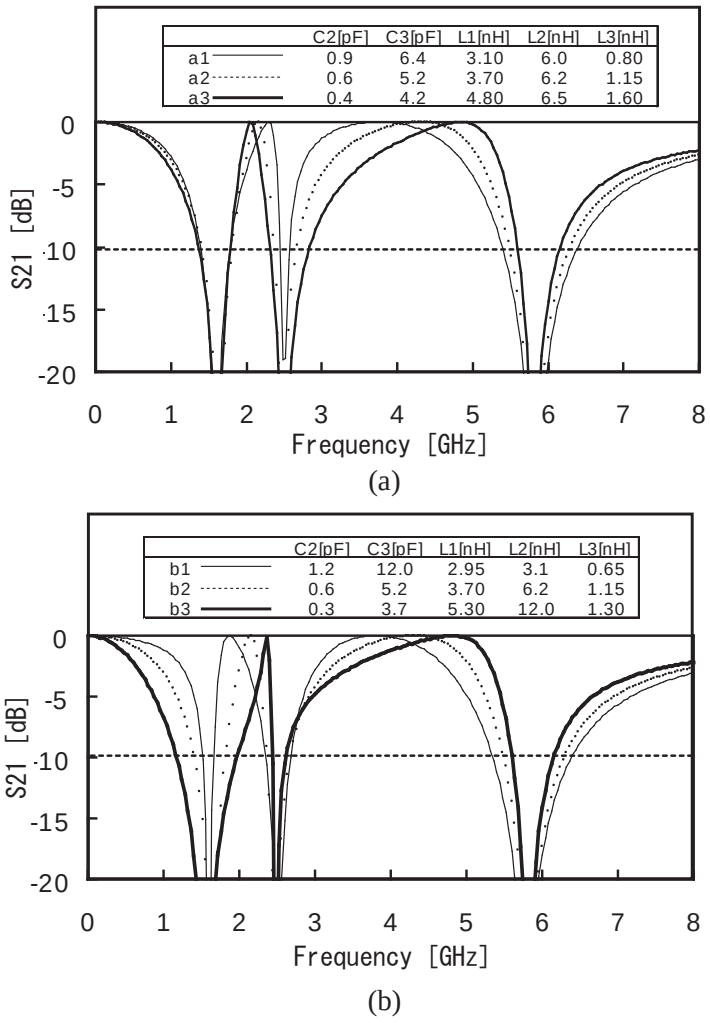

Figure 2.4: Calculated S_{21} vs. frequency of ladder circuits for three parallel resonance frequencies.

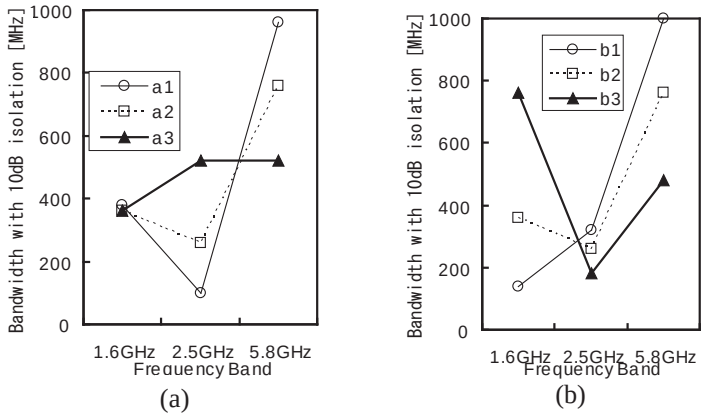

Figure 2.5: Bandwidth with 10dB isolation at 1.6, 2.5 and 5.8 GHz frequency bands.

Table 2.1: Required bandwidth for each system.

system	bandwidth
GPS	1573 - 1577 MHz (4 MHz)
VICS	2498 - 2502 MHz (4 MHz)
DSRC/ETC	5770 - 5850 MHz (80 MHz)

Figure 2.4 indicates that the bandwidths are adjustable while the parallel resonance frequencies are fixed. These characteristics are helpful to design the switch.

Figure 2.5 shows bandwidths at the three frequency bands with isolation value of 10dB in Fig.2.4. Parameter sets a1-a3 and b1-b3 are the same as those in Fig.2.4. It looks like that there are tradeoffs between the three bandwidths. Fig.2.5(a) indicates that the bandwidth adjustment by parameter sets a1-a3 makes the bandwidth changes at 2.5 GHz and 5.8 GHz while the bandwidth is stable at 1.6 GHz. Larger C_2, C_3 and smaller L_3 make wider bandwidth at 5.8 GHz and narrower bandwidth at 2.5 GHz, and vise versa. On the other hand, Fig.2.5(b) indicates that the adjustment by parameter sets b1-b3 (mainly caused by the changes of C_2, C_3 and L_2) makes the bandwidths change at 1.6 GHz and 5.8 GHz while the bandwidth is stable at 2.5GHz.

The bandwidth requirements for GPS, VICS and DSRC/ETC are summarized in Table 2.1. Based on these requirements, we chose parameter set a2(=b2) to design and fabricate an SPDT switch for the three frequency band use.

2.3 Experimental Results

Two types of triple-band switches have been fabricated based on the aforementioned circuit configuration. One has the circuit configuration shown in Fig.2.2 and employs lumped element inductances and capacitances. The other has the same circuit configuration in Fig.2.2 and employs microstrip planar circuit construction. The main specifications of the commercial pin diode [2.18] used in our prototypes are summarized on Table 2.2. A standard single band SPDT switch for comparison consists of pin diodes and lumped elements, is designed for a 5.8GHz band and is fabricated on the same printed circuit board shown in Fig.2.6. Characteristics of triple-band switches will be compared with those of the standard switch.

2.3.1 Switch with Lumped Elements Construction

Figure 2.6 shows the triple-band SPDT switch with lumped elements shown in Fig.2.6. It is fabricated on the dielectric substrate with relative permittivity $\epsilon_r = 3.45$ and thickness = 0.8mm. To simulate this lumped element switch, we used equivalent models of the pin diode [2.8], capacitors, and inductors [2.19] including parasitic

Table 2.2: Main specification of pin diode.

C_P (parasitic capacitance)	0.35 pF
R_{on} (resistance at on state)	1.5 ohms
P_r (power rating)	150 mW
V_{max} (max voltage at on state)	1.0 V
I_F (current at on state)	2.0 mA

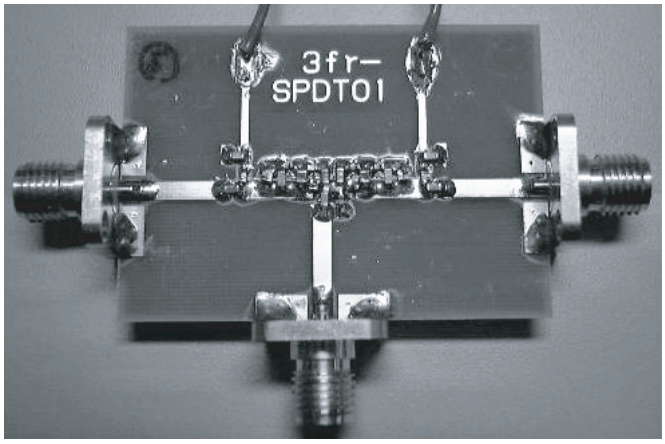

Figure 2.6: Triple-band SPDT switch with lumped elements construction.

elements. Due to the effect of the parasitic elements, the elements in Fig.2.6 were optimized within 20 % of their designed values by simulation in order to achieve the desired resonance frequencies.

Figure 2.7 shows the measured and simulated S_{21} and S_{22} values of the triple-band SPDT lumped element switch. Isolations greater than 20dB in the off-state and insertion losses under 2dB in the on-state were obtained at 1.6, 2.5, and 5.8 GHz. For S_{21}, the measured and simulated results agreed well. For S_{22}, there were some discrepancies between the results but the similar tendencies are clear. The newly proposed triple-band switch added two isolated bands to the standard single band switch, without any effects on the original isolated band. It is also found that the insertion loss levels at 1.6 GHz and 2.5GHz of the proposed switch are 2-3 dB less than those of the single band switch. This is due to the high isolation of S31 at these two bands [2.13].

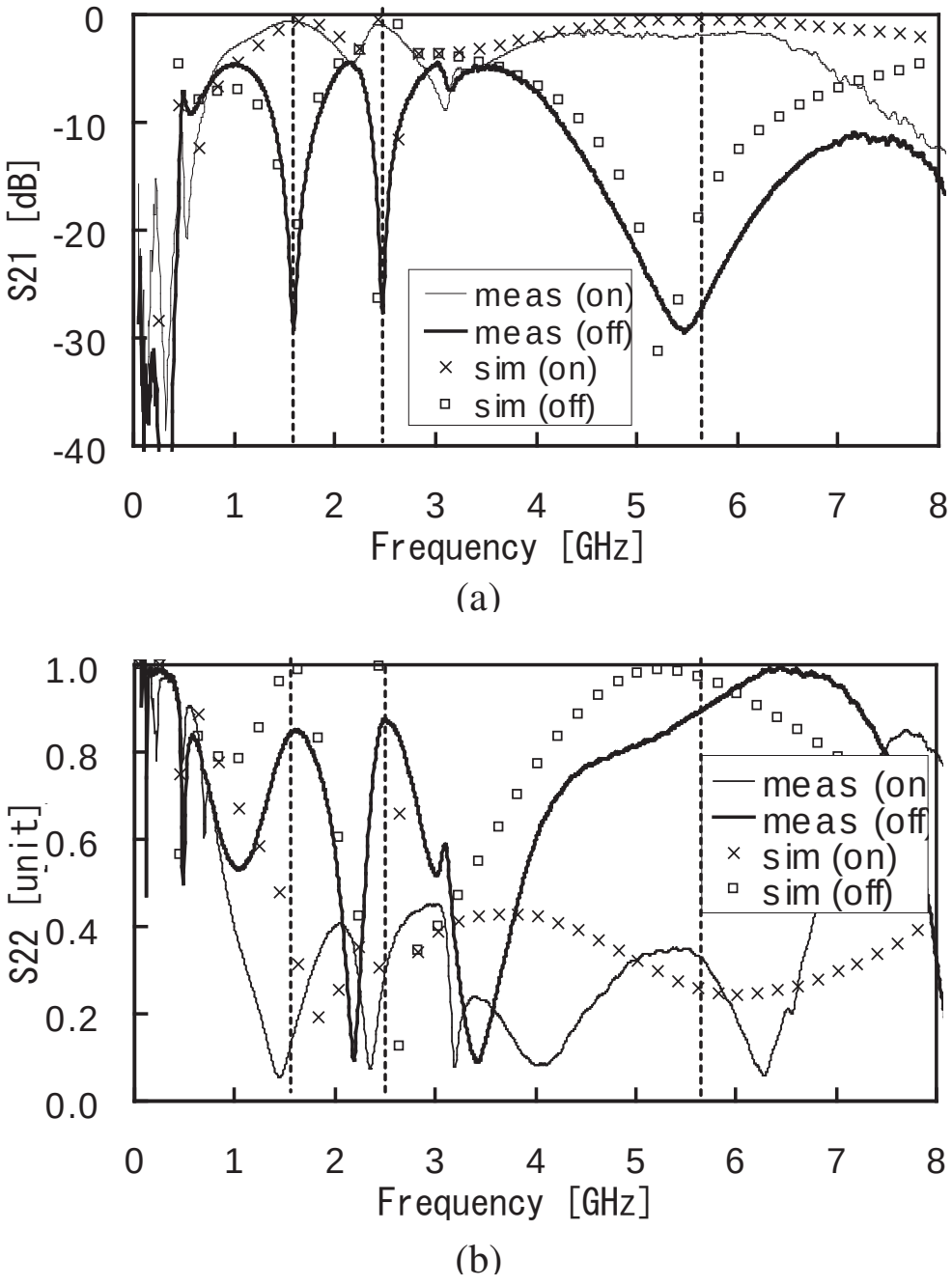

Figure 2.7: Measured and simulated (a) S_{21} and (b) S_{22} of lumped elements triple-band SPDT switch.

2.3.2 Switch with Semi-Microstrip Configuration and Variation of Triple-Band Characteristics

The variation of the parallel resonance frequencies with respect to inductors and capacitors were investigated in detail in order to permit mass production. Fortunately, a variation measurement trial with 4 samples showed good stability [2.13]. However, it is predicted from (2.2) that the variation in the three resonance frequencies of a switch composed of lumped elements will be quite large, because commercially available lumped inductors and capacitors shows ± 10 % and ± 5 % deviations of their values, respectively. In order to obtain smaller variations of those circuit component values, we introduced microstrip elements [2.8] as shown in Fig.2.8 in place of lumped elements. Figure 2.8(a) shows a microstrip type switch where all the inductors and capacitors in the ladder circuits are replaced by planar microstrip elements. Figure 2.8(b) shows a semi-microstrip type switch, where only inductors are replaced by microstrips and capacitors are still lumped elements.

The semi-microstrip switch was selected for fabrication as it is smaller than that made of all microstrip elements. Since all the prototype switches are on printed circuit boards with $\epsilon_r = 3.45$, the microstrip capacitor needs more space compared with the corresponding lumped capacitor. The second reason for this choice is that lumped capacitor values exhibit relatively less variation as mentioned before.

The approximated equivalent inductance (L_E) of a microstrip inductor is expressed as [2.8],

$$L_E = \frac{Z_0 L}{v_g} \tag{2.3}$$

where Z_0 = characteristic impedance, L = length and v_g = group velocity of the microstrip inductor. Figure 2.9 shows the fabricated triple-band SPDT switch made of semi-microstrip elements.

We made 20 prototype triple-band switches of lumped and semi-microstrip configurations in order to assess the variation characteristics in detail. Figure 2.10 shows the variation in S_{21} of 10 lumped element switches. The variation widths of the resonance frequencies are approximately 130 MHz at 1.6 GHz, 230 MHz at 2.5 GHz, and 220 MHz at 5.8 GHz. As shown in Fig.2.10(c), isolation levels greater than 20 dB were achieved for more than 800 MHz in the 5.8 GHz band. However, the variation widths in the 1.6 GHz and 2.5 GHz band are too large and the isolation levels in the desired frequency bands may not be insufficient for the mass-production.

The measured variation characteristics of the semi-microstrip switch (10 samples) are shown in Fig.2.11. Figures.2.11(a)-(c) are S_{21} and Figs.2.11(d)-(f) are S_{22}. The variation widths are 30 MHz at 1.6 GHz and 60 MHz at 2.5 GHz. It is clear that the semi-microstrip structure is very effective in reducing the variation widths in the 1.6 and 2.5 GHz band. The isolation becomes greater than 20 dB and the insertion loss becomes less than 2 dB at the desired three frequency bands. The insertion loss at 2.5 GHz is slightly increased from that of the lumped element switch, since the inductance and capacitance values in the semi-microstrip configuration are not

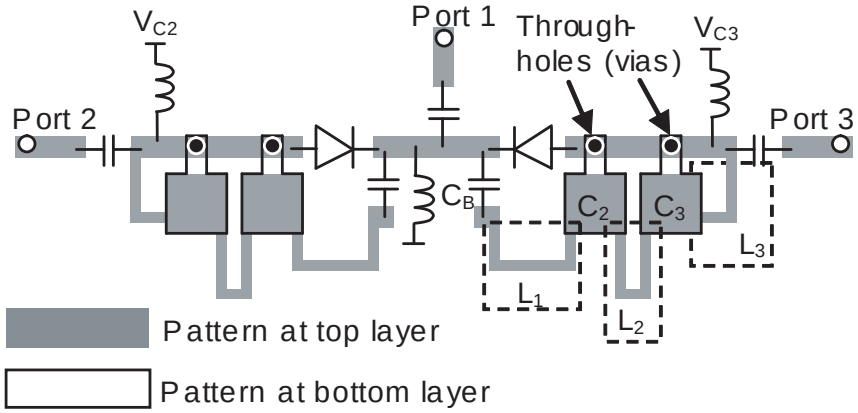

(a)

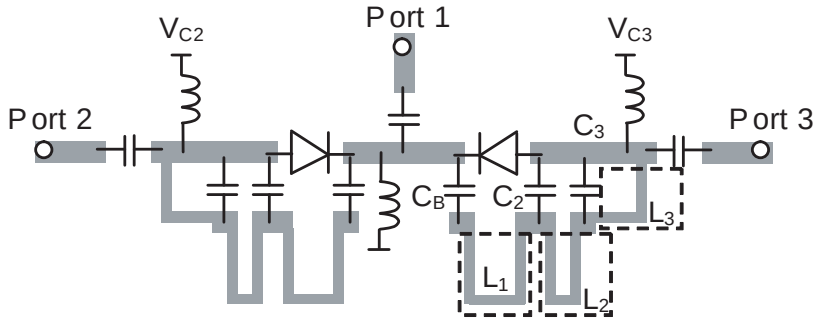

(b)

Figure 2.8: Layout pattern of triple-band SPDT switch with (a) all microstrip construction and (b) semi-microstrip construction.

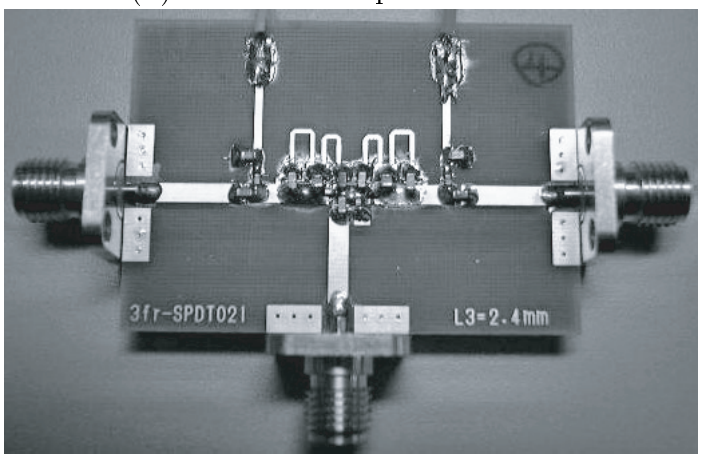

Figure 2.9: Triple-band SPDT switch with semi-microstrip construction.

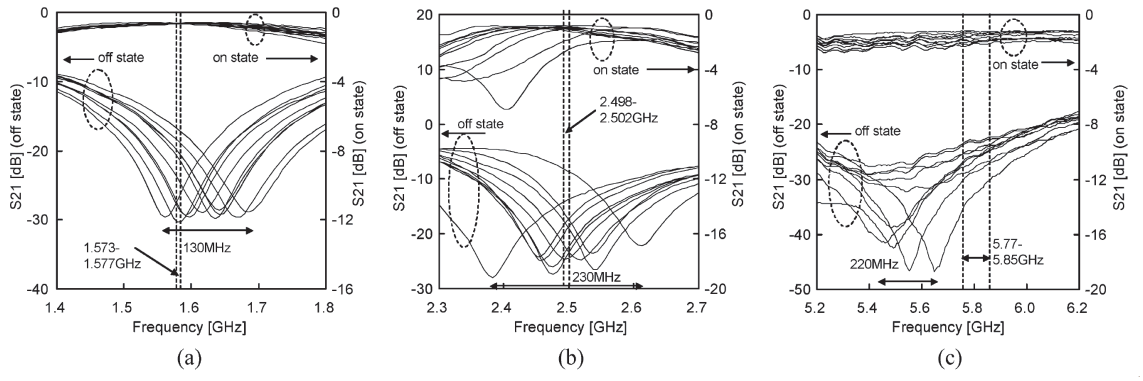

Figure 2.10: Measured variation characteristics of S_{21} of triple-band SPDT switch with lumped elements construction at (a) 1.6, (b) 2.5, and (c) 5.8 GHz (10 samples)

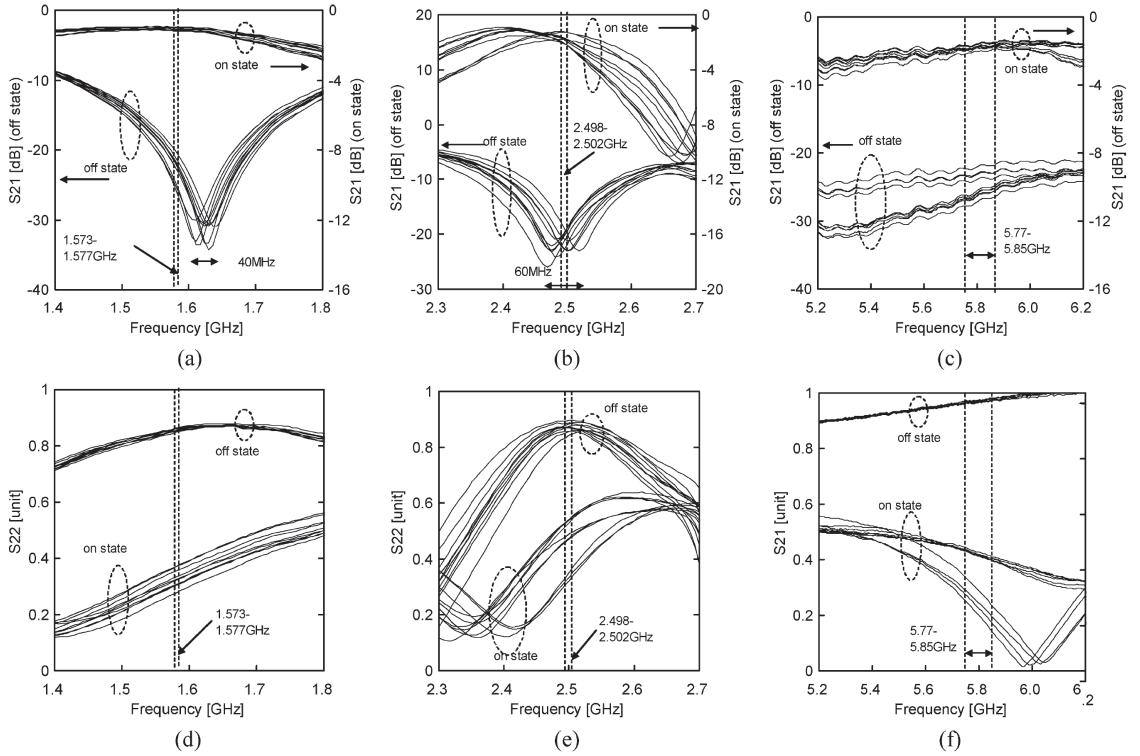

Figure 2.11: Measured variation characteristics of triple-band SPDT switch with semi-microstrip construction for (a) S_{21} at 1.6 GHz, (b) S_{21} at 2.5 GHz, (c) S_{21} at 5.8 GHz, (d) S_{22} at 1.6 GHz, (e) S_{22} at 2.5 GHz, and (f) S_{22} at 5.8 GHz (10 samples)

Table 2.3: Measured and simulated variation width (MHz).

	1.6GHz	2.5GHz
lumped element (meas)	130	230
lumped element (sim)	220	360
semi-microstrip (meas)	30	60
semi-microstrip (sim)	60	100

exactly the same as those of the lumped element switch. The measured insertion loss is a little bit higher than those of commercially available wideband switches [2.16][2.17]. As shown in Figs.2.11(d)-(f), the bottom points of S_{22} in the on-state are slightly deviated from the target frequencies and it causes the increase of insertion loss levels. So further adjustment is the next subject, but the insertion loss levels are better than those of the standard single band switch as described in Section III.A and small enough in our system. It is also considered that the long microstrip lines shown in Fig.2.9 increase insertion losses. This can be reduced when they are made on a compact printed circuit board in the actual product.

The measured and simulated variation widths at 1.6 GHz and 2.5 GHz are summarized on Table 2.3. The measured values are about 60 % of the simulated values, because the simulated value is obtained from the worst case analysis. Both measured and simulated variation widths of the semi-microstrip switch are reduced to about 25 % of those of the lumped element switch. It is also found that the variation in C_P for the pin diode is negligible compared to the variation in inductance and capacitance values.

2.3.3 Switching Speed, Distortion, and Temperature Characteristics

Figure 2.12 shows the measured switching speed characteristics of the triple-band switch with the semi-microstrip configuration and standard single band switch. The measurement was done by high speed oscilloscope at 5.8 GHz. There is little difference between Fig.2.12(a) and (b). Therefore the ladder circuit configuration does not influence the switching speed. The triple-band switch with all the lumped elements shows the similar characteristics. The measured switching time is 0.15 μ sec (turn-on) and 1.5 μ sec (turn-off). The measured delay time is 0.02 μ sec (turn-on) and 0.01 μ sec (turn-off). These times satisfy the specification of DSRC system [2.20].

Figure 2.13 shows the measured signal distortion characteristics of the triple-band switch with the semi-microstrip configuration and the standard single band switch. The carriers and the third order intermodulation (IM3) components were measured when the two tone carriers at 5.800 GHz and 5.805 GHz are injected in accordance

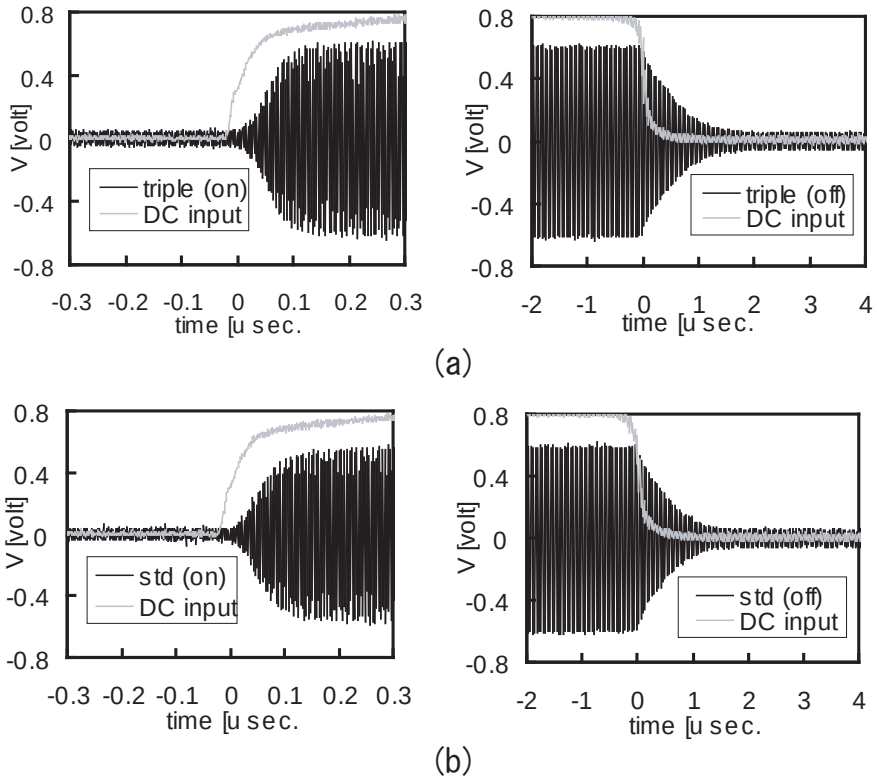

Figure 2.12: Measured switching speed characteristics at 5.8 GHz band of (a) semi-microstrip triple-band switch and (b) standard single band switch.

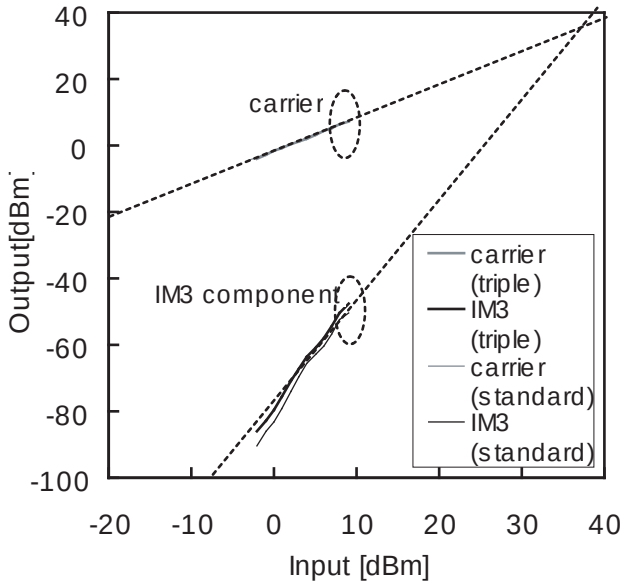

Figure 2.13: Measured carrier and IM3 components at 5.8 GHz band of semi-microstrip triple-band switch and standard single band switch.

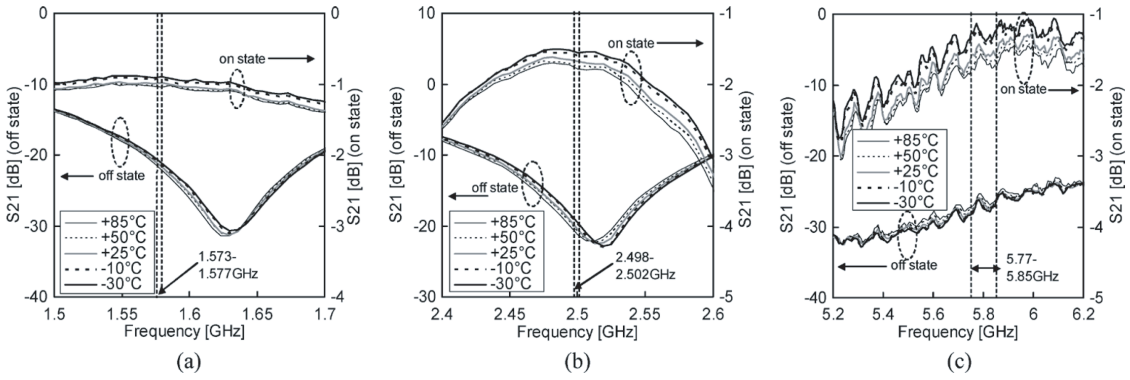

Figure 2.14: Measured temperature characteristics of S_{21} of triple-band SPDT switch with semi-microstirp construction at (a) 1.6, (b) 2.5, and (c) 5.8GHz.

with the DSRC specification [2.20]. There is little difference in the distortion between the triple-band semi-microstrip and single band switch, so the ladder circuit configuration does not influence the distortion characteristics. The triple-band switch with the lumped element configuration shows the similar characteristics. In Fig.2.13 the third order intercept point (OIP3) is obtained by extrapolation and is about +35 dBm. It is enough for DSRC specifications [2.20]. The measured OIP3s at 1.575 and 2.500 GHz are +44 dBm and +40 dBm, respectively, when the two-tone carriers with 1 MHz separation are injected. These values are large enough in receiving GPS and VICS signals [2.14].

Figure 2.14 shows the temperature characteristics of S_{21} of the triple-band semi-microstrip switch. From -30 ℃to +85 ℃, the switch offers good stability and the variations in resonance frequencies are within 20 MHz. The minimum points (resonance frequency) in the off-state are shifted to lower frequencies with the increase of the temperatures. It is estimated that the variations in resonance frequencies are mainly caused by the thermal expansion of the materials of the lumped elements and the printed circuit board.

Figure 2.14 shows that the insertion loss is larger at higher temperatures. This is due to the temperature characteristics of the cable. But the variations of the insertion loss are within 1 dB over the temperature range.

2.3.4 Study on Higher Isolation Switch

In our system isolations larger than 20 dB are enough for the narrow bands summarized in Table 2.1. However, in order to prepare for the requirement of higher isolations and wider bandwidth, we study on the isolation improvement of the multiband switch in this subsection. It is known that the isolations can be improved by adding more pin diodes to a switch [2.8]. As a trial, we made a higher isolation SPST

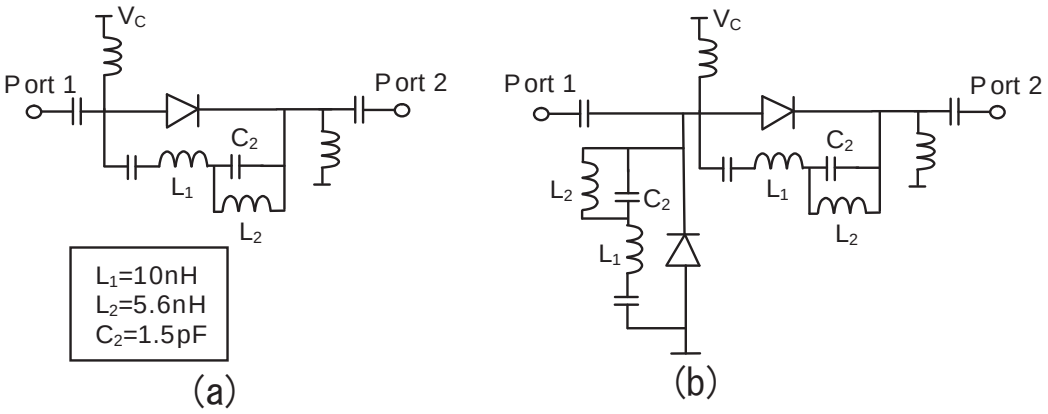

Figure 2.15: Circuit configuration of dual band SPST switch employing (a) one pin diode and (b) two pin diodes.

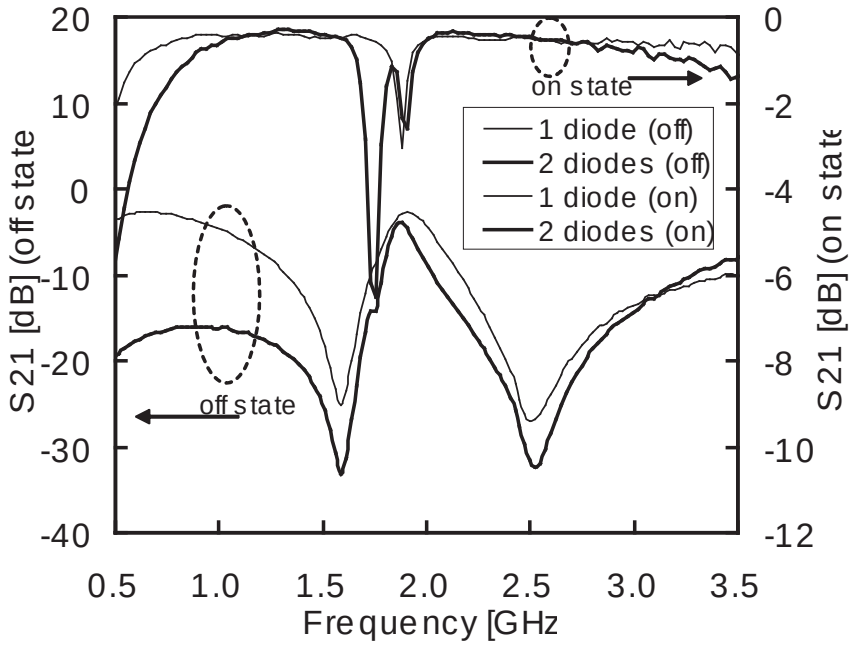

Figure 2.16: Measured S_{21} of dual band SPST switch employing one and two pin diodes.

switch for dual bands (1.6 and 2.5 GHz) by adding pin diodes.

Figure 2.15(a) shows a dual band SPST switch employing ladder circuits. One pin diode is employed and L_1, L_2 and C_2 values for 1.6 and 2.5 GHz operation are shown in the inset. Figure 2.15(b) shows a higher isolation SPST dual band switch employing two pin diodes. L_1, L_2 and C_2 values in Fig. 2.15(b) are the same as those in Fig.2.15(a). Control voltage V_C is switched from plus to minus in the two diodes switch. These two switches are fabricated on the same printed circuit board with all lumped elements.

Figure 2.16 shows measured S_{21} of both switches. At 1.6 and 2.5 GHz, the isolations of the two-diode switch improve by more than 5 dB from those of one-diode switch. As a result, the bandwidths with isolations more than 20 dB are widened. Insertion loss levels at both frequencies are almost the same. The circuit configuration shown in Fig. 2.15(b) can be extended to triple band or more, and applicable to an SPDT configuration. So Fig.2.16 suggests that the result shown in Fig.2.11 can be improved by adding more pin diodes.

2.4 Conclusion

The SPDT switch design and fabrication was discussed for purpose of reducing the cost and increasing the reliability. The switch showed the isolation greater than 20 dB and the insertion loss less than 2 dB at three different frequency bands: 1.6 GHz, 2.5 GHz, and 5.8 GHz. The use of the ladder circuit realizes a simple circuit configuration, the number of frequency bands is not limited to three, and the frequency range is not limited to 1-6 GHz. Simulations including parasitic elements gave good agreement with the measured results. Ten prototype switches were fabricated for the lumped and semi-microstrip model to measure the variations of the switching characteristics for their future mass production. Their variation width of the resonance frequencies were investigated in detail. The semi-microstrip configuration gave quite stable resonance frequencies and its variation width became about 25 % of that of the lumped element switch. It was also found by measurements that the ladder circuit configuration did not influence switching speed and signal distortions. The switch showed good temperature stability from -30 ℃to +85 ℃. It is also found that the isolations of the multi-band switch can be improved by adding pin diodes without the degradation of insertion losses. The switch introduced here may become the key device to bi-directional multi-band automobile communication systems.

2.5 References

[2.1] M.Ali, G.J.Hayes, H.S.Hwang, and R.A.Sadler, "Design of a multiband internal antenna for third generation mobile phone handsets," IEEE Trans. Antennas & Propagation, vol.51, no.7, pp. 1452-1461, July 2003.

[2.2] Y.L.Kuo and K.L.Wong, "Printed double-T monopole antenna for 2.4/5.2GHz dual-band WLAN operations," IEEE Trans. Antennas & Propagation, vol.51, no.9, pp. 2187-2192, September 2003.

[2.3] J.Mitola, III, "Software radio architecture: a mathematical perspective," IEEE J. Select. Areas Commun., vol.17, no.4, pp. 514-538, April 1999.

[2.4] R.Kohno, "Structures and theories of software antennas for software defined radio," IEICE Trans. Commun., vol.E83-B, no.6, pp.1189-1199, June 2000.

[2.5] H.Harada, M.Kuroda, H.Morikawa, H.Wakana, F.Adachi, "The overview of the new generation mobile communication system and the role of software defined radio technology," IEICE Trans. Commun., vol.E86-B, no.12, pp.3374-3384, December 2003.

[2.6] S.Tanaka, N.Taguchi, T.Kimura and Y.Atsumi, "Frequency-tunable PIN diode switch for software defined radio," Proc. 35th European Microwave Conf., pp.1771-1774, October 2005.

[2.7] R.Tenenholtz, "A 2000 watt CW MIC 20-500MHz SPDT pin diode switch module," 1981 IEEE MTT-S Int. Microwave Symp. Dig., pp.252-254, June 1981.

[2.8] I.Bahl and P.Bhartia, "Microwave Solid State Circuit Design," John Wiley & Sons, 1988.

[2.9] B.L.Smith and M.H.Carpentier, "The Microwave Engineering Handbook," Vol.1, Van Nostrand Reinhold, 1993.

[2.10] P.Vizmuller, "RF Design Guide: Systems, Circuits and Equations," Artech House, 1995.

[2.11] J.L.Lee, D.Zych, E.Reese, and D.M.Drury, "Monolithic 2-18 GHz low loss, on-chip biased PIN diode switches," IEEE Trans. Microwave Theory & Tech., vol.43, no.2, pp. 250-256, February 1995.

[2.12] G.Matthaei, L.Young and E.M.T.Jones, "Microwave Filters, Impedance-Matching Networks, and Coupling Structures," Artech House, 1980.

[2.13] S.Tanaka and T.Kimura, "A pin diode switch operating at multi-frequency bands," 2004 IEEE MTT-S Int. Microwave Symp. Dig., pp.1129-1132, June 2004.

[2.14] S.Tanaka, S.Yuminaga and T.Kimura, "On-board multi-layered microstrip antenna and associated RF circuits for multiple ITS applications," Proc. 11th World Congress on Intelligent Transport Systems, IS01, No.3059, October 2004.

[2.15] S.Yuminaga and Y.Yamada, "A triple-layered patch antenna capable of triple-frequency operation," Proc. IEEE AP-S Int. Symp., vol. 4, pp.138-141, July 2003.

[2.16] Skyworks Solutions, Inc., "AS218-000 data sheet."

[2.17] M/A-COM, Inc., "MASWSS0070 data sheet."

[2.18] Hitachi, Ltd., "HVD142 data sheet Rev.0,"January 2001.

[2.19] C.R.Paul, "Introduction to Electromagnetic Compatibility," Wiley-Interscience, 1992.

[2.20] Association of Radio Industries and Businesses, "Dedicated Short-Range Communication System ARIB Standard ARIB STD-T75 1.2," (2003).

Chapter 3

Wideband Folded Dipole Antenna

Two types of wideband antenna based on folded dipole construction are proposed. One is a folded loop antenna, that has folded portion at both ends of folded dipole antenna. The other is a planar folded dipole antenna that has simple planar construction without a ground plane and is easy to be assembled. Parameter values are adjusted in order to obtain wideband properties and compactness by using an electromagnetic simulator based on the method of moments. An experimental result centered at 1.7 GHz for 50 ohms impedance matching shows that the antenna has bandwidth over 55 % (VSWR $\leq$ 2). The gains of the antenna are almost constant (2 dBi) in this frequency band and the radiation patterns are very similar to those of a normal dipole antenna. It is also shown that the antenna has a self-balanced impedance property in this frequency band.

3.1 Introduction

With the recent progress and rapid increase in radio communication systems, wideband wireless systems are being put into actual use; examples are an ultra wideband system [3.1][3.2] and digital terrestrial television [3.3][3.4]. This emphasizes the importance of designing high performance antennas for small mobile terminals. A key demand is wideband and compact antennas [3.5][3.6].

One interesting candidate for wideband and compact antennas is the folded loop antenna [3.7]–[3.9]. It is named as folded loop antenna but basically constructed by folding both ends of an approximately $\lambda_C/2$ length folded dipole antenna [3.12]–[3.16] (λ_C is the wavelength at the center frequency f_C). In the previous paper, a folded loop antenna system for handsets accompanied with ground plane has been introduced and analyzed [3.7]. It has been also reported that the folded loop antenna with more than 40 % bandwidth (VSWR $\leq$ 2) can be constructed around finite ground plane [3.8][3.9]. This folding parts are important to widen the bandwidth and by adjusting some construction parameters.

One of the aim in this Chapter is to remove the ground plane from this wideband

folded loop antenna and to maintain wideband characteristics with just the folded loop antenna element itself. The bandwidth (VSWR $\leq$ 2) changes by the antenna parameter values are investigated in detail, in order to obtain maximum bandwith with this construction. It is described in Chapter 3.2 [3.10][3.11].

The other aim in this Chapter is to simplify the antenna configuration of the folded dipole antenna with folded elements, that is, to remove the folding parts at both ends of the element and at the same time to maintain wideband properties. With this modification, the antenna can be planar and is easy to be assembled. As is done in case of folded loop, the parameter distributions for maximum bandwidth are investigated. It is described in Chapter 3.3 [3.18]–[3.20].

It is normal to apply a balanced feed to a balanced antenna like a dipole antenna. However, a narrow band folded dipole antenna has self balanced properties [3.15][3.17] so an unbalanced feed is also applicable. In this case, no balun is needed so the antenna is cost-effective. Therefore, balanced and unbalanced feeds are evaluated in order to examine the self-balanced properties.

3.2 Folded Loop Antenna

3.2.1 Antenna Structure

Figure 3.1 shows the structure of proposed folded loop antenna and its parameters. It is constructed by folding both ends of folded dipole antenna. Since the folded dipole can be considered as a λ_C-long loop antenna, the antenna is referred to as a folded loop. When a is fixed to 72mm, bandwidth = 53 % is obtained with w_1 = 4 mm, w_2 = 28 mm, d = 2 mm, h = 2 mm, and s = 60mm. In order to find optimum antenna parameters, we investigated impedance characteristics for various parameters by the simulation based on the method of moment [3.21].

3.2.2 Impedance Characteristics

Figure 3.2(a)-(c) shows the impedance variations from folded dipole antenna with ground plane [3.7]–[3.9] (a = 72 mm, w_1 = 2 mm, w_2 = 8 mm, d = 2 mm, h = 18 mm, s = 60 mm, g = 2 mm) to folded loop antenna without ground plane [3.10]. Parameter g is gap between antenna and ground plane, so $g = \infty$ means there is no ground plane. As shown in Fig.3.2(a), wideband characteristics are lost when ground plane is removed. So as shown in Fig.3.2(b)(c), w_2 is increased and h is decreased to obtain wideband characteristics without ground plane. Figure 3.2(d)-(f) shows the impedance variations with other parameters, those are w_1, d, and s. From Fig.3.2, it is shown that the parameters w_2, h, and s have strong influence on impedance characteristics of folded loop antenna without ground plane.

Figure 3.3 shows bandwidth (VSWR $\leq$ 2) characteristics of folded loop antenna when the parameters w_2, h, and s are simultaneously changed. Figure 3.3(a) shows

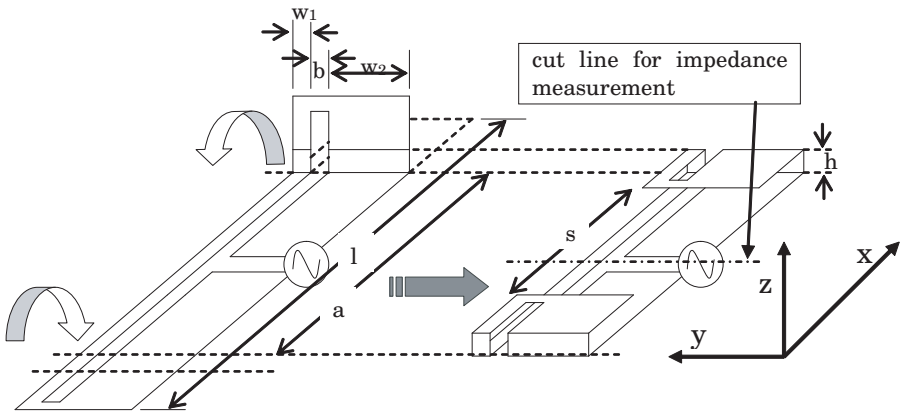

Figure 3.1: Antenna structure of a folded loop antenna.

the parameter ranges to obtain maximum bandwidth, it is w_2 = 28–32 mm and $h \leq$ 10 mm. Figure 3.3(b)(c) shows the bandwidth decreases when s decreases. However, the peaks of bandwidth are found around the range of w_2 = 28–32 mm and $h \leq 10$ mm.

Figure 3.4 shows the measured and simulated VSWR of the folded dipole antenna. The measured result shows that VSWR ≤ 2 is obtained from 1.43 GHz to 2.47 GHz (bandwidth = 53 %). Figure 3.4 shows that the measured and simulated results agreed well each other.

3.2.3 Radiation Pattern

Figure 3.5 shows the measured and simulated radiation pattern of the folded loop antenna at 1.5, 1.9 and 2.4 GHz. At the time of measurement, coaxial cable covered with electric wave absorption material is employed instead of balun. The measured and simulated results agreed well for the main polarization (E_θ). They are around 2 dBi in this frequency band and the pattern is almost same to the half-wavelength dipole. The measured and simulated antenna gains are summerized in Table 3.1. The antenna gain has tendency to increase when the operation frequency goes up.

The measured cross polarizations (E_ϕ) are larger than the simulated values at 1.5 and 2.4 GHz. On the other hand, both results agreed well at 1.9 GHz. This is caused by the small ocsillator that is only applicable to 1.9 GHz band. The simulated E_ϕ has tendency to increase when the operation frequency goes up.

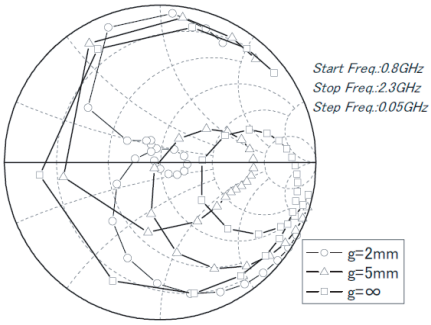

(a) Impedance vs. g
(w_1=d=2mm, w_2=8mm, h=18mm, s=40mm)

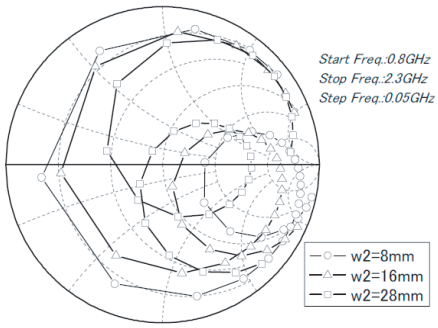

(b) Impedance vs. w_2
(g=∞, w_1=d=2mm, h=18mm, s=40mm)

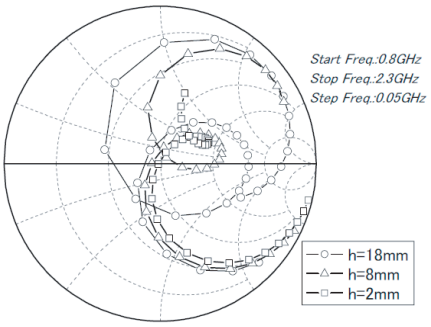

(c) Impedance vs. h
(g=∞, w_2=28mm, w_1=d=2mm, s=40mm)

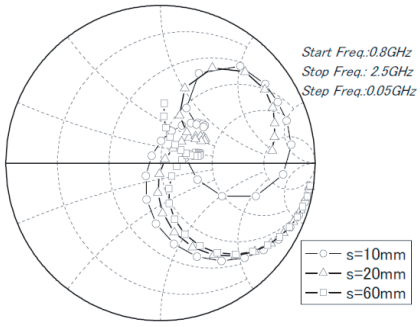

(d)Impedance vs. s
(w_1= d=2mm, w_2=28mm, h=2mm)

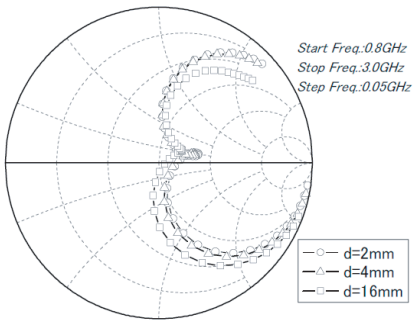

(e) Impedance vs. d
(w_1=2mm, w_2=28mm, h=2mm, s=60mm)

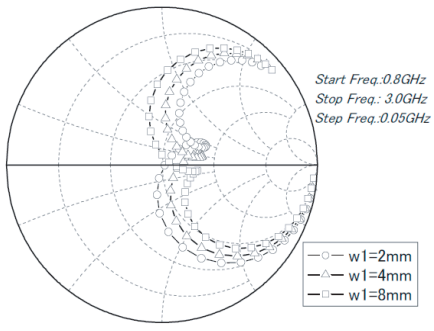

(f) Impedance vs. w_1
(d=2mm, w_2=28mm, h=2mm, s=60mm)

Figure 3.2: Simulated input impedances of a folded loop antenna with various parameter values

(a) s=60mm

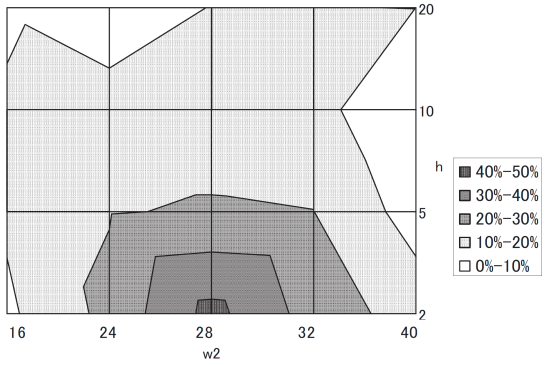

(b) s=20mm

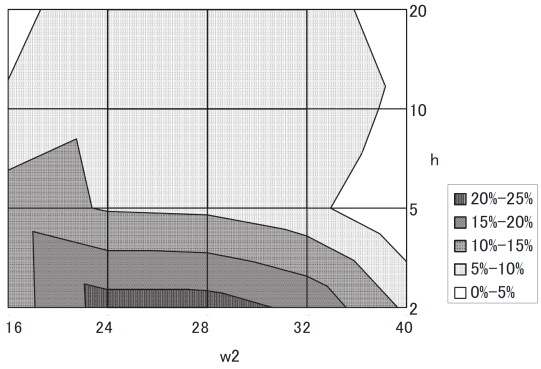

(c) s=10mm

Figure 3.3: Simulated bandwidth of a folded loop antenna when w_2, h and s are changed.

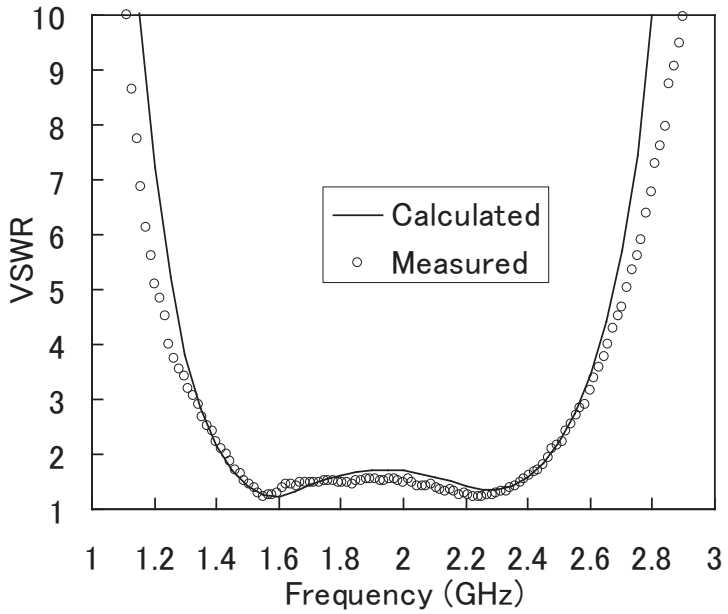

Figure 3.4: Measured and simulated VSWR of a folded loop antenna.

Table 3.1: Antenna gain of a folded loop antenna.

Frequency	1.5 GHz	1.9 GHz	2.4 GHz
Simulated	2.1 dBi	2.2 dBi	2.6 dBi
Measured w/o balun	2.3 dBi	2.1 dBi	2.2 dBi

3.3 Folded Dipole Antenna

Fig. 3.6 shows the simulated S_{11} of folded loop antenna with various s. It is observed that the bandwidth with S_{11} less than -9.5 dB (equivalent to VSWR less than 2) increases when s increases. So it is expected that planar folded dipole antenna also have wideband property. As is plotted in Fig.3.6 together, folded dipole antenna without folding at both ends also exhibit wideband characteristics. In this subsection, this wideband folded dipole antenna will be investigated in detail.

3.3.1 Antenna Structure

Figure 3.7 shows the structure of the proposed planar folded dipole antenna. The folded dipole antenna [3.12]–[3.16] with two $\lambda/2$-long elements is constructed 2-dimensionally. Its construction parameters are also indicated in Fig.3.7. The length of the elements, l is fixed to 88 mm so $f_C \approx 1.7$ GHz. The widths of the two strips are

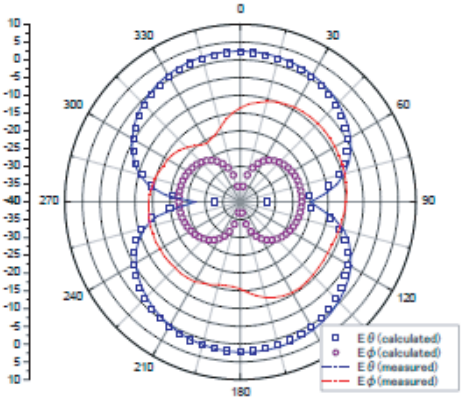

(a) 1.5GHz

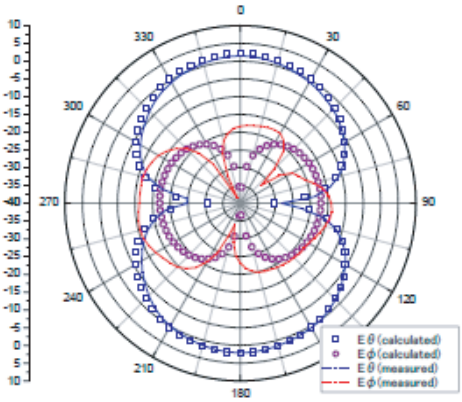

(b) 1.9GHz

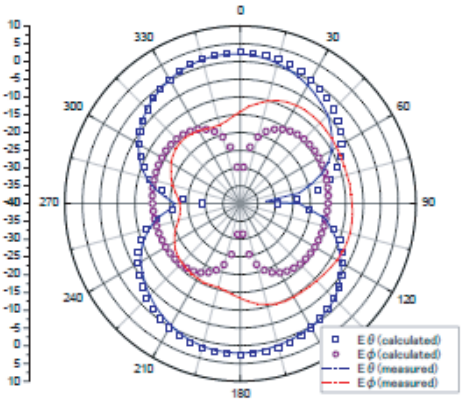

(c) 2.4GHz

Figure 3.5: Measured and simulated radiation pattern of a folded loop antenna.

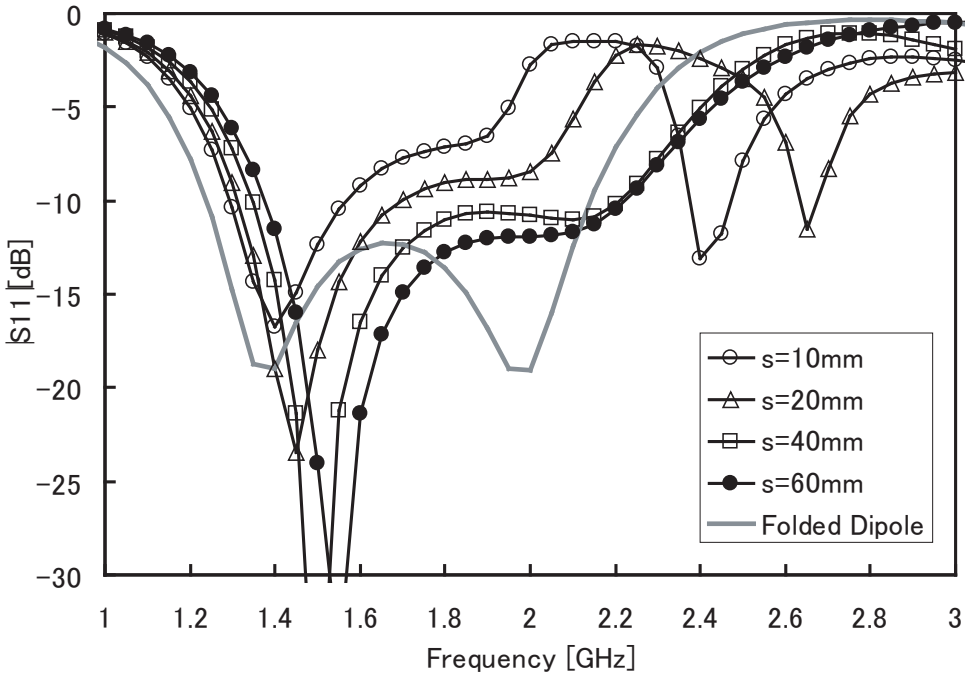

Figure 3.6: Simulated S_{11} of folded loop antenna with various s.

w_1 and w_2. The width w_2 is set to be wider than w_1 in order to match the antenna impedance to 50 ohms. The separation width between two strips is d. The end width of the folded portion is e. The gap of the feed point, g is fixed to 2 mm. So we can adjust 4 parameters, w_1 , w_2, d, and e. A copper plate with 0.2 mm thickness is employed to construct the antenna.

3.3.2 Impedance Characteristics

In this subsection, the input impedance of the planar folded dipole antenna shown in Fig.3.7 is investigated. First, impedance changes due to 4 construction parameters are discussed. Then, the bandwidth (VSWR $\leq$ 2) and f_C changes due to 3 active parameters are investigated in detail together with the standpoint of compactness. In this subsection, the electromagnetic simulator based on the method of moments [3.21] is used. Only balanced feed is considered in the simulations. Finally, experimental results with balanced and unbalanced feeds, and simulated results are compared and discussed.

Impedance Changes by the Parameters

Figure 3.8 shows the impedance characteristics of the planar folded dipole antenna, when 4 parameter values, w_1 , w_2, e, and d is changed. The starting values of these

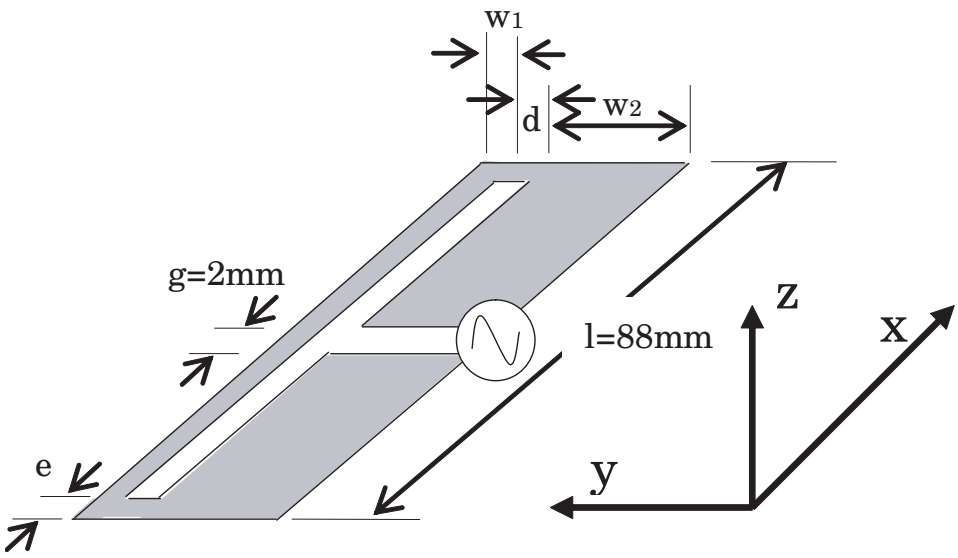

Figure 3.7: Antenna structure of the planer folded dipole antenna.

parameters are $w_1 = 4$ mm, $w_2 = 2$ 8mm, $d = 2$ mm and $e = 2$ mm, as those are used in [3.10][3.11]. As shown in Fig.3.8(a), rounded curves on the Smith chart (with two resonance frequencies) go to higher impedance when w_2 is decreased under 32mm. When w_2 is increased over 32mm, the rounded curve goes to higher reactance. $w_2 =$ 32 mm is the best value for wideband impedance matching around 50 ohms. So we changed w_2 from 28mm to 32mm for the next studies.

Figure 3.8(b) shows that imaginary part of the impedance decreases when w_1 increases. However, the change caused by w_1 has less impact than that by w_2. Figure 3.8(c) shows that the real part of the impedance increases when e increases. So wideband properties cannot be obtained when $e \leq 16$ mm if 50 ohms matching is desired. As shown in Fig.3.8(d), little impedance change is observed when d is changed. Wavelength λ_{HRF} at 2 GHz (higher resonance frequency; refer to Fig.3.12) is 150 mm, so $d = 2$ mm is $0.013\lambda_{HRF}$ and $d = 16$ mm is $0.107\lambda_{HRF}$, respectively. According to [3.14], d is better to be less than 0.01λ, however, this limit is not so strict. So the impedance is almost constant when d is changed from 2 to 16 mm.

Bandwidth (VSWR $\leq$ 2) Changes by the Parameters

As is shown in the former subsection, construction parameters w_1, w_2, and e have an important role in a planar folded dipole antenna. So we are going to change these parameters simultaneously in order to find the optimum parameter sets for wideband properties. Figure 3.9 shows the simulated bandwidth when parameters w_2 and e are simultaneously varied while $w_1 = 4$ mm and $d = 2$ mm are fixed. Figure 3.9 illustrates the area of w_2 and e to obtain the bandwidth over 50 %. For the bandwidth

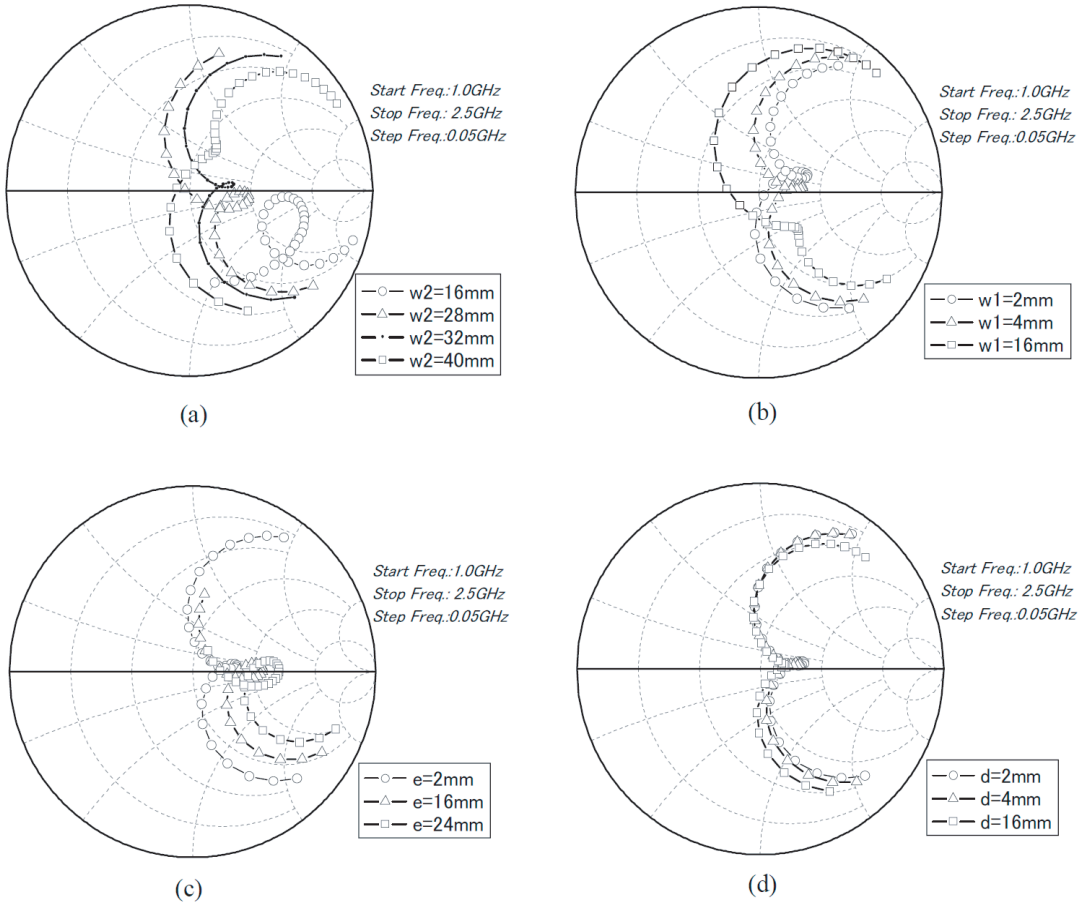

Figure 3.8: Simulated input impedance characteristics of a planar folded dipole antenna with the variation of (a) w_2 (w_1 = 4 mm, d = 2 mm, e=2 mm), (b) w_1 (w_2 = 32 mm, d = 2 mm, e = 2 mm), (c) e (w_2 = 32 mm, w_1 = 4 mm, d = 2 mm) and (d) d (w_2 = 32 mm, w_1 = 4 mm, e = 2 mm).

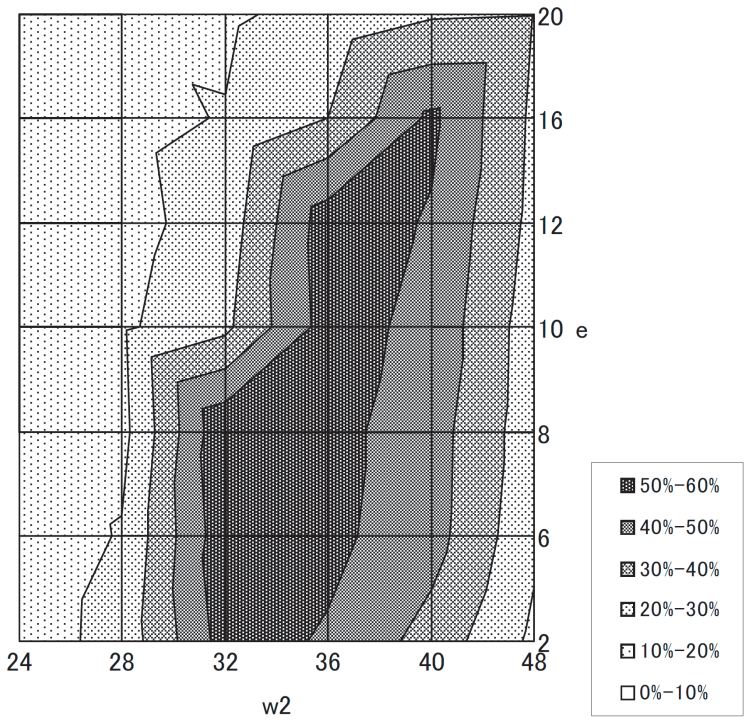

Figure 3.9: Simulated bandwidth (in %) of a planar folded dipole antenna with the variation of w_2 and e ($w_1 = 4$ mm, $d = 2$ mm)

more than 50 %, w_2 shall be 32 mm for small e and w_2 shall be 40 mm for large e. So for the compactness of the planar folded dipole antenna, small e is desirable.

Figure 3.10 shows the simulated bandwidth when parameter w_2 and w_1 are simultaneously varied while $d = 2$ mm are fixed. Figures 3.10(a), (b) and (c) are for $e = 2$, 8, and 16 mm, respectively. When e is small as shown in Fig.3.10(a), $w_2 \approx$ 32 mm and small w_1 values are the best for wideband properties. However, as shown in Figs.3.10(b) and (c), w_2 and w_1 values for the bandwidth over 50 % is increased when e is increased. Therefore, e shall be kept small to obtain a compact antenna that is the same as indicated in Fig.3.9.

In Figs.3.10(b) and (c), tendencies such as the tradeoff between w_2 and w_1 are observed. For example, both $w_2 = 40$ mm and $w_1 = 4$ mm or $w_2 = 36$ mm and $w_1 = 8$ mm are the conditions for the bandwidth over 50 % in Fig.3.10(c). In both cases, $w_2 + w_1$ is almost constant (44 mm). For the wideband properties, w_2 shall be increased when w_1 is decreased and vice versa, in these conditions.

Experimental Results

In consideration of the studies in the former subsections, we selected construction parameters $w_1 = 4$ mm, $w_2 = 32$ mm, $d = 2$ mm and $e = 2$ mm for the compact and

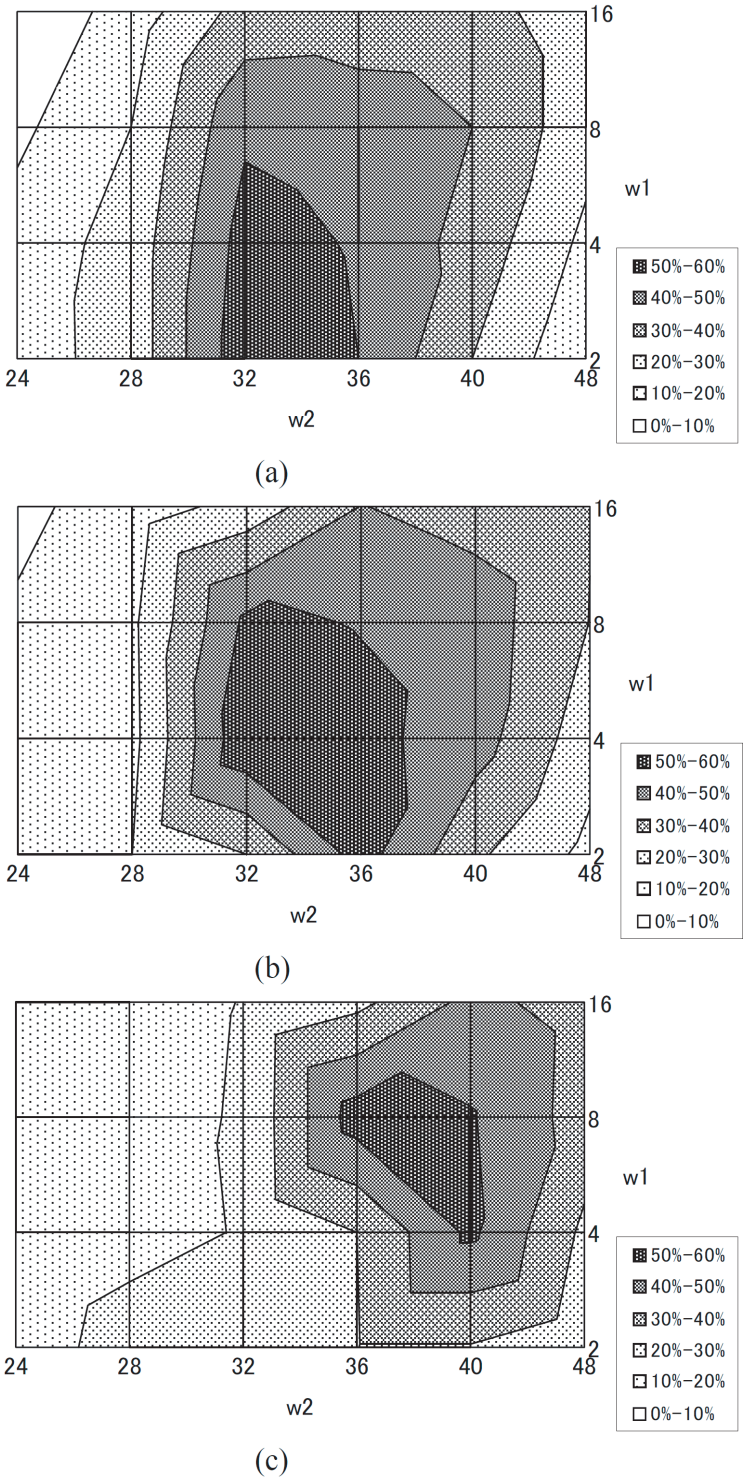

Figure 3.10: Simulated bandwidth (in %) of a planar folded dipole antenna with the variation of w_2 and w_1 (a) $e = 2$ mm, (b) $e = 8$ mm, and (c) $e = 16$ mm ($d = 2$ mm for all).

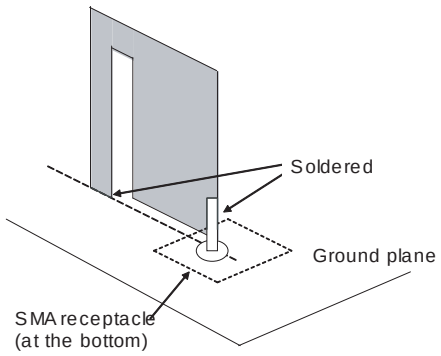

Figure 3.11: An antenna structure with a ground plane for the impedance measurement (balanced feed).

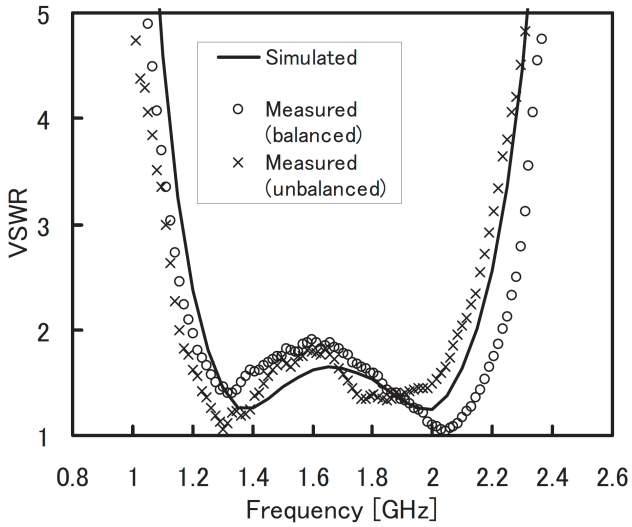

Figure 3.12: Measured and simulated VSWR of a planar folded dipole antenna.

wideband properties. We made two prototypes of planar folded dipole antennas for the impedance measurement. The one has the structure shown in Fig.3.7 (hereinafter referred to as the normal structure) used for the radiation pattern measurement. In this case, the antenna is fed by a coaxial cable without a balun, so an unbalanced feed is used here.

The other has the antenna structure with a ground plane for the balanced feed shown in Fig.3.11. In this case, due to the symmetry of the dipole antenna shown in Fig.3.7 the half portion of the antenna is made on the ground plane as shown in Fig.3.11. The size of the ground plane is around 300 mm x 300 mm and the antenna is attached at the center. The measured impedance is doubled for the compensation so the model is equivalent to the antenna with a wideband balun.

Figure 3.12 shows the measured and simulated voltage standing wave ratio (VSWR).

The measured and simulated results are in good agreement and exhibit wideband properties. The measured results by the balanced feed and the unbalanced feed agree well so we suppose that the antenna is self-balanced in the wide frequency band. The resonance frequencies of the unbalanced feed structure have a tendency to be lower than those of the balanced one. We think that this is caused by the parallel feed lines of approximately 5 mm length with the unbalance feed (no ground plane). The frequency ranges for VSWR ≤ 2 are from 1.2 GHz to 2.23 GHz for the balanced feed and 1.16 GHz to 2.09 GHz for the unbalanced feed, respectively. The bandwidths are 60 % and 57 % for the balanced and the unbalanced feed, respectively. The simulated bandwidth is 55 % where the antenna feed is assumed a balanced one.

3.3.3 Radiation Pattern

Figure 3.13 shows the radiation patterns of the planar folded dipole (normal structure) antenna at three frequencies. The construction parameters are the same as described in Section 3.3.2 so the frequencies 1.25G, 1.65G and 2.10 GHz are selected in the band with VSWR ≤ 2 (Fig.3.12). Simulated (a balanced feed), and measured (with and without a balun) results are plotted together for comparison. The intensity level is indicated with respect to the antenna gain in dBi.

In the x-z plane, the simulated and measured main polarization components (E_θ) are in good agreement, both with and without a balun. However, for the cross polarization component (E_ϕ), the measured results without a balun are stronger than the simulated results, although the measured results with a balun agreed well with the simulated results. The antenna has a self-balanced property because of wideband impedance matching for 50 ohms, as described in Section3.3.2. However, as described above, the self-balanced impedance property does not reduce the cross polarization component without a balun. The E_ϕs without balun are mainly created by currents flowing on the outside of coaxial cable, so the measured value can be changed by realigning coaxial cable. The balun used here has a insertion loss of around 1 dB, so the measured E_θs with the bulun are a little bit smaller than the measured E_θs without the bulun.

In the cases of the y-z and x-y plane patterns, the main polarization components (E_ϕ) measured with and without the balun agreed well with those simulated. However, in these cases, the differences between the three results are much bigger than those in the case of the x-z plane pattern. This is because the antenna feeding coaxial cable is laid along the y axis and has effects on the radiated electromagnetic field including the y axis. As the coaxial cable is located along the -y axis direction as shown in Fig.3.7, the differences between the simulated and the measured results have tendencies to be larger in the -y region than in the +y region. The simulated cross polarization components (E_θ) for the y-z and x-y plane are not appeared in Fig.3.13 since they are less than -40 dBi. However, in the y-z plane, the E_θs with the balun are much smaller than E_θs without the balun.

As a whole, as shown in Fig.3.13, the planar folded dipole antenna has radiation

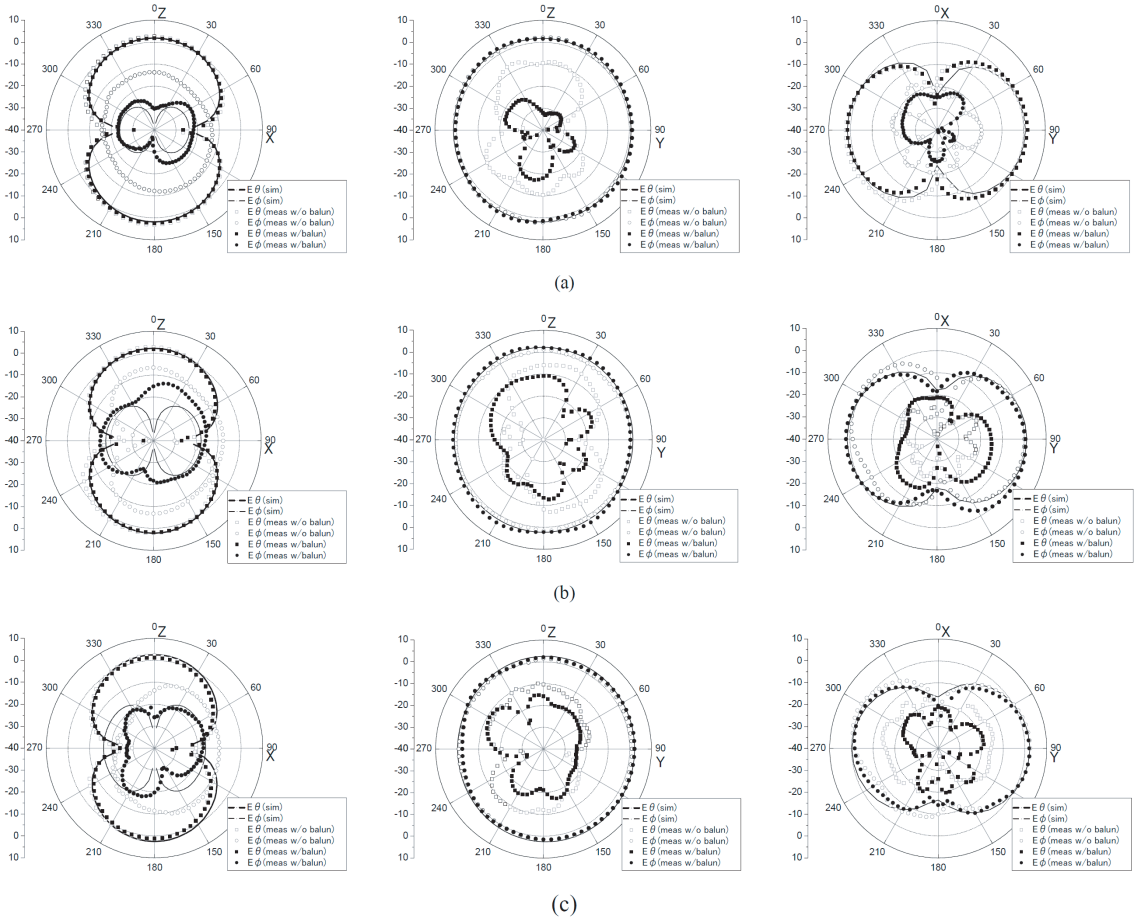

Figure 3.13: Measured and simulated radiation patterns of a planar folded dipole antenna at (a) 1.25 GHz, (b) 1.65 GHz, and (c) 2.10 GHz.

patterns similar to those of a normal dipole antenna in the wide frequency range except the cross polarization component. The simulated and measured (without the balun) antenna gain for the E_θs in the x-z plane are summarized in Table 3.2.

3.3.4 Current Distribution and Studies on Wideband Mechanizm

Figure 3.14 shows simulated current distributions on the planar folded dipole antenna. Figure 3.14(a) is for 2.00 GHz and Fig.3.14(b) is for 1.35 GHz. As is found from Fig.3.12, the minimum VSWRs are obtained at these frequencies. The arrows show the vector of the current flow. As shown in Fig.3.14(a) at 2.00 GHz, the current is dominant along the T-shaped slit edges of the antenna. The directions of the currents are anti-parallel in the narrow strip (width = w_1) and in the wide strip (width = w_2)

Table 3.2: Antenna gain of a planar folded dipole antenna.

Frequency	1.25 GHz	1.65 GHz	2.10 GHz
Simulated	1.9 dBi	2.2 dBi	2.5 dBi
Measured w/o balun	2.5 dBi	2.7 dBi	2.2 dBi

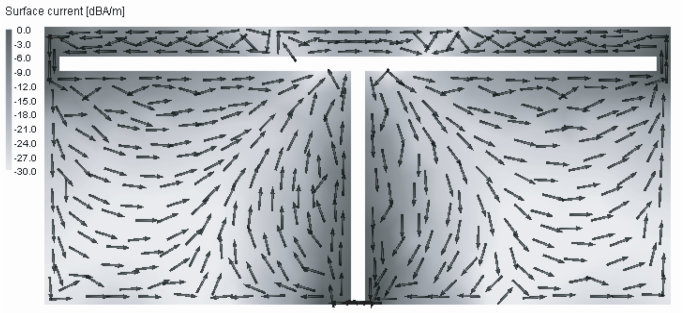

(a) at 2.00GHz

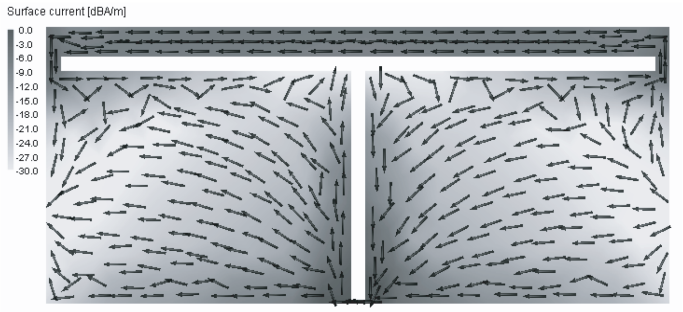

(b) at 1.35GHz

Figure 3.14: Simulated current distribution on a planar folded dipole antenna.

along slit, so the antenna is in transmission line mode at 2 GHz. However, as is shown in Fig.3.13(c), the antenna radiates. So the radiation mechanism at this frequency is considered to be different from folded dipole antenna. As shown in Fig.3.14(b) at 1.35 GHz the main current flows along the bottom side of in the wide strip and the narrow strip. The directions of the currents are same in the narrow strip and in most of the wide strip (mainly at the bottom portion), so we can say that the folded dipole antenna is in antenna mode at this frequency.

In order to investigate these current distributions in detail, we simulated two antenna elements named construction A and construction B. The antenna constructions A and B are shown in Fig.3.15(a) and Fig.3.15(b), respectively. The simulated VSWRS of these antenna elements are shown in Fig.3.15(c). It is shown that construction A has resonance at 2.1 GHz. So we can say that the higher order resonance

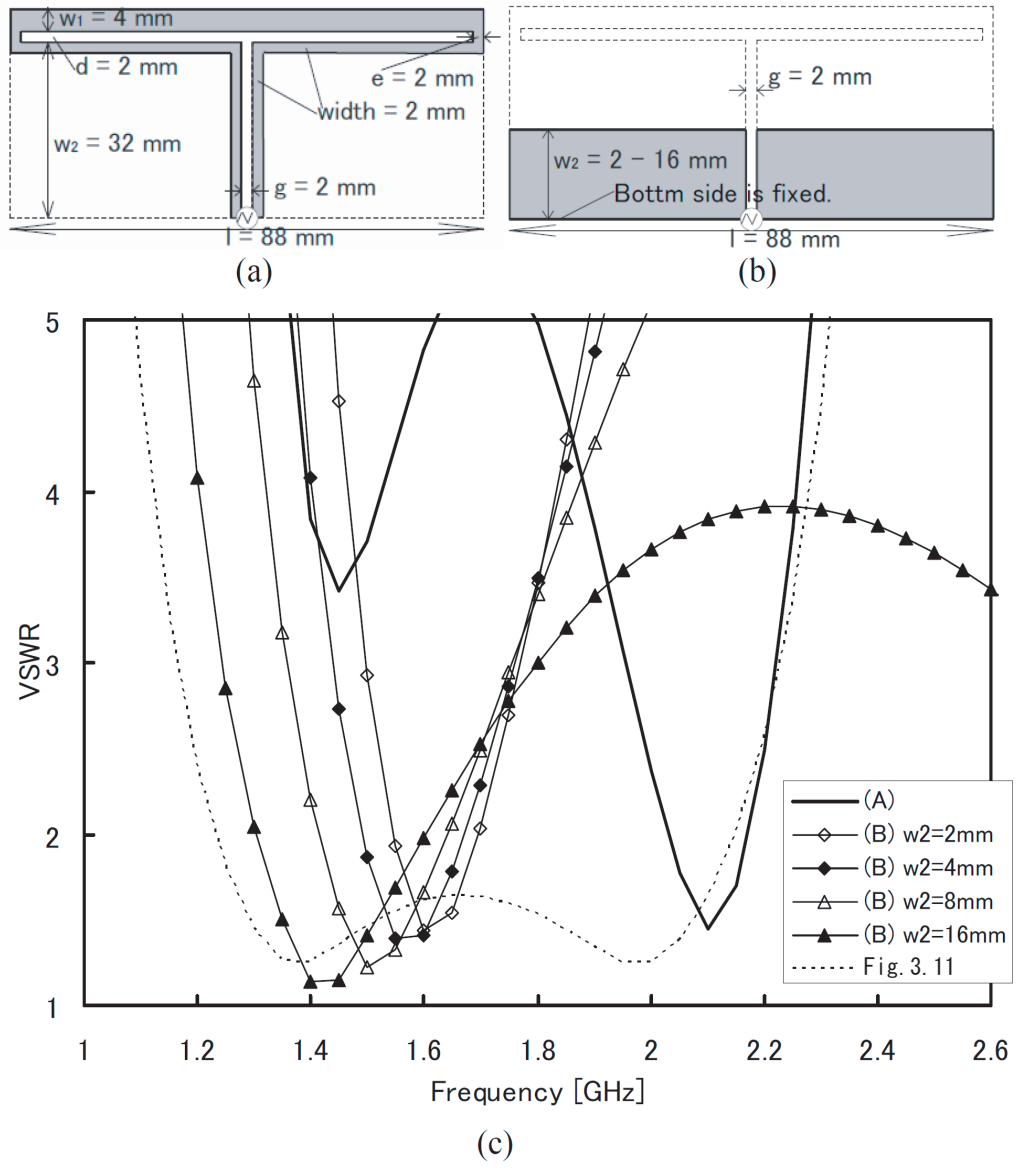

Figure 3.15: Decomposition of a planar folded dipole antenna to (a) construction A and (b) construction B, and (c) their simulated VSWRs.

at 2.00 GHz is mainly caused by the construction A. For construction B, bandwidth is increased when dipole width w_2 is increased. It is found that the resonance frequency is 1.4 GHz when $w_2 = 16$ mm. So we can say that the lower order resonance at 1.35 GHz is mainly caused by the antenna mode shown in Fig.3.14(b), that is based on the dipole antenna shown in the construction B. It is considered that the mechanism of the wideband operation of this folded dipole antenna is caused by the combination of these two constructions. The VSWR of the folded dipole antenna shown in Fig.3.12 is also plotted in Fig.3.15 as a reference.

3.4 Conclusion

A folded loop antenna and a planer folded dipole antenna with wideband characteristics are proposed. Both antennas have same characteristics, so the folded loop antenna is suitable for compact applications and the folded dipole antenna is suitable for planer applications. The antenna have simple planar construction without a ground plane and are easy to be assembled. Parameters for wideband and compact properties are found by using an electromagnetic simulator based on the method of moments. Experimental results centered at 1.7 GHz for 50 ohms impedance matching show that the antenna has the bandwidth of more than 55 % (VSWR *leq* 2). The simulated and experimental results are in good agreement, and the gains of the antenna are almost constant (around 2 dBi) in this frequency band. The radiation patterns are very similar to a normal dipole antenna except cross polarization components, and it is also found that the antenna has a self-balanced impedance property in this frequency band. The antenna is expected to be the powerful solution for the wideband wireless communication systems.

3.5 References

[3.1] M.Z.Win and R.A.Scholtz, "Ultra-wide band-width time-hopping spread-spectrum impulse radio for wireless multiple-access communications," IEEE Trans. Commun., vol.48, no.4, pp. 679-691, April 2000.

[3.2] R.J.Fontana, "Recent system applications of short-pulse ultra-wideband (UWB) technology," IEEE Trans. Microwave Theory & Tech., vol.52, no.9, pp. 2087-2104, September 2004.

[3.3] O.Yamada, H.Miyazawa, and J.Kumada, "Development of digital broadcasting in Japan," IEICE Trans. Electron., vol.E81-C, no.5, pp.636-641, May 1998.

[3.4] S.Matsuzawa, K.Sato, and K.Nishikawa, "Study of on-glass mobile antennas for digital terrestrial television," IEICE Trans. Commun., vol.E88-B, no.7, pp.3094-3096, July 2005.

[3.5] H.Morishita, Y.Kim, and K.Fujimoto, "Design concept of antenna for small mobile terminals and the future perspective," IEEE Antennas & Propag. Mag., vol.44, no.5, pp. 30-42, October 2002.

[3.6] S.Sekine, H.Shoki, and H.Morishita, "Antennas for wireless terminals," IEICE Trans. Commun., vol.E86-B, no.3, pp. 1005-1015, March 2003.

[3.7] Y. Kim, H. Morishita, Y. Koyanagi, K. Fujimoto, "A Folded loop antenna system for handsets developed and based on the advanced design concept," IEICE Trans. Commun., vol. E84-B, no.9, pp.2468-2475, Sep. 2001.

[3.8] S. Hayashida, H. Morishita, Y. Koyanagi, K.Fujimoto, "Wideband folded loop antenna for handsets," IEEE AP-S Int. Symp. Proc., pp.440-443, 2002.

[3.9] S. Hayashida, H. Morishita, K.Fujimoto, "A wideband folded loop antenna for handsets," IEICE Trans. Commun., vol. J86-B, no.9, pp.1799-1805, Sep. 2003.

[3.10] S.Tanaka, S.Hayashida, H.Morishita, and Y.Atsumi, "Wideband and compact folded loop antenna," IEE Electron. Letters, Vol.41, No.17, pp.945-946, August 18, 2005.

[3.11] S.Tanaka, Y.Kim, A.Matsuzaki, S.Hayashida, H.Morishita, Y.Atsumi and Y.Ido, "Wideband folded loop and folded dipole antennas," IEEE AP-S Int. Symp. Proc., pp.3711-3714, June 2006.

[3.12] C.W.Harrison, Jr and R.W.P.King, "Folded dipoles and loops," IRE Trans. Antenna & Propagation, vol. AP-9, no.2, pp.171-187, March 1961.

[3.13] G.A.Thiele, P.Ekelman, Jr. and L.W.Henderson, "On the accuracy of the transmission line model of the folded dipole," IEEE Trans. Antenna & Propagation, vol. AP-28, no.5, pp.700-703, September 1980.

[3.14] Ross W. Lampe, "Design formulas for an asymmetric coplanar strip folded dipole," IEEE Trans. Antenna & Propagation, vol. AP-33, no.9, pp.1028-1030, September 1985. (See correction, vol. AP-34, no.4, p.611, April 1986.)

[3.15] H.K.Schuman, "Modeling folded dipoles and feedlines for radiation and scattering," IEEE Trans. Antenna & Propagation, vol. AP-38, no.1, pp.30-39, January 1990.

[3.16] J.D.Krauss and R.J.Marhefka, "Antennas 3rd edition," McGraw-hill, 2001.

[3.17] H.Uchida and Y.Mushiake, "VHF- antenna,"Corona Publishing, Japan, 1961.

[3.18] Y.Okano,"A simple shape broadband planar antenna adaptable to RFID-tag," IEEE Trans. Antenna & Propagation, vol.54, no.6, pp.1885-1888, June 2006.

[3.19] S.Tanaka, Y.Kim, A.Matsuzaki, S.Hayashida, H.Morishita, Y.Atsumi and Y.Ido, "Wideband folded loop and folded dipole antennas," Proc. IEEE Antennas & Propagarion Society Int. Symp. (AP-S), pp.3711-3714, July 2006.

[3.20] S.Tanaka, Y.Kim, H.Morishita, S.Horiuchi, Y.Atsumi and Y.Ido,"Wideband planar folded dipole antenna with self-balanced impedance property," IEEE Trans. Antenna & Propagation, vol.56, no.5, pp.1223-1228, May 2008.

[3.21] R.F.Harrington, "Field computation by moment methods," Macmillan Company, 1968.

Chapter 4

Predistortion Type Equi-Path Linearizer for Radio-on-Fiber (RoF) System

A predistortion type equi-path linearizer is created for a radio-on-fiber system based on W-CDMA; its main benefit is its simple optical circuit configuration. Experiments show that the phase difference between the carrier and the third order intermodulation component of the laser diodes is shifted by around 90 degrees from that of the RF amplifier. To our knowledge, this is the first report to describe this phase shift, which is observed with both Fabry-Perot and distributed feedback laser diodes. To counter this shift we use additional phase shifters. The proposed design places a pre-amplifier between the linearizer and the laser diode for lower power consumption and better insertion gain at the linearizer. Experimental and calculated results agree well, and more than 20 dB improvement in the third order intermodulation components is obtained over the bandwidth of 60 MHz. The linearizer works well in the temperature range of 10 ℃to 40 ℃with a simple control circuit.

4.1 Introduction

Radio-on-fiber (RoF) systems are widely used for wireless communication networks [4.1]–[4.3] and various linearization techniques have been created to reduce the nonlinear distortions generated by the use of laser diodes (LDs). The feedforward technique is superior since it offers a large improvement in the third order intermodulation (IM3) components and less intensity noise [4.4]–[4.5]. However, it has a drawback in that it requires additional optical components such as a laser diode, a photodiode (PD), and optical couplers. Predistortion with diodes is a simple approach but it offers less improvement in IM3 components than the feedforward technique [4.6]–[4.7]. Moreover, these techniques need complex control circuits to handle the temperature changes expected and these circuits consume a lot of power [4.8]–[4.9]. There is strong de-

mand for a linearizer that has a simple optical circuit configuration, a minimal control circuit, and a large improvement in IM3 components.

This Chapter proposes an RoF system with a predistortion type equi-path (PTEP) linearizer [4.10]. The PTEP linearizer uses predistortion and demonstrates good temperature characteristics without a control circuit. As an example, the linearizer is combined with a Fabry-Perot LD for a W-CDMA RoF system. Fabry-Perot LDs are cost-effective but their distortion characteristics are worse than those of distributed feedback (DFB) LDs. Our target is to improve the IM3 components by more than 10 dB, and to realize an RoF system for W-CDMA around a Fabry-Perot LD instead of a DFB-LD.

Section 4.2 describes the circuit configuration and design method of the PTEP linearizer for an RoF system. In addition to approximated calculation [4.11], calculation without approximation is discussed for the linearizer design. Experiments on a linearizer with two types of LDs are presented in Section 4.3; one is Farby-Perot [4.11] and the other is a DFB-LD. The distortion characteristics with non-modulated two tone carriers [4.11] as well as a CDMA modulated carrier are shown. The observed phase shift of the phase difference between the carrier and the IM3 component seen in both types of LDs is discussed in Section 4.4 in more detail than is provided in [4.11].

4.2 Circuit Configuration and Design Method

4.2.1 Circuit Configuration of the Linearizer

Figure 4.1 shows the circuit configuration of the proposed PTEP linearizer with RoF link (LD, PD and optical fiber). The parameters of each device are shown in the inset. At the linearizer, the input signal is split into two paths by a branch line coupler (BL-1) [4.12]. One drives a predistortion amplifier (Amplifier-1) and the other drives Amplifier-2. Amplifier-1 and Amplifier-2 have the same characteristics and are accompanied by the same attenuator (Attenuator-1 and Attenuator-2). Amplifier-1 is followed by Attenuator-1 and Attenuator-2 is followed by Amplifier-2, so the two signals have the same carrier level but different IM3 component level. When these two signals through couplers are combined at BL-2 their phase difference equals 180 degrees, so the carrier signals cancel each other and only the distortion components remain. Hence this path is called the distortion path. The signal from Amplifier-2 is split into two, one is sent to the distortion path with BL-2 and the other to the linear path with BL-3. At BL-4, signals from the distortion path and linear path are combined with 180 degree phase difference, so the carrier signals and the IM3 components of the output signal have opposite phases. The signal output by the linearizer drives the RoF link.

As is shown in Fig.4.1, the distortion path and linear path consist of the same elements, so temperature changes do not alter the phase difference. Attenuator-3 is

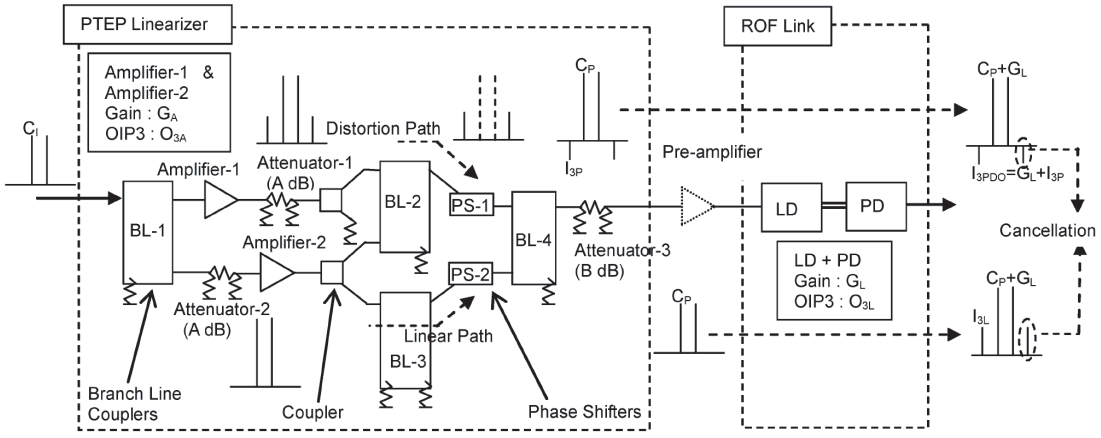

Figure 4.1: Circuit configuration of PTEP linearizer with RoF link.

used for power level adjustment. The pre-amplifier between the linearizer and the RoF link and phase shifters PS-1 and PS-2 are newly employed from [4.10]. The role of the pre-amplifier is described in the next subsection. The role of PS-1 and PS-2 is discussed in Section 4.4.

4.2.2 Calculation of Power Levels

Assuming that the insertion losses of all couplers (including BLs) in Fig.4.1 is 3 dB and the pre-amplifier is not used, we can calculate the power (in dBm) of carriers (C_P) and IM3 components (I_{3P}) at the output of PTEP linearizer as follows;

$$C_P = C_I + G_A - A - B - 12 \tag{4.1}$$

$$I_{3P} = -2O_{3A} + 3C_I - A + 3G_A - B - 18 + 2L + 20\log(1 - 10^{(-A-L)/10}) \tag{4.2}$$

$$\approx -2O_{3A} + 3C_I - A + 3G_A - B - 18 \tag{4.3}$$

where C_I is carrier power at input (dBm), A is the attenuation of Attenuator-1 and Attenuator-2 (dB), B is the attenuation of Attenuator-3 (dB), G_A is gain of Amplifier-1 and Amplifier-2 (dB), O_{3A} is 3rd output intercept point (OIP3) of Amplifier-1 and Amplifier-2 (dBm), L is $10\log(1-10^{-A/10})$; the approximation in (4.2) is reasonable assuming that A is large enough. Assuming also that the gain and OIP3 of the RoF link are G_L and O_{3L} respectively, the power of predistorted IM3 components at the output of the RoF link (I_{3PDO}) is

$$I_{3PDO} = G_L + I_{3PD}$$

$$= -2O_{3A} + 3C_I - A + 3G_A - B - 18 + G_L + 2L + 20\log(1 - 10^{(-A-L)/10}) \tag{4.4}$$

$$\approx -2O_{3A} + 3C_I - A + 3G_A - B - 18 + G_L \tag{4.5}$$

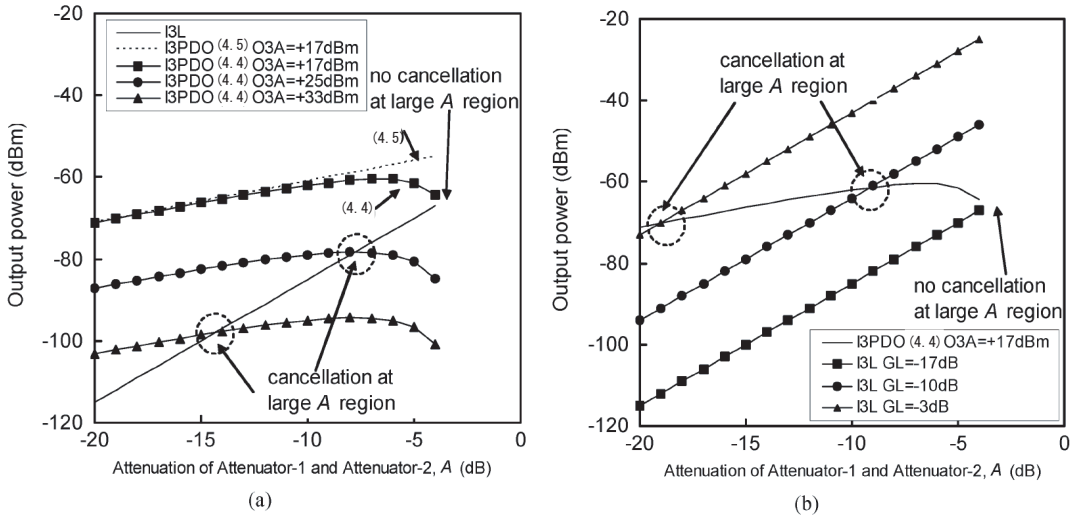

Figure 4.2: Calculated power of predistorted IM3 components at the output of the RoF link (I_{3PDO}) and IM3 component power at the output of the RoF link (I_{3L}) versus the attenuation value of Attenuator-1 and Attenuator-2 (A) for (a) various OIP3 of Amplifier-1 and Amplifier-2 (O_{SA}) and (b) various gain of the RoF link (G_L).

IM3 component power (I_{3L}), at the output of the RoF link is, when two tone carriers of C_P (dBm) without distortion are input, given by

$$I_{3L} = -2O_{3L} + 3C_I - 3A + 3G_A - 3B - 36 + 3G_L \tag{4.6}$$

The requirement for IM3 component cancellation is (4.4) = (4.6).

Figure 4.2(a) shows the calculated power of predistorted IM3 components at the output of the RoF link (I_{3PDO}) and IM3 component power at the output of the RoF link (I_{3L}) using (4.4) and (4.6) versus the attenuation value of Attenuator-1 and Attenuator-2 (A), for various OIP3 of Amplifier-1 and Amplifier-2 (O_{3A}). Our prototypes used an RoF link with G_L (gain) = -17 dB and O_{3L} (OIP3) = -7dBm, and Amplifier-1 and Amplifier-2 with G_A (gain) = 21 dB and O_{3A} (OIP3) = +17 dBm. B = 0 dB, and input power = -15 dBm are assumed. Calculated I_{3PDO} by (4.5) when O_{3A} = +17 dBm is plotted together for reference. As shown in Fig.4.2(a), I_{3PDO} by (4.4) degrades quickly for smaller A due to the effect of the last two terms in (4.4). This degraded region is unstable so large A values are desirable for stable operation. When A is large enough, the deviations between (4.4) and (4.5) are negligible. Fig.4.2(a) shows that there is no cancellation in the large A region when O_{3A} = +17 dBm, and large O_{3A}(OIP3 of Amplifier-1 and Amplifier-2) is necessary for cancellation. However, enlarging O_{3A} means increasing the power consumption of the linearizer.

Table 4.1: Required specifications for RoF link.

IM3	-65 dBc
C/N	52 dB
bandwidth	2130 - 2150 MHz (20 MHz)
temperature range	10 ℃to 40 ℃

Another method for cancellation with these devices is to enlarge G_L (gain of the RoF link). Figure 4.2(b) shows the calculated I_{3PDO} and I_{3L} using (4.4) and (4.6) versus A for various gain of the ROF link (G_L). Cancellation in the large A region is observed for large G_L in Fig.4.2(b). To enlarge G_L, a pre-amplifier with gain = 22 dB and OIP3 = +36 dBm is employed between the linearizer and RoF link, as shown in Fig.4.1. This configuration enables to reduce O_{3A} (OIP3) for the two amplifiers by the insertion of one pre-amplifier. So in our case, the power consumption at the linearizer (including the pre-amplifier) is about 25 % lower than that of the configuration without a pre-amplifier. The pre-amplifier also gives the linearizer insertion gain, instead of insertion loss.

4.3 Experimental Results

The specifications for the RoF link (down link) of a W-CDMA RoF system are summarized in Table 4.1. An RoF link with Fabry-Perot LD, G_L = -17 dB and O_{3L} = -7 dBm in the 2140 MHz band when the bias current I_b = 18 mA and optical output power=2.5mW does not meet these specifications, so a large improvement in IM3 components is required. The carrier and IM3 were calculated using (4.1), (4.4) and (4.6). The attenuation values of Attenuator-1 and Attenuator-2, A are set to 15 dB and the value of Attenuator-3, B is adjusted in order to minimize the IM3 components.

The PTEP linearizer fabricated for the above RoF link is shown in Fig.4.3. A printed circuit board with dielectric constant ϵ_r = 3.45 and thickness = 0.8 mm was used to build for this prototype. The coupler proposed by E.J.Wilkinson [4.13] was employed.

Figure 4.4 shows the measured and calculated carrier and IM3 component of the RoF link employing the PTEP linearizer and Fabry-Perot LD; B is around 3dB and the insertion gain of the linearizer (including pre-amplifier) is around 13dB in this case. The measurement was done in the 2140 MHz band and two tone carriers at 2140 and 2145 MHz were injected; this represents a frequency separation Δf = 5 MHz. The data measured without the linearizer are also plotted for reference; it is shifted by 13 dB along the input axis, in order to match the carrier plot. A maximum

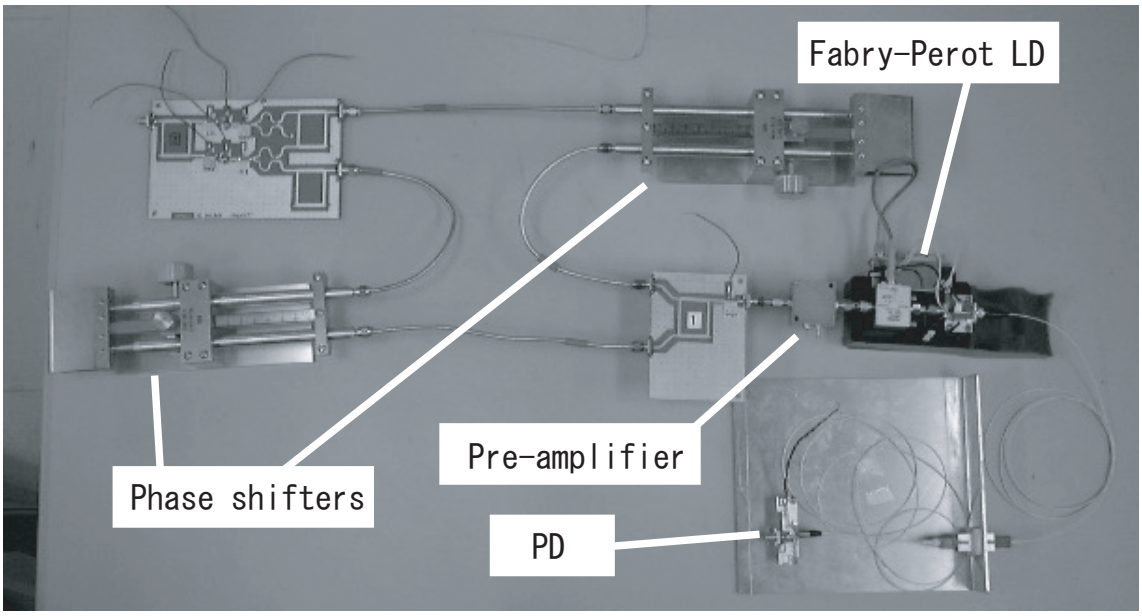

Figure 4.3: Fabricated PTEP linearizer with RoF link employing Fabry-Perot LD.

improvement of over 20 dB in IM3 components is observed in Fig.4.4. The measured and calculated carriers and IM3 components agree well with each other.

Figure 4.5 shows measured C/N and IM3 characteristics versus the optical modulation index (OMI). Without the PTEP linearizer, the Fabry-Perot LD used here cannot meet the specifications in Table 4.1. Since the proposed linearizer improves the IM3 components by more than 20 dB, the LD meets the specification with OMI range from 10 % to 30 %.

The PTEP linearizer does not alter the C/N. The measured noise level of RoF link itself (LD+PD) and that of the RoF link with the linearizer are the same, around -152 dBm/Hz. The measured noise level of the PTEP linearizer itself (including the pre-amplifier) is increased to around -142 dBm/Hz due the losses imposed by the couplers and attenuators. However, the RoF link with Fabry-Perot LD has large loss, around 17 dB, in this case, so the noise increase due to the PTEP linearizer is negligible.

Figure 4.6 shows frequency bandwidth characteristics of the PTEP linearizer. Frequency separation $\Delta f = 5$ MHz. With the linearizer, the IM3 components are improved by more than 20 dB in a bandwidth of greater than 60 MHz; the bandwidth specifications described in Table 4.1 are satisfied.

Figure 4.7 shows the measured carrier power and adjacent channel power (ACP) of a W-CDMA modulated signal passed through the ROF link. As the ACP is proportional to IM3 component, the ACP in Fig.4.7 has the same curve as the IM3 component in Fig.4.4. However, due to the noise level around -86 dBm with channel power measurement, it is degraded when ACP is under -80 dBm. The measured

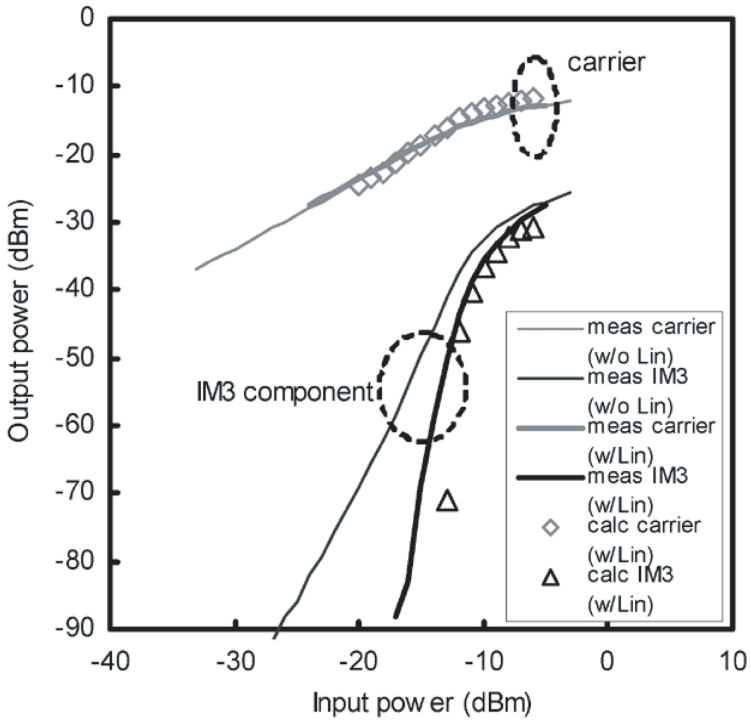

Figure 4.4: Measured and calculated carrier and IM3 component of RoF link employing PTEP linearizer and Fabry-Perot LD in the 2140 MHz band.

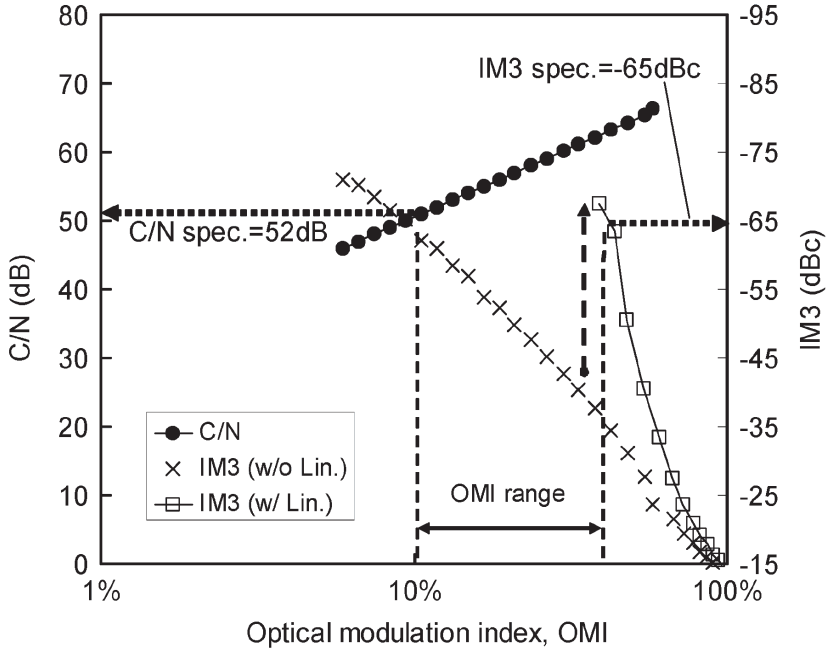

Figure 4.5: Measured C/N and IM3 characteristics versus the optical modulation index (OMI) with and without the linearizer.

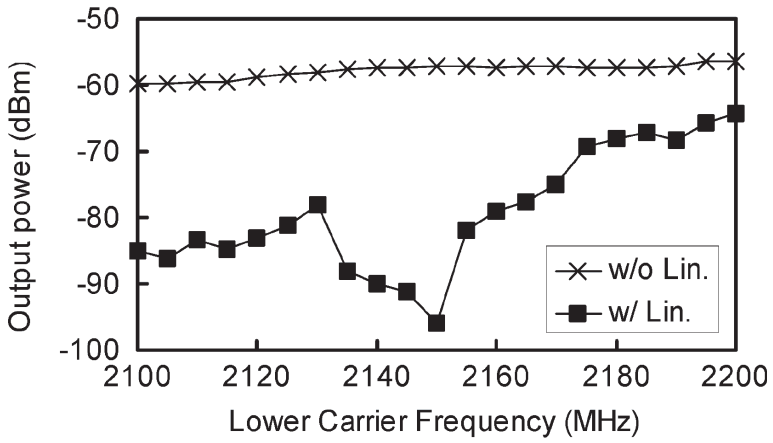

Figure 4.6: IM3 component versus frequency with and without the linearizer (input power = -17 dBm, frequency separation Δf = 5 MHz).

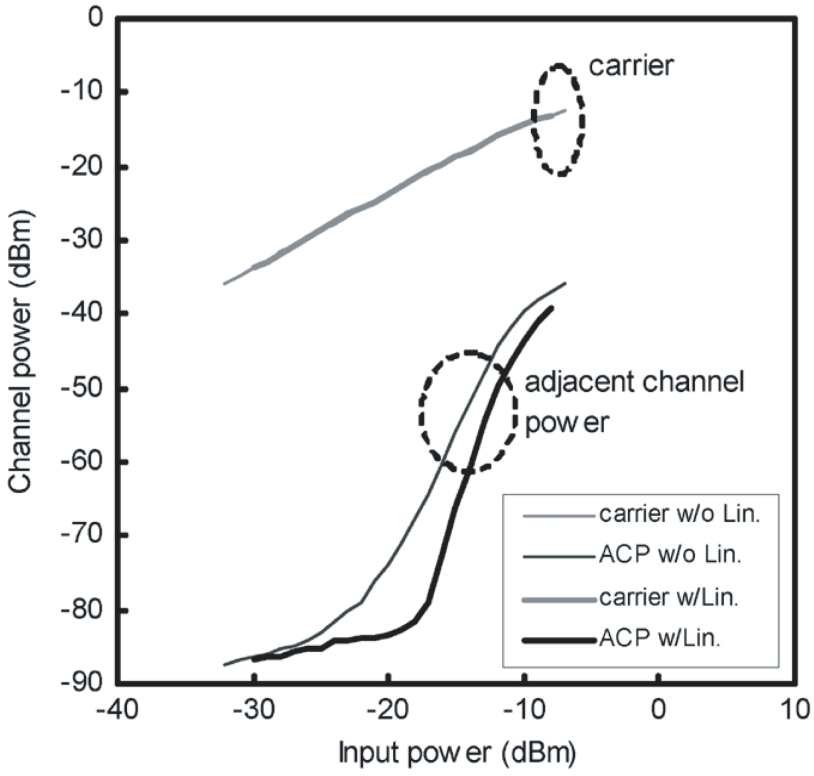

Figure 4.7: Measured carrier power and adjacent channel power of W-CDMA modulated signal through the RoF link with PTEP linearizer and Fabry-Perot LD.

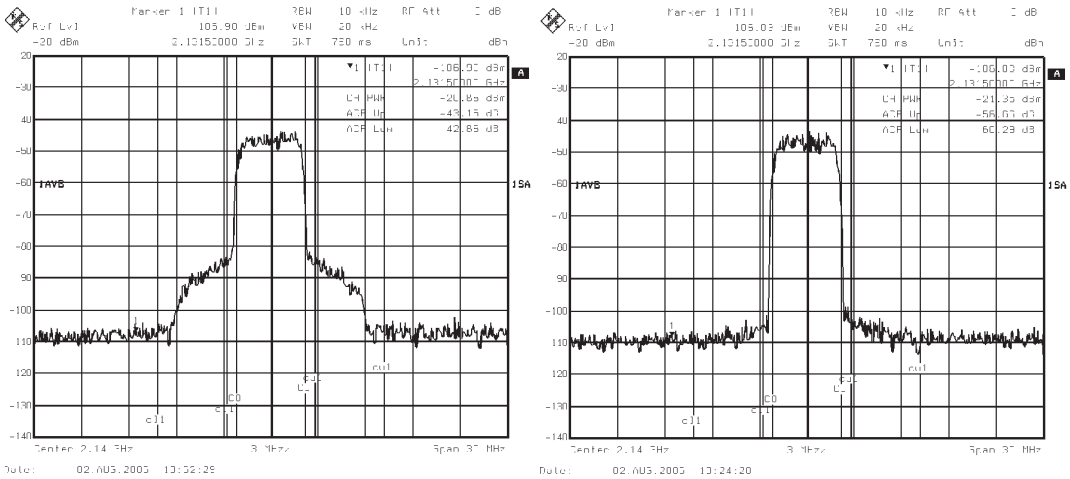

Figure 4.8: Measured spectra of W-CDMA modulated signal through the RoF link (a) without PTEP linearizer and (b) with PTEP linearizer.

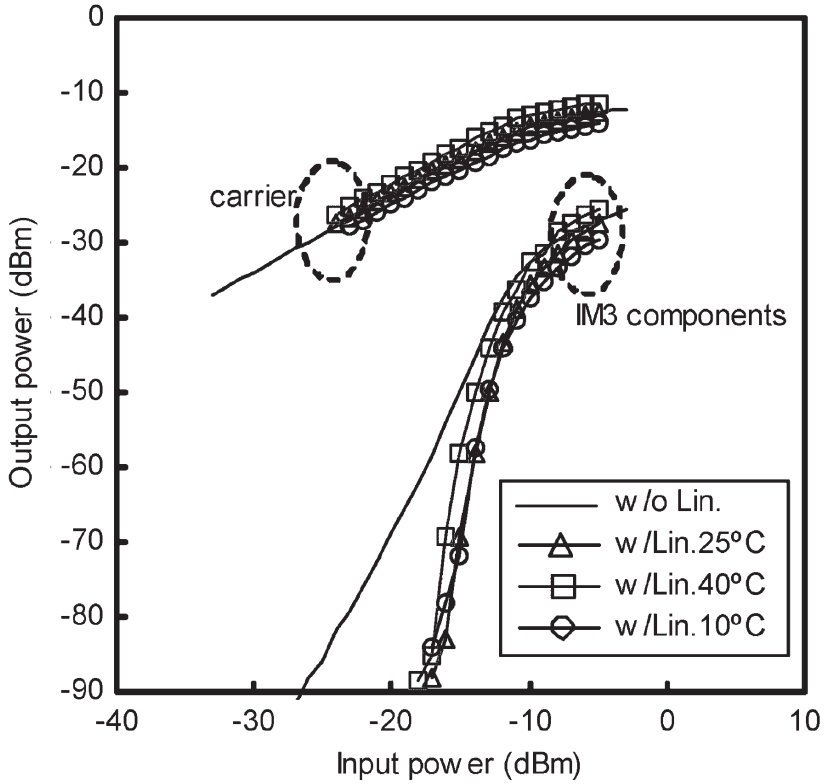

Figure 4.9: Measured temperature characteristics of the carrier and IM3 component of the RoF link with PTEP linearizer and Fabry-Perot LD.

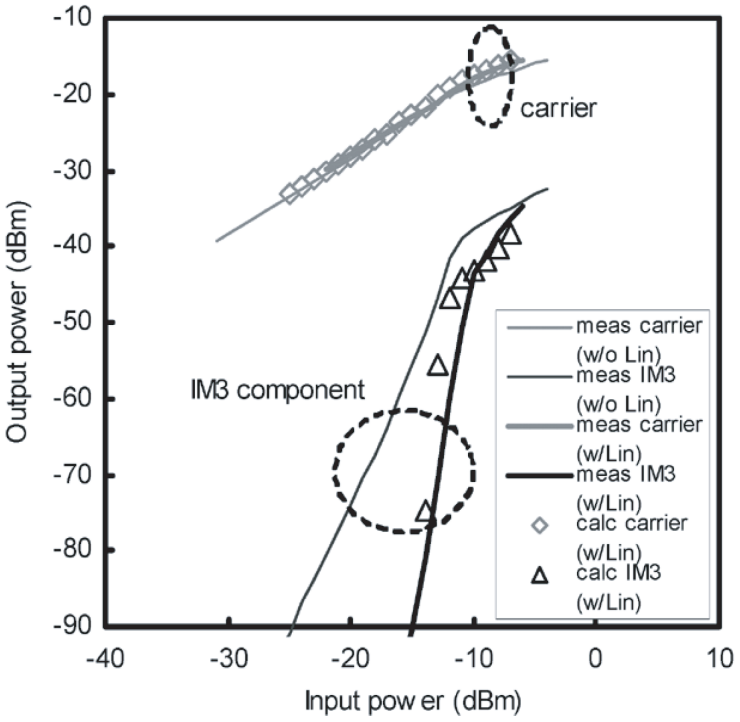

Figure 4.10: Measured and calculated carrier and IM3 component of RoF link employing PTEP linearizer and DFB-LD in the 2140 MHz band.

spectra of the W-CDMA modulated signal with and without the linearizer are shown in Fig.4.8. In Figs.4.8(a) and 4.8(b), the carrier power is the same to -21 dBm, and the ACP is -43 dBm without the linearizer and -59 dBm with the linearizer, respectively. As the ACP improvement by the linearizer is 16 dB due to a noise floor, it is observed that the peak of ACP is improved by around 20 dB from Fig.4.8. It is also found from Figs.4.7 and 4.8 that the noise level with the linearizer equals that without the linearizer, as mentioned above.

Fig.4.9 shows the measured temperature characteristics of the carrier and IM3 components of the RoF link with the PTEP linearizer. As the automatic temperature control circuit attached to the Fabry-Perot LD is not strong enough, the attenuation value B should be adjusted according to the temperature. However, the temperature stability can be realized by a simple control circuit. The variation of carrier level is 3 dB and the improvement of IM3 components is more than 20 dB from 10 ℃to 40 ℃.

The PTEP linearizer was also applied to a DFB-LD with G_L = -12 dB and O_{3L} = -5 dB in the 2140 MHz band when the bias current I_b = 20 mA. Figure 4.10 shows the measured and calculated carrier and IM3 component of the RoF link using the DFB-LD; B is around 12 dB and the insertion gain of the linearizer (including pre-amplifier) is around 4 dB in this case. The measured data without the linearizer are

also plotted for reference. Maximum improvement of over 20dB in IM3 component is also observed in Fig.4.8. The measured and calculated results agree with each other but not as well as with the Fabry-Perot LD. We suppose that this deviation is caused by the non-linear characteristics of the IM3 components of the DFB-LD when the input power is around -12 dBm.

4.4 Phase Delay of IM3 components

As shown in Fig.4.1, we added two phase shifters along the distortion and linear paths of the PTEP linearizer. These phase shifters are not necessary in a linearized RF amplifier, but are needed if LDs are used. Figure 4.11 shows measured carrier and IM3 component of the RoF link with the Fabry-Perot LD versus the phase difference between PS-1 and PS-2. Figure 4.11(a) is for 830 MHz band measurement and Fig.4.11(b) is for 2370 MHz band measurement when frequency separation Δf = 5 MHz, and input power level is -10 dBm. The calculated IM3 component from carrier level without the PTEP linearizer is also plotted for reference. Figure 4.11 indicates that the maximum improvement of IM3 components is observed when the phase difference is around 90 degrees for the Fabry-Perot LD, while it is observed when the phase difference is 0 degrees for RF amplifier. This suggests that the phase difference between the carrier and the IM3 components of the Fabry-Perot LD is shifted by around 90 degrees from the phase of the carrier. In other words, the phase difference between the carrier and the IM3 component is 270 degrees for the Fabry-Perot LD and 180 degrees for the RF amplifier. The results in Figs.4.4–4.9 were measured under this optimum phase difference.

In order to verify the above mentioned 90 degree phase shift in phase difference between carrier and IM3 component, we investigated the optimum phase difference at various RF frequencies. Figure 4.12 shows the optimum phase difference (measured) that maximizes the improvement in IM3 components as a function of RF frequency when frequency separation Δf = 5 MHz. As shown in Fig.4.12, a 90 degree phase difference is needed from 800 MHz to 2400 MHz for the Fabry-Perot LD. The slight deviations from 90 degrees observed in Fig.4.12 are thought to be caused by the measurement error of phase shifter.

Figure 4.13 shows the measured optimum phase difference as a function of frequency separation Δf. -10 dBm two tone carriers with center frequency 2140 MHz are injected, i.e., the upper carrier frequency is 2140 + $\Delta f/2$ (MHz) and the lower carrier frequency is 2140 - $\Delta f/2$ (MHz). Figure 4.13 indicates that the optimum phase difference is constant at around 90 degrees for all Δf values. The optimum phase difference to minimize upper frequency IM3 and lower frequency IM3 deviates when Δf is large, as the phase of upper and lower IM3 components deviates at large Δf. The optimum phase difference increases when Δf is large. We suppose this increase is due to the frequency-dependence of non-linearity in the directly-modulated LD [4.14] and the phase deviation created by the BLs.

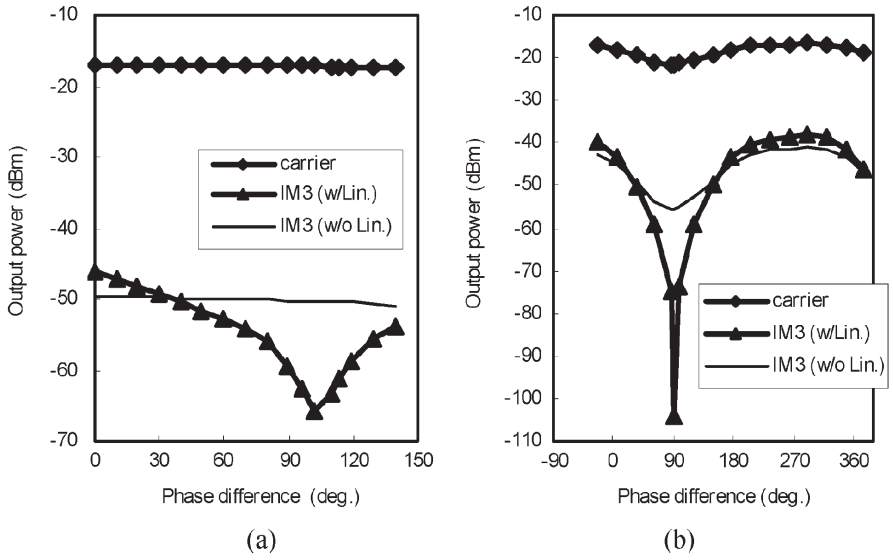

Figure 4.11: Measured carrier and IM3 component of RoF link employing PTEP linearizer and Fabry-Perot LD versus phase difference between PS-1 and PS-2 in the (a) 830 MHz band and (b) 2370 MHz band.

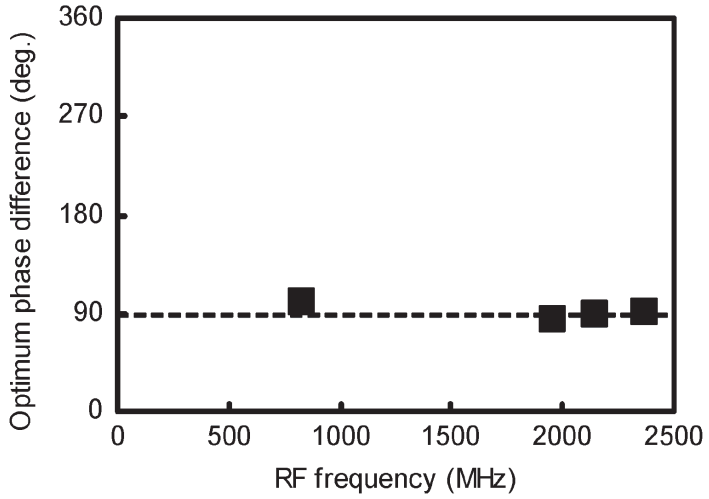

Figure 4.12: Measured optimum phase difference between PS-1 and PS-2 for Fabry-Perot LD versus RF frequency.

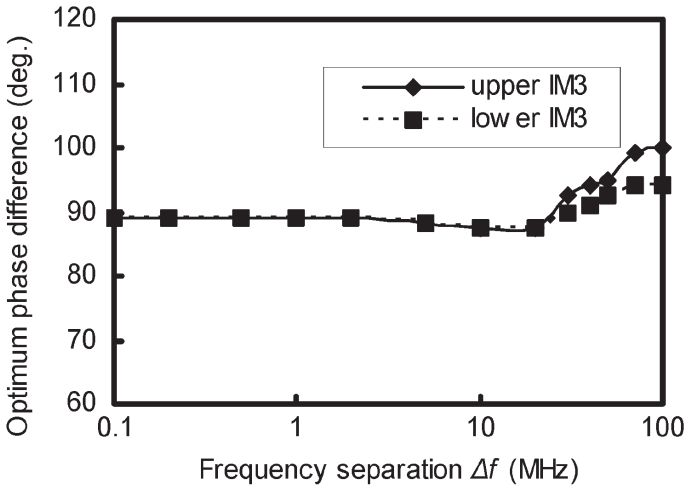

Figure 4.13: Measured optimum phase difference between PS-1 and PS-2 for Fabry-Perot LD versus frequency separation Δf.

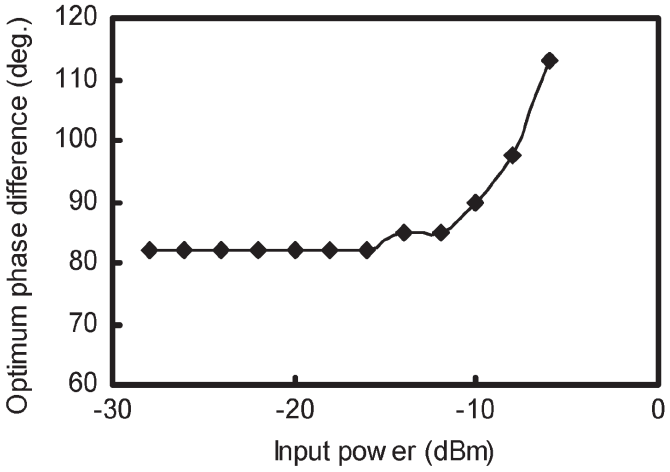

Figure 4.14: Measured phase difference between PS-1 and PS-2 for maximizing improvement in IM3 components for Fabry-Perot LD versus input power.

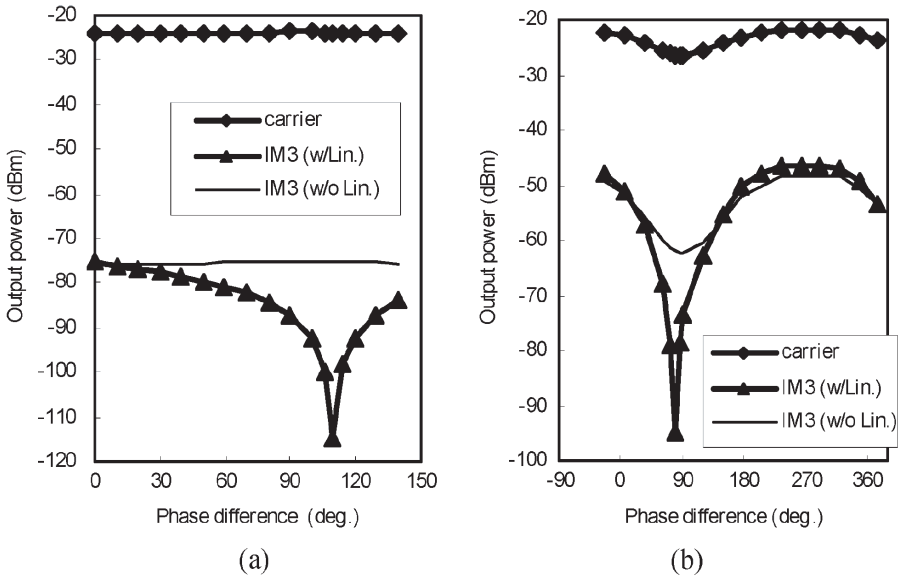

Figure 4.15: Measured phase difference between PS-1 and PS-2 for maximizing improvement in IM3 components for Fabry-Perot LD versus input power.

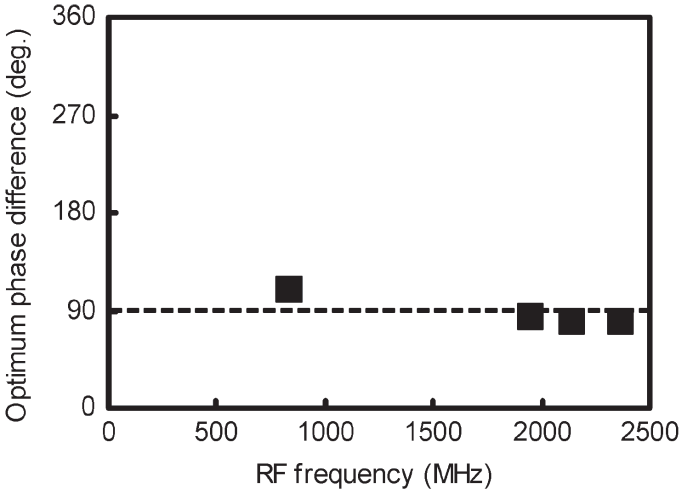

Figure 4.16: Measured optimum phase difference between PS-1 and PS-2 for DFB-LD versus RF frequency.

Figure 4.14 shows the measured optimum phase difference as a function of input power level. The measurement was done in the 2140 MHz band when $\Delta f = 5$ MHz and Fig.4.14 indicates that the optimum phase difference is constant at around 90 degrees for small input power levels. The optimum phase difference increases when the input power increases. We believe that this characteristic is mainly caused by the AM-PM conversion at high input power of Amplifier-1, Amplifier-2, the pre-amplifiers [4.9], and LD[4.15][4.16].

These phase shift characteristics were also investigated for the DFB-LD. Figure 4.15 shows measured carrier and IM3 component of the RoF link employing the DFB-LD versus the phase difference between PS-1 and PS-2 in the 830 MHz and 2370 MHz bands. Figure 4.16 shows the measured optimum phase difference that maximizes the improvement in IM3 components as a function of RF frequency when frequency separation $\Delta f = 5$ MHz. As shown in Fig.4.16, a phase difference of around 90 degrees is also needed from 800MHz to 2400MHz for the DFB-LD. Therefore, it is supposed that the 90 degree phase shift of the phase difference between the carrier and the IM3 component is an intrinsic characteristic of semi-conductor LDs. It is also assumed that the 90 degree phase shift is related to the phase distortion of vector modulated symbols after transmission through the ROF link at low power levels, as is reported in [4.16].

4.5 Conclusion

A predistortion type equi-path linearizer was combined with a Fabry-Perot LD for an RoF system based on W-CDMA. IM3 components are improved by over 20 dB in the RF frequency band of more than 60 MHz. The C/N level is not changed by the addition of the linearizer and the RoF link meets the specifications with OMI range from 10 % to 30 %. The proposed configuration exhibits good temperature stability from 10 to 40 ℃with a simple control circuit. It can be said that the improved stability is obtained by increasing the complexity of the RF circuit. However, compared to the feedforward technique (excluding temperature control circuit), the expensive optical portion is reduced and total circuit complexity is about the same. The circuit size is very large in our prototype shown in Fig.4.3, but it can be reduced by employing compact couplers and including additional phase shifters from the first design stage.

It is also found that the phase difference between the carrier and the IM3 component generated by the non-linearity of the Fabry-Perot and distributed feedback laser diode is shifted by 90 degrees from that of the RF amplifier. This is, to our knowledge, the first report of this phase shift. This 90 degree phase shift was validated in experiments at various RF frequencies, frequency separations, and input powers. The proposed linearizer will be a powerful incentive to adopt RoF systems.

4.6 References

[4.1] W.I.Way, "Optical fiber-based microcellular systems: an overview," IEICE Trans. Commun., vol.E76-B, no.9, pp. 1091-1102, September 1993.

[4.2] J.C.Fan, C.L.Lu and L.G.Kazovsky, "Dynamic range requirements for microcellular personal communication systems using analog fiber-optic links," IEEE Trans. Microwave Theory & Tech., vol.45, no.8, pp. 1390-1397, August 1997.

[4.3] T.Kuri and K.Kitayama, "Optical heterodyne detection of millimeter-wave-band radio-on-fiber signals with a remote dual-mode local light source," IEEE Trans. Microwave Theory & Tech., vol.49, no.10, pp. 2025-2029, October 2001.

[4.4] L.S.Fock, A.Kwan and R.S.Tucker, "Reduction of semiconductor laser intensity noise by feedforward compensation: experiment and theory," IEEE J. Lightwave Technol., vol.10, no.12, pp. 1919-1925, December 1992.

[4.5] D.Hassin and R.Vahldieck, "Feedforward linearization of analog modulated laser diodes - theoretical analysis and experimental verification," IEEE Trans. Microwave Theory & Tech., vol.41, no.12, pp. 2376-2382, December 1993.

[4.6] L.Roselli, V.Borgioni, F.Zepparelli, F.Ambrosi, M.Comez, P.Faccin and A.Casini, "Analog laser predistortion for multiservice radio-over-fiber systems," IEEE J. Lightwave Technol., vol.21, no.5, pp. 1211-1223, May 2003.

[4.7] R.A.Adb-Alhameed, P.S.Excell, J.G.Gardiner and N.T.Ari, "Volterra series analysis of a laser diode predistorter for mobile communication systems," Microwave J., vol.47, no.9, pp. 190-197, September 2004.

[4.8] P.B.Kenington, "High-Linearity RF Amplifier Design,"Artech House, 2000.

[4.9] N.Pothecary, "Feedforward Linear Power Amplifiers," Artech House, 1999.

[4.10] N.Suematsu, T.Takagi, A.Iida and S.Urasaki, "A predistortion type equi-path linearizer in Ku-band," The 3rd Asia-Pacific Microwave Conference Proc., pp. 1077-1080, 1990.

[4.11] S.Tanaka, N.Taguchi, T.Kimura and Y.Atsumi, "A predistortion type equi-path linearizer designed for radio-on-fiber system," 2005 IEEE MTT-S Int. Microwave Symp. Dig., TU1A-4, June 2005.

[4.12] J.Reed and J.Wheeler, "A method of analysis of symmetrical four-port networks," IRE Trans. Microwave Theory & Tech., Vol.4, No.5, pp.246-252, October 1956.

[4.13] E.J.Wilkinson, "An N-way hybrid power divider," IRE Trans. Microwave Theory & Tech., vol.8, no.1, pp. 116-118, January1960.

[4.14] R.Sadhwani and B.Jalali, "Adaptive COMS predistortion linearizer for fiber-optic links," IEEE J. Lightwave Technol., vol.21, no.12, pp. 3180-3193, December 2003.

[4.15] K.Yamauchi, K.Mori, M.Nakayama, Y.Mitsui and T.Takagi, "A microwave miniaturized linearizer using a parallel diode with a bias feed resistance," IEEE Trans. Microwave Theory & Tech., vol.45, no.12, pp. 831-834, December 1997.

[4.16] X.Fernand and A.Sesay, "Characteristics of directly modulated ROF links for wireless access," Proc. Canadian Conf. Electrical and Computer Engineering., vol.4, pp. 2167-2170, May 2004.

Chapter 5

Distortion Reduction Filters for Radio-on-Fiber (RoF) System

Three distortion reduction filters for radio-on-fiber systems are proposed and evaluated from the standpoint of improvements in out-of-band third order intermodulation (IM3) components (spurious components), insertion loss, temperature stability and so on. The basic filter configuration includes optical comb filter, RF (radiowave frequency) comb filter, and RF dual band rejection filter (DBRF). Experiments are conducted at 2 GHz band for frequency separation Δf = 5 MHz and 100 MHz in the temperature range of -10 ℃to +50 ℃. These filters can reduce IM3 components even in the saturation region, unlike conventional linearizers. An optical comb filter can reduce IM3 components more than 20 dB and noise level around 10 dB if its polarization controller is properly adjusted, but its insertion loss is large and stability against vibration is very poor. The proposed RF comb filter and RF-DBRF can reduce IM3 components by more than 20 dB and noise level by more than 3 dB. Their stability against vibration and temperature change is good, and insertion losses are 1-2 dB for Δf = 100 MHz.

5.1 Introduction

Radio-on-fiber (RoF) systems are widely used in wireless communication networks [5.1]–[5.4] and various linearization techniques have been applied in order to reduce the nonlinear distortion generated by the use of laser diodes (LDs). The feedforward technique is superior since it offers a large improvement in third order intermodulation (IM3) components and lower intensity noise [5.5][5.6]. However, it has a drawback in that it requires additional optical components such as a laser diode, a photodiode (PD), and optical couplers. Predistortion with diodes is a simple approach but it offers less improvement in IM3 components than the feedforward technique [5.7][5.8]. Additionally, these techniques need complex control circuits to handle temperature changes, and these circuits can consume a lot of power [5.9][5.10]. The predistortion

type equi-path technique has good temperature stability [5.11] but requires large RF circuit size as does the feedforward approach and control circuit is simplified but still needed, as described in Chapter 4. There is strong demand for a distortion cancellation technique that offers simple circuit configuration, no control circuit, and a large improvement in IM3 components.

A related trend is the continual increase in the required bandwidth for wireless communication systems. The required bandwidth is around 5 MHz for wideband code division multiple access (W-CDMA) systems, around 20 MHz for wireless local area network (W-LAN) systems, and over GHz for ultra wideband (UWB) systems [5.12]. Conventional linearization techniques have difficulty in covering such wide bands [5.9][5.10]. Given this background, filtering techniques composed of all passive devices will be effective. Filters can also meet the three above mentioned demands placed on distortion cancellers. Filtering techniques is only effective for reducing out-of-band IM3 (spurious) components; they are not effective for in-band IM3 components. Therefore, only spurious components are addressed this paper. However, the spurious components are the most critical component and are restricted by law. If in-band IM3 is critical in some application, a filtering technique accompanied with a simple and weak linearizer (e.g., diode predistortion) can be adopted.

In this chapter, we propose distortion reduction filters for RoF systems. The circuit configuration and design method of three kinds of filter, optical comb filter [5.13] based on the interferometer configuration [5.14][5.15], radio frequency (RF) comb filter, and RF dual band rejection filter (RF-DBRF) [5.16] are described in Section 5.2. RoF links with these filters are then evaluated and compared in Section 5.3, from the standpoint of improvement in IM3 components, insertion loss, noise level, temperature stability and so on. As an example, those filters are applied to an RoF link in the 2 GHz band. Frequency separation of signals (Δf), which is proportional to bandwidth, is evaluated at 5 MHz and 100 MHz. Our target is to obtain more than 10 dB improvement in IM3 components.

5.2 Circuit Configuration and Design Method

5.2.1 RoF Link with Optical Comb Filter

Figure 5.1(a) shows the circuit configurations of the proposed RoF link with optical comb filter. In the optical comb filter, the filter is composed of an optical divider, optical coupler, and two optical fiber paths with different lengths. The optical comb filter is placed between the LD and PD. Signals with IM3 components output by the LD are fed into the optical comb filter. The transmission characteristics of the comb filter have rejection frequencies at a regular interval which is adjustable by tuning the difference length of the short and long paths. The function of the polarization controller (PC) shown in Fig.5.1(a) is discussed in Section 5.3.1.

The phase angles of signals and IM3 components at three points (A, B and C) in

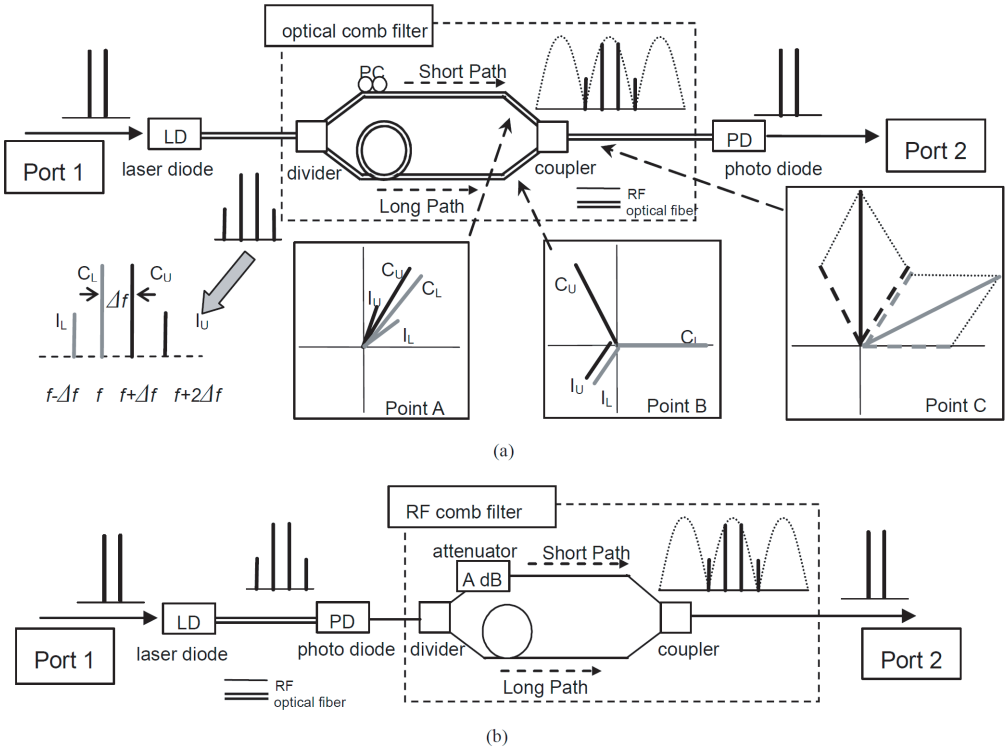

Figure 5.1: Circuit configuration of the RoF link employing (a) optical comb filter and (b) RF comb filter.

Fig.5.1(a) is shown in the inset. The function of the comb filter is explained from the standpoint of phase angles. If we can realize a 180 degree phase difference between the IM3 components at point A and those at B, the combined signal at point C will have no IM3 components. Assuming that the frequency (in MHz) of the two tone carriers are f and f+Δf as shown in Fig.5.1(a), the phase angle difference between the lower frequency IM3 component (I_L) and upper frequency IM3 component (I_U) shall be $360n$ degree (where n is a natural number) at point B. First, we have to find the electrical length of the long path (L_L) for this condition. As the wavelength λ [m] of frequency f is $300/f$ when f is expressed in MHz, the phase angles of I_L and I_U after transmission through L_L [m] are $360/300 \cdot L_L(f - \Delta f)$ and $360/300 \cdot L_L(f + 2\Delta f)$ [degrees], respectively. Therefore, the following L_L is needed

$$L_L = 100n/\Delta f[m]. \tag{5.1}$$

$n = 1$ is desirable to minimize L_L. In this condition, the phase angle of lower frequency carrier (C_L), upper frequency carrier (C_U), I_L and I_U at point B are expressed as (in

degrees)

$$Phase of I_L@B = 120f/\Delta f - 120 \tag{5.2}$$
$$Phase of C_L@B = 120f/\Delta f \tag{5.3}$$
$$Phase of C_U@B = 120f/\Delta f + 120 \tag{5.4}$$
$$Phase of I_U@B = 120f/\Delta f + 240. \tag{5.5}$$

Next, the electrical length of short path (L_S) is determined. The phase of the center frequency of the four components ($f + 0.5\Delta f$) shall be 180 degree different from (5.2) and (5.5), that is $120f/\Delta f + 60$ [degree]. This value can be more than 360 degrees, so in order to minimize L_S, rem (remainder of $(120f/\Delta f + 60)/360$) [degree] is employed. This means that the target L_S is expressed by

$$L_S = 5/[6(f + 0.5\Delta f)] \cdot rem[m]. \tag{5.6}$$

With this L_S, the phase angles of C_L, C_U, I_L and I_U at point A are expressed as (in degrees)

$$Phase of I_L@A = (f - \Delta f)/(f + 0.5\Delta f) \cdot rem \approx rem \tag{5.7}$$
$$Phase of C_L@A = f/(f + 0.5\Delta f) \cdot rem \approx rem \tag{5.8}$$
$$Phase of C_U@A = (f + \Delta f)/(f + 0.5\Delta f) \cdot rem \approx rem \tag{5.9}$$
$$Phase of C_U@A = (f + 2\Delta f)/(f + 0.5\Delta f) \cdot rem \approx rem. \tag{5.10}$$

The approximation in (5.7)–(5.10) is reasonable when $\Delta f \ll f$ and is useful in the shortening the design process since $\Delta f \ll f$ is normal in most radio communication systems. When Δf is close to f, the comb filter technique is not effective. Without this approximation, the phase deviation $\Delta\theta$ of IM3 components is expressed as

$$\Delta\theta = 1.5\Delta f/(f + 0.5\Delta f) \cdot rem[degree]. \tag{5.11}$$

According to (5.1), longer L_L is needed when Δf becomes narrow, however, the attenuation in the optical fiber is negligible and so is not an issue. On the other hand, when Δf becomes wide, the approximation in (5.7)–(5.10) is not reasonable and the phase difference of the IM3 components between point A and B deviates from 180 degrees. The IM3 cancellation level S_{IM3} with gain and phase deviations can be calculated as follows [5.9],

$$S_{IM3} = -10log[1 + 10(\Delta A/10) - 2 \cdot 10(\Delta A/20)cos(\Delta\theta)][dB] \tag{5.12}$$

where ΔA is amplitude deviation [dB]. The output carriers at Point C have a phase difference of about 60 degrees so the insertion loss of the comb filter is about 1.7 dB, assuming that the transmission losses of the optical divider, optical coupler, and optical fibers are negligible.

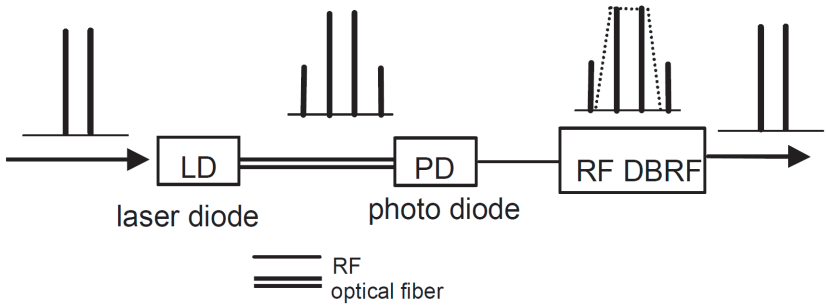

Figure 5.2: Circuit configuration of the RoF link with RF-DBRF.

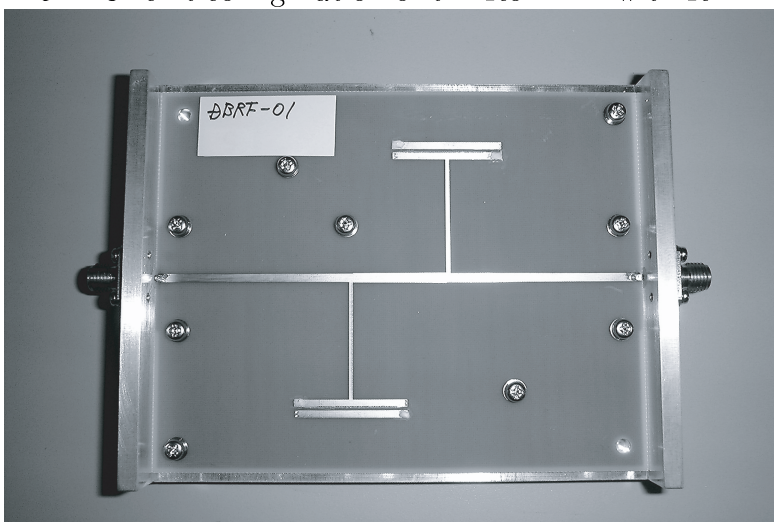

Figure 5.3: Fabricated RF-DBRF.

5.2.2 RoF Link with RF Comb Filter

Figure 5.1(b) shows the circuit configurations of the proposed RoF link with RF comb filter. In this arrangement, the comb filter is composed of an RF divider, RF coupler, and two RF transmission lines. The RF comb filter is placed after the PD. The distortion cancellation mechanism of the RF comb filter is basically the same as that of the optical comb filter, so equations (5.1)–(5.12) are also applicable.

According to (5.1), longer L_L is needed when Δf becomes narrow, and this would cause high insertion loss in the long path in the RF comb filter. When the attenuation difference between long and short paths is A[dB], an attenuator with A[dB] must be inserted in the short path, as shown in Fig.5.1(b). In this case, the insertion loss of the RF comb filter is calculated as follows.

$$InsertionLoss = 1.7 + A[dB]. \tag{5.13}$$

This insertion loss can be reduced by using a 1:n coupler/divider with $n =$

$10(A/20)$ instead of inserting an attenuator. When the tuning of 1:n is perfect and no attenuator is used in the short path, the insertion loss of the RF comb filter is calculated as follows

$$InsertionLoss = 1.7 + 0.5A[dB]. \tag{5.14}$$

The insertion loss caused by the 1:n coupler/divider in (5.14) is reduced to half that of (5.13). In this paper, we selected to employ the additional attenuator, so (5.13) was used.

5.2.3 RoF Link with RF-DBRF

In the field of microwave RF circuits, the use of RF-DBRF has been proposed for distortion reduction [5.16]. Figure 5.2 shows an RoF link with a RF-DBRF. The RF-DBRF is set after the PD in order to reduce the distortion caused by the LD, like the RF comb filter. In our case, the RF-DBRF is formed on a substrate with ϵ_r = 3.45, thickness = 0.8 mm. Two short-circuited quarter-wavelength stubs are closely placed with their open ends face to face. They couple to each other through the electrical field at their open ends, resulting in its equivalence to two coupled resonant circuits. As a result, the RF-DBRF exhibits steep slope characteristics. A fabricated RF-DBRF is shown in Fig.5.3.

5.3 Experimental Results

5.3.1 RoF Link with Optical Comb Filter

We made an RoF link prototype that employed an optical comb filter with normal single mode fibers for Δf = 5 MHz in the 2 GHz band. In this case, the optical fiber's physical length of the long path $\approx$ 11 [m]. A distributed feedback (DFB) LD with bias current = 20 mA was used.

Figure 5.4 shows measured carrier and IM3 components of the RoF link prototype. As the insertion loss caused by the optical comb filter is around 10dB, the measured result without the filter is shifted along the output axis, in order to match the carrier plot. We found that the polarization controller (PC), shown in Fig.5.1(a), is needed in one path. This is because the relative-intensity-noise (RIN) of the optical comb filter increases if the polarization plane is not adjusted [5.15]. The measured result without PC is also plotted in Fig.5.4. Figure 5.5 shows the measured output spectra when the RIN is changed by PC adjustment. It is observed that the RIN varies by more than 20 dB and the carriers and IM3 components are not changed, when the polarization state is changed. Thus we assume that the plot without PC in Fig.5.4 is correct when the RIN level is near maximum as shown in Fig.5.5(a). Without PC, $\Delta A \approx 0$ dB as the transmission loss of optical fibers are negligible. On the other hand, ΔA caused by the PC insertion is around 1 dB. Thus the measured IM3

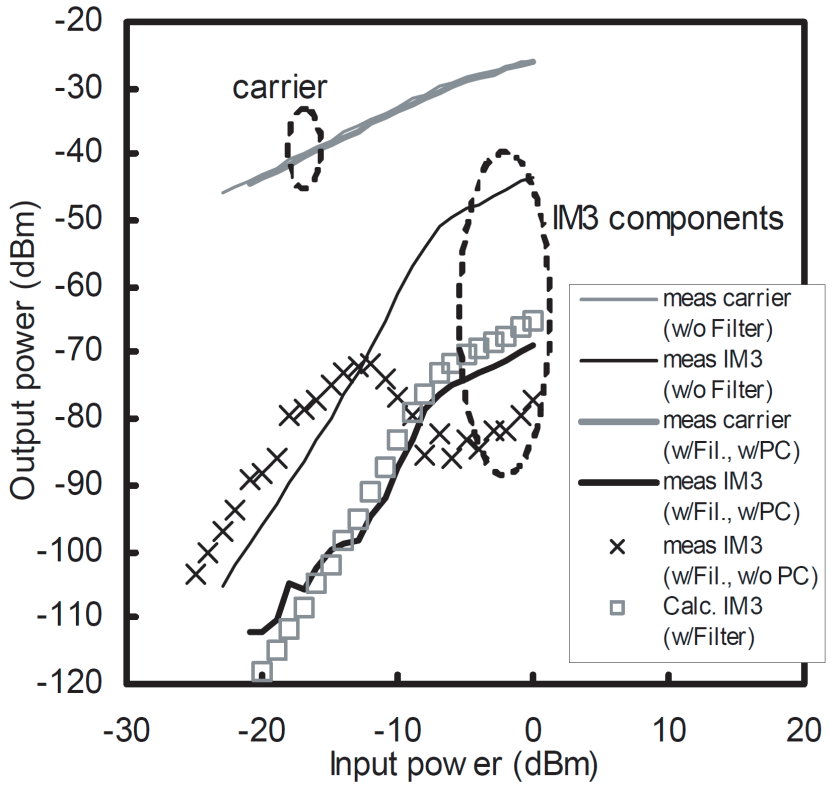

Figure 5.4: Measured carrier and IM3 component of RoF link employing optical comb filter (Δf = 5 MHz).

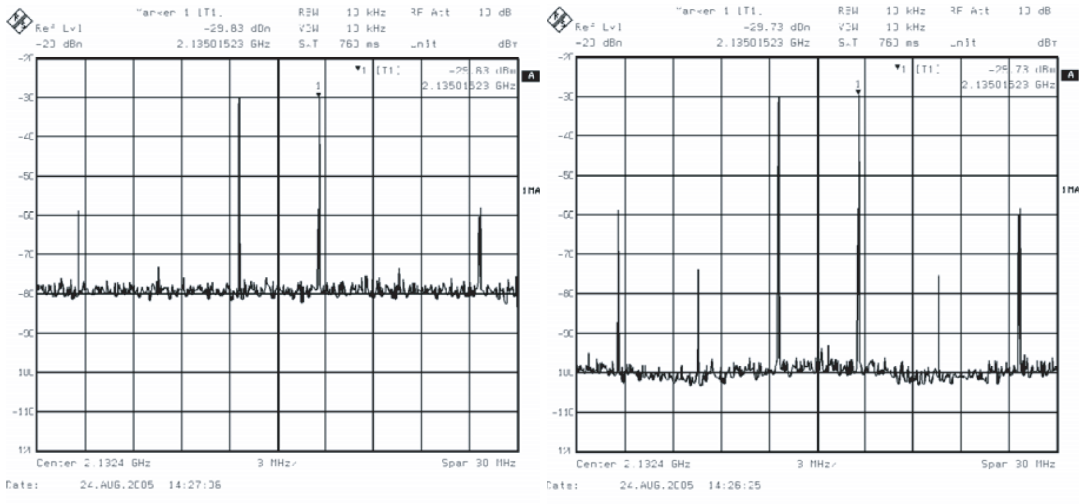

Figure 5.5: Measured output spectra of RoF link employing optical comb filter when RIN is (a) maximum and (b) minimum (Δf = 5 MHz).

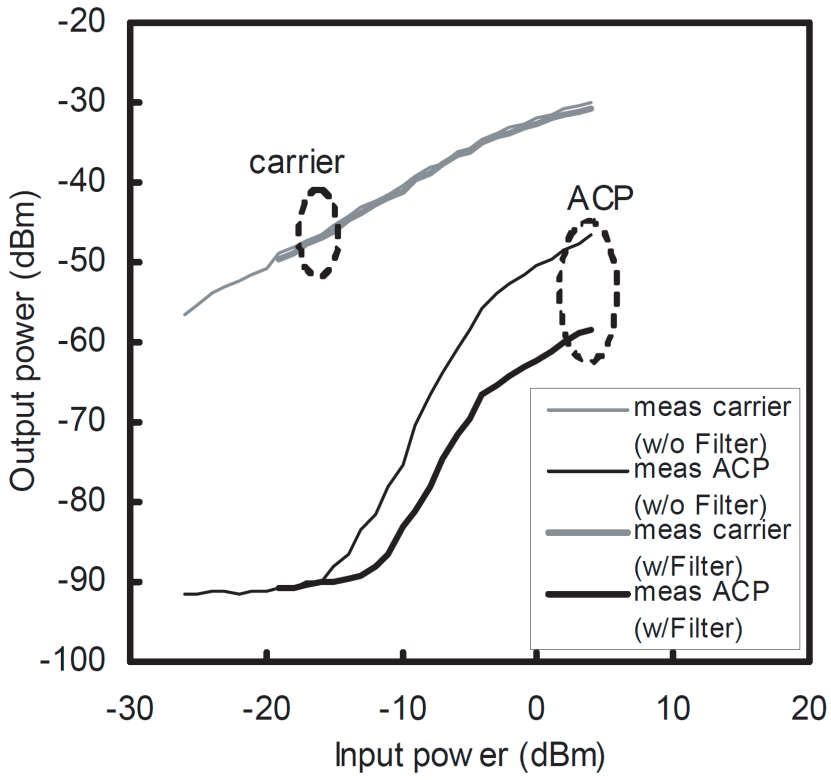

Figure 5.6: Measured carrier and ACP of RoF link employing the optical comb filter (W-CDMA modulated, $\Delta f = 5$ MHz).

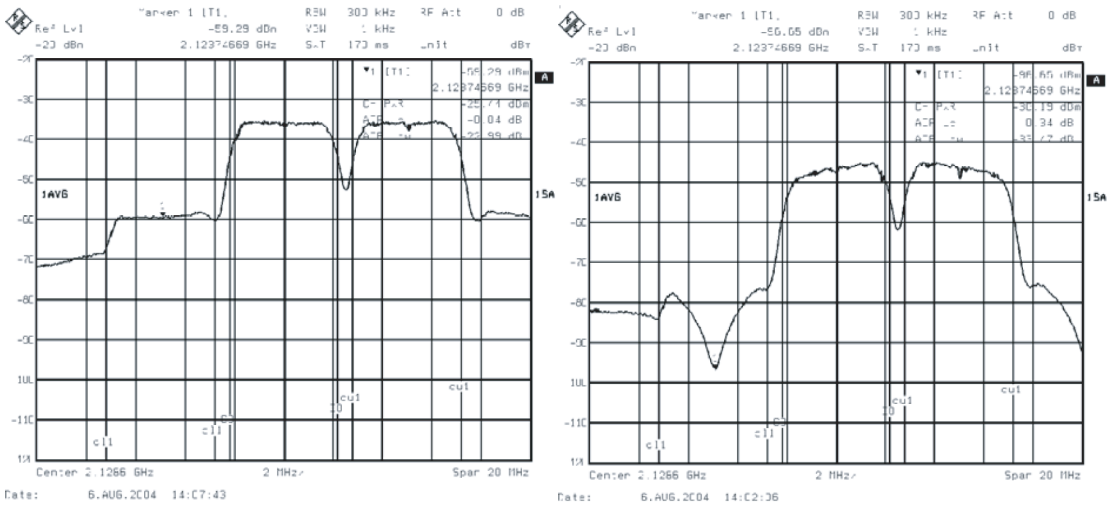

Figure 5.7: Measured output spectra of RoF link, (a) without the comb filter and (b) with the comb filter (W-CDMA modulated, $\Delta f = 5$ MHz).

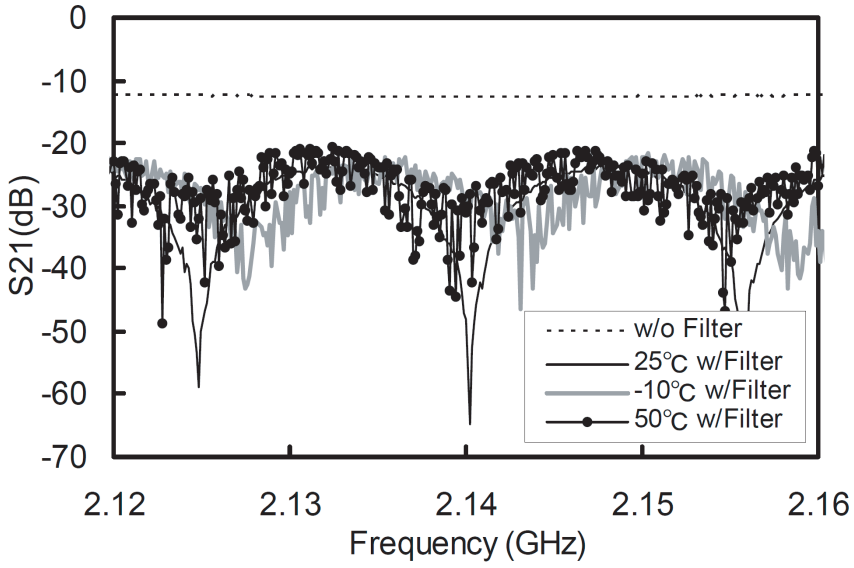

(a)

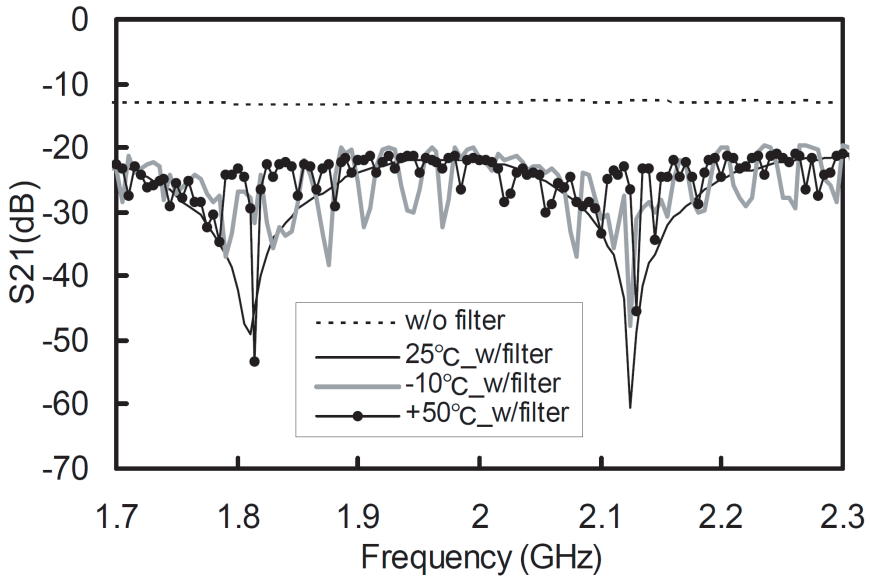

(b)

Figure 5.8: Measured S21 of RoF link employing optical comb filter for (a) $\Delta f = 5$ MHz and (b) $\Delta f = 100$ MHz with temperature variation.

components without PC, shown in Fig.5.4, are lower than those with PC when the input power exceeds -10 dBm (in this region, output power of IM3 components is stronger than the RIN level). As a result, both the upper and lower frequency IM3 components are improved by around 20 dB compared to the values without the filter. The calculated IM3 component with the filter plotted in Fig.5.4 was calculated using (5.12). The measured values with PC and calculated results agree with each other.

Figure 5.6 shows the measured carrier and adjacent channel power (ACP) of the RoF link prototype in the case of W-CDMA modulated two tone carriers (3.84 MHz bandwidth) instead of continuous waves. The improvement in ACP is reduced to around 12 dB in this case. This is because the 3.84 MHz bandwidth is not negligible compared to Δf. Figure 5.7 shows the output spectra of the RoF link prototype for the input power of -5dBm. Figure 5.7(b) shows that the rejection bandwidth is much narrower than 3.84 MHz. As shown in Fig.5.6, the noise level with the filter is of the same level as that without the filter, despite the 10 dB plot shift along the output axis. This is because the PC adjustment minimized the noise level as shown in Fig.5.5(b). Therefore, it can be said that the optical comb filter can reduce the noise level (10 dB in Fig.5.6) as well as distortion.

Figure 5.8 shows measured S_{21} of the RoF link with the optical comb filter. Ports 1 and 2 are defined in Fig.5.1(a), and temperature was changed from -10 ℃to +50 ℃. At 25 ℃, the measurement was done without employing a temperature chamber. At -10 ℃and +50 ℃, the S_{21} plot is not smooth. This is because of vibration caused by wind in the temperature chamber. As shown in Fig.5.8, rejection frequency varies around 5MHz in this temperature range for both $\Delta f = 5$ MHz and $\Delta f = 100$ MHz. This is quite large in the $\Delta f = 5$ MHz case, but negligible in the $\Delta f = 100$ MHz case.

5.3.2 RoF Link with RF Comb Filter

An RoF link prototype with RF comb filter for $\Delta f = 5$ MHz and 100 MHz in the 2 GHz band was also evaluated. In this case, the RF coaxial cable's physical length of the long path ≈ 14 [m] and 1 [m], respectively. Figure 5.9 shows measured S_{21} of the ROF link with RF comb filter. Ports 1 and 2 are defined in Fig.5.1(b), and temperature was changed from -10 ℃to +50 ℃. The rejection frequency varies around 5 MHz in this temperature range, for both $\Delta f = 5$ MHz and 100 MHz. This is quite large in the $\Delta f = 5$ MHz case shown in Fig.5.9(a), but negligible in the $\Delta f = 100$ MHz case shown in Fig.5.9(b). Attenuator A was set to 8 dB and 0 dB for $\Delta f = 5$ MHz and 100 MHz, respectively, so insertion loss levels of the RF comb filters were around 10 dB and 2 dB for $\Delta f = 5$ MHz and 100 MHz, respectively. The insertion loss level for $\Delta f = 5$ MHz can be improved by 4 dB by applying (5.14). S_{21} plots of the RF comb filters are stable against vibration, unlike the optical comb filter.

Figure 5.10 shows the measured carrier and adjacent channel power (ACP) of the ROF link prototype with RF comb filter for $\Delta f = 5$ MHz with W-CDMA modulated two tone carriers. The improvement in ACP is around 12 dB. As shown in Fig.5.9(a),

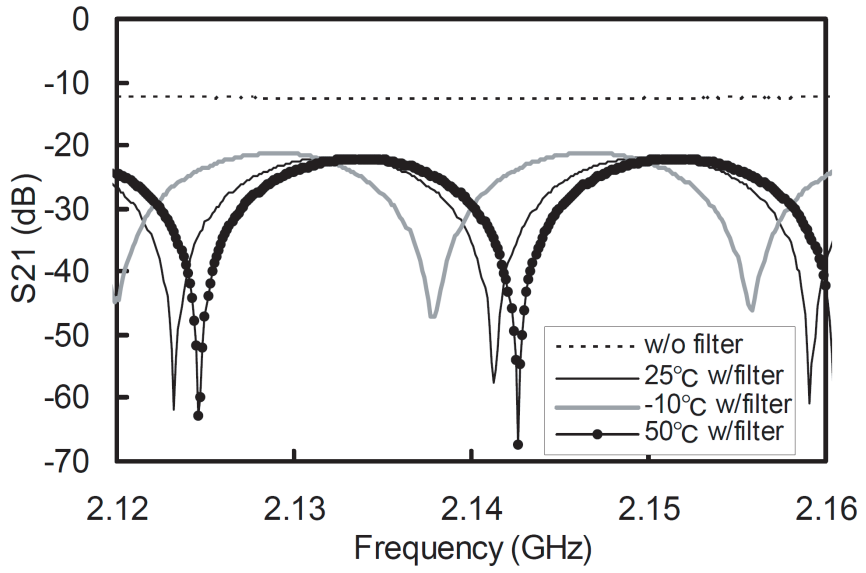

(a)

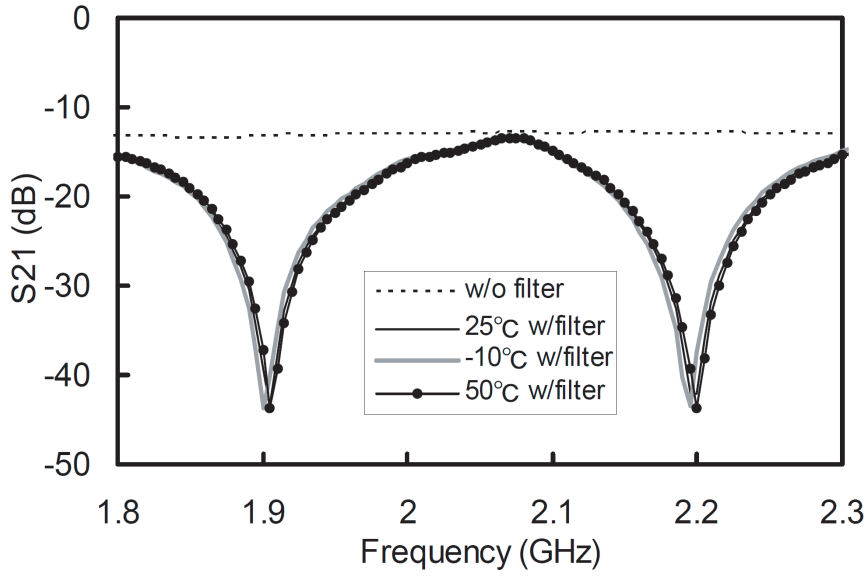

(b)

Figure 5.9: Measured S21 of RoF link employing RF comb filter for (a) $\Delta f = 5$ MHz and (b) $\Delta f = 100$ MHz with temperature variation.

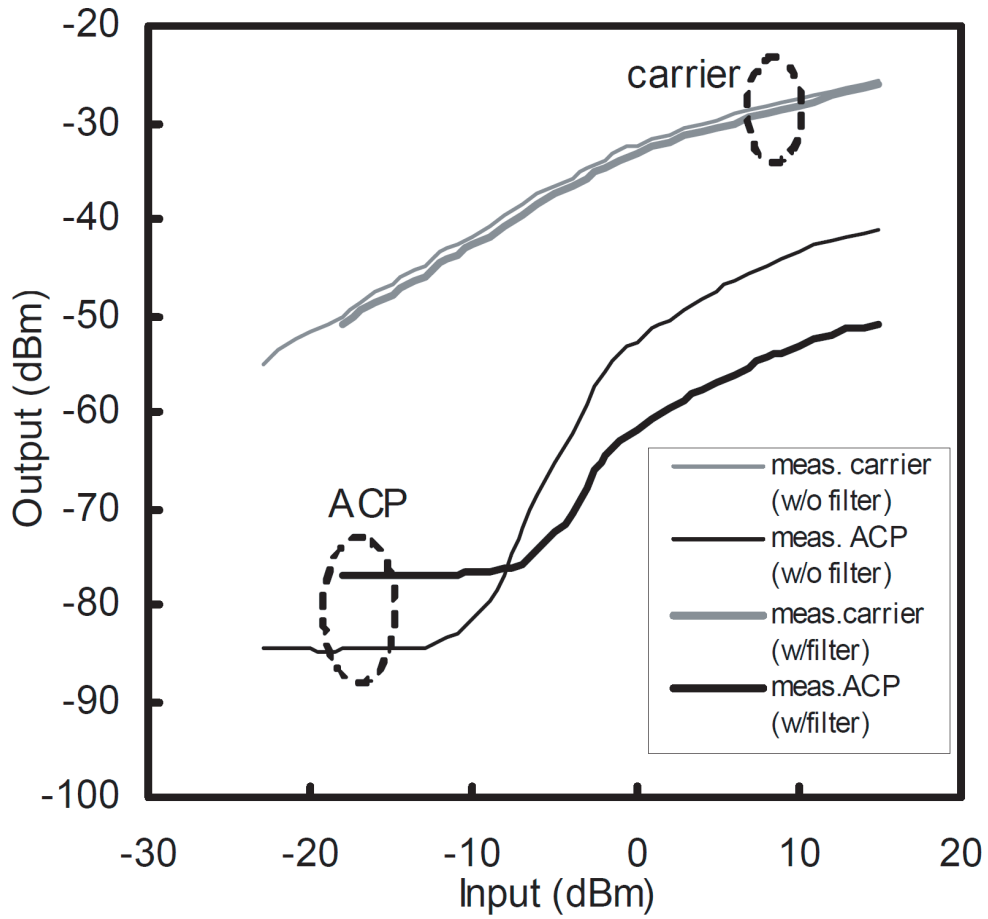

Figure 5.10: Measured carrier and ACP of RoF link employing the RF comb filter (Δf = 5 MHz, W-CDMA modulated).

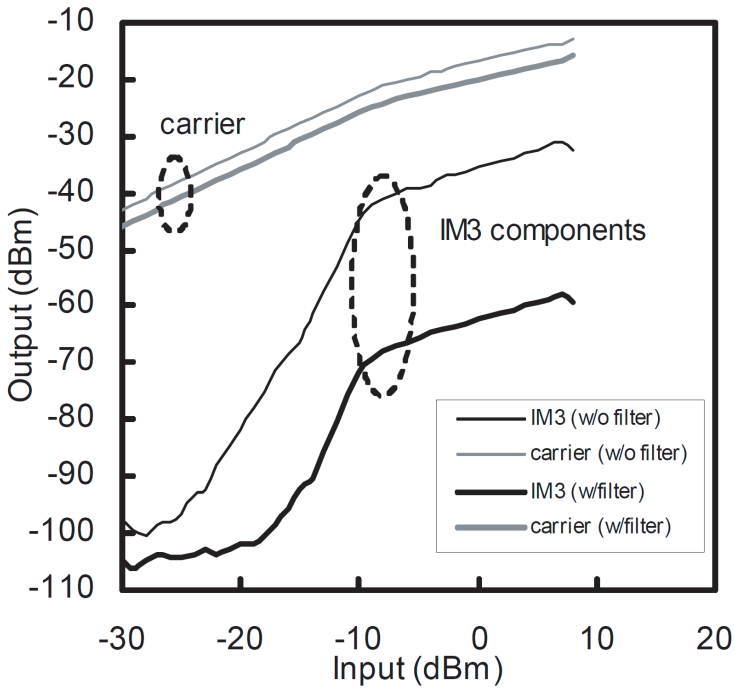

Figure 5.11: Measured carrier and IM3 component of RoF link employing RF comb filter (Δf = 100 MHz, RBW = 30 kHz).

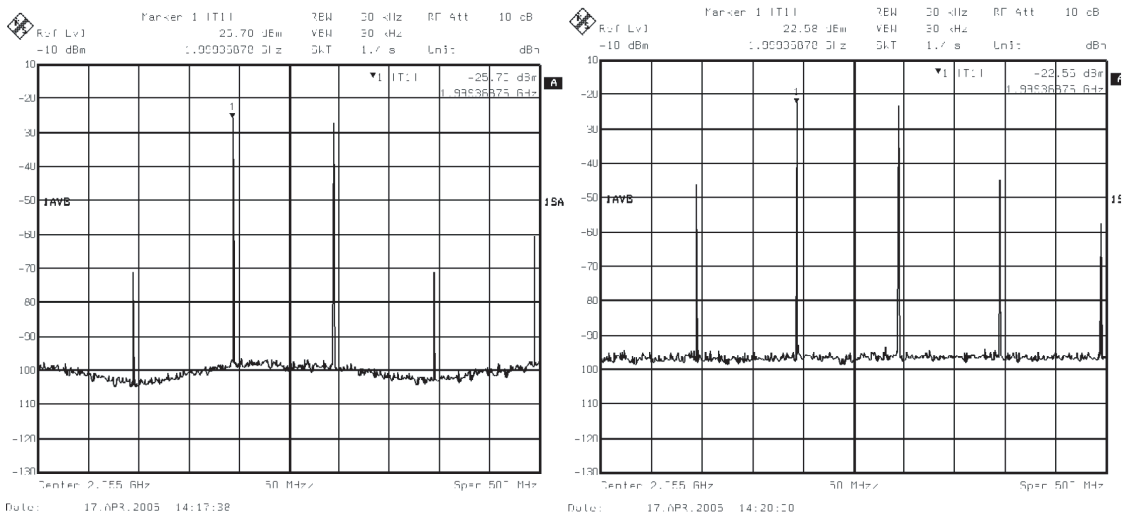

(a) (b)

Figure 5.12: Measured output spectra of RoF link, (a) with the RF comb filter and (b) without the RF comb filter (Δf = 100 MHz).

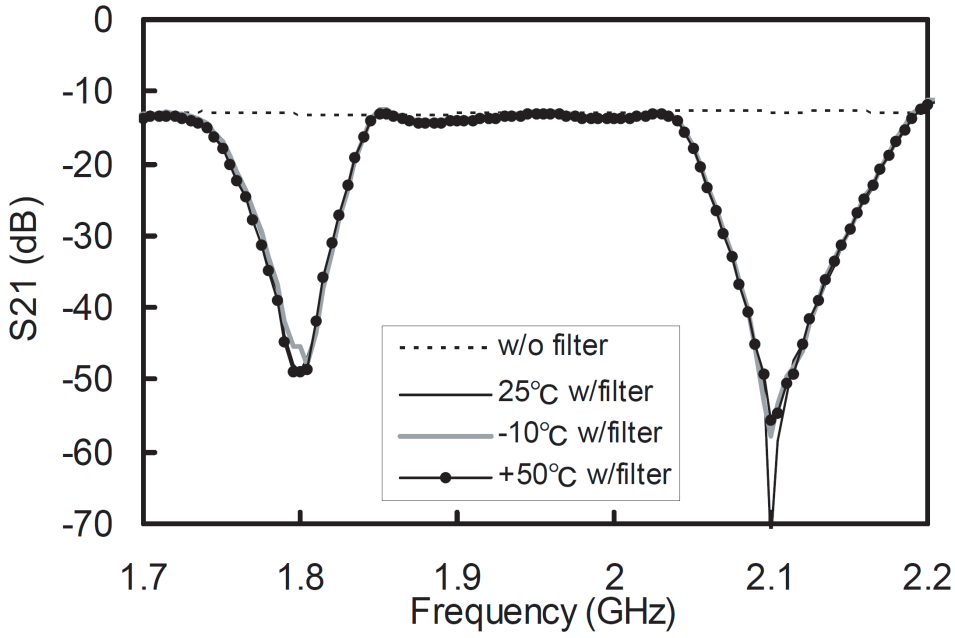

Figure 5.13: Measured S21 of RoF link employing RF-DBRF for $\Delta f = 100$ MHz with temperature variation.

the insertion loss is 10 dB so the plot without the filter was shifted along the output axis by 10 dB, as in Fig.5.6. As a result, in consideration of the 10 dB shift, the filter reduces the noise level by around 3 dB. The output spectrum in this case is similar to Fig.5.7(b).

Figure 5.11 shows the measured carrier and IM3 component of the RoF link prototype with RF comb filter for $\Delta f = 100$ MHz. The improvement in IM3 component is over 20 dB. As shown in Fig.5.9(b), insertion loss level is only 2 dB so the plot without the filter is not shifted along output axis in this figure, unlike Figures 5.4, 5.6, and 5.10. In this measurement, resolution bandwidth (RBW) of the spectrum analyzer was fixed to 30 kHz even at the small output level, unlike Fig.5.4. Fig. 5.11 shows that the filter improves the noise level by more than 3 dB. So it can be said that the RF comb filter can slightly reduce the noise level, but its reduction effect is not as strong as that observed in Fig.5.6. The measured output spectra with and without the filter are shown in Fig.5.12. As shown in Fig.5.12(a), the noise level at rejection frequencies of the RF comb filter (1.9 and 2.2 GHz) is reduced by more than 3 dB.

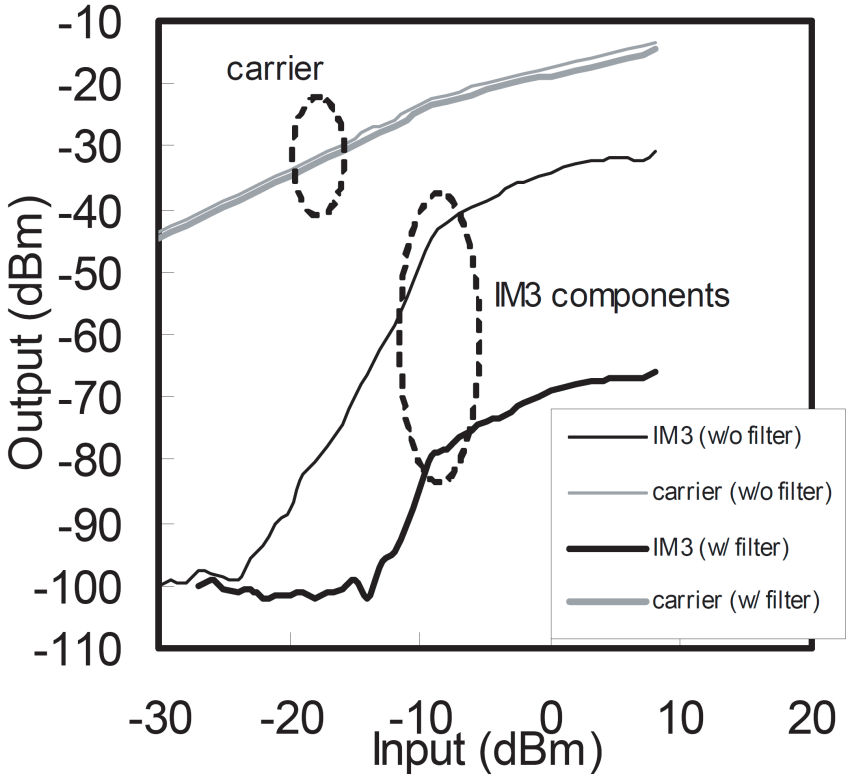

Figure 5.14: Measured carrier and IM3 component of RoF link employing RF-DBRF (Δf = 100 MHz, RBW = 30 kHz).

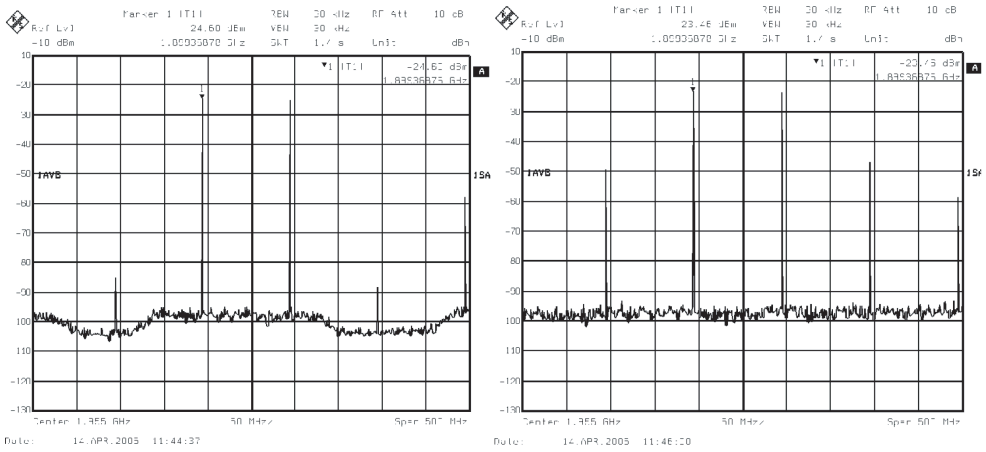

(a) (b)

Figure 5.15: Measured output spectra of RoF link, (a) with the RF-DBRF and (b) without the RF-DBRF (Δf = 100 MHz).

Table 5.1: Summary of RoF link with three filters.

	IM3 improv.	ACP improv. (Δf=5MHz)	Ins.loss (Δf=5/100MHz)	Noise reduct.	Remarks
Opt.comb	$\geq$ 20dB	12dB	10dB	10dB	poor stability
RF comb	$\geq$ 20dB	12dB	10/2dB	$\geq$ 3dB	
RF-DBRF	$\geq$ 30dB	N.A.	N.A./1dB	$\geq$ 3dB	flat pass band

5.3.3 RoF Link with RF-DBRF

An RoF link prototype employing an RF-DBRF for Δf = 100 MHz at 2 GHz band was also evaluated. Figure 5.13 shows measured S_{21} of the RoF link with RF comb filter, when the temperature was changed from -10 ℃to +50 ℃. Rejection frequency deviation is within 5 MHz in this temperature range. Furthermore, comparing Fig.5.13 with Figs.5.8 and 5.9, RF-DBRF is shown to have a steep rejection shape and flat pass band properties from 1.85 to 2.05 GHz. This characteristic has an advantage in that the carriers are not affected by the filter. The insertion loss level is within 1 dB. This prototype employed a planar circuit filter with Δf = 100 MHz, however, Δf can be reduced by employing the waveguide construction [5.16]. The RF-DBRF is expected to reduce wideband distortion if an RF high pass filter (HPF) and a low pass filter (LPF) are added.

Figure 5.14 shows the measured carrier and IM3 component of the RoF link prototype with RF-DBRF. The improvement in IM3 component is over 30dB. As shown in Fig.5.13, insertion loss level is under 1 dB so the plot without the filter is not shifted along the output axis and RBW is fixed to 30 kHz, as in Fig.5.11. Figure 5.14 shows that the addition of the filter improves the noise level by more than 3 dB. The measured output spectra with and without the filter are shown in Fig.5.15. As shown in Fig. 5.15(a), noise level is reduced at the rejection frequencies of the RF-DBRF (1.8 and 2.1 GHz).

5.4 Conclusion

Three distortion reduction filters for radio-on-fiber systems are proposed and evaluated in the 2 GHz band. These filters have simple construction as they are composed of all passive components, and can reduce IM3 (spurious) components even in the saturation region, unlike conventional linearizers. The optical comb filter can reduce IM3 components by more than 20 dB and the noise level by around 10 dB, but insertion loss is large and stability against vibration is very poor. The proposed RF comb filter can reduce IM3 components by more than 20 dB and reduce noise by more than 3 dB; its insertion losses are 2 and 10 dB for frequency separations of Δf = 100 MHz and 5 MHz, respectively. A RF-DBRF for Δf = 100 MHz can reduce IM3

components by more than 30 dB and noise level by more than 3 dB. These results are summarized in Table 5.1. It can be said that RF-DBRF has the best properties for Δf = 100 MHz. Frequency deviations in the temperature range of -10 ℃to +50 ℃are within 5 MHz for all filters. The RF comb filter and the RF-DBRF are stable against vibration, so these filters will be powerful solutions for the introduction of radio-on-fiber to wideband communication systems.

5.5 References

[5.1] W.I.Way, "Optical fiber-based microcellular systems: an overview," IEICE Trans. Commun., vol.E76-B, no.9, pp. 1091-1102, September 1993.

[5.2] T.Kuri and K.Kitayama, "Optical heterodyne detection of millimeter-wave-band radio-on-fiber signals with a remote dual-mode local light source," IEEE Trans. Microwave Theory & Tech., vol.49, no.10, pp. 2025-2029, October 2001.

[5.3] H.Al-Raweshidy and S.Komaki, "Raio over fiber technologies for mobile communications networks," Artech House, 2002.

[5.4] T.Nagatsuma, "Recent progress in microwave photonics technologies," IEICE Trans. Electron. (Japanese Edition), vol.J87-C, no.4, pp. 357-368, April 2004.

[5.5] L.S.Fock, A.Kwan and R.S.Tucker, "Reduction of semiconductor laser intensity noise by feedforward compensation: experiment and theory," IEEE J. Lightwave Technol., vol.10, no.12, pp. 1919-1925, December 1992.

[5.6] D.Hassin and R.Vahldieck, "Feedforward linearization of analog modulated laser diodes - theoretical analysis and experimental verification," IEEE Trans. Microwave Theory & Tech., vol.41, no.12, pp. 2376-2382, December 1993.

[5.7] L.Roselli, V.Borgioni, F.Zepparelli, F.Ambrosi, M.Comez, P.Faccin and A.Casini, "Analog laser predistortion for multiservice radio-over-fiber systems," IEEE J. Lightwave Technol., vol.21, no.5, pp. 1211-1223, May 2003.

[5.8] R.A.Adb-Alhameed, P.S.Excell, J.G.Gardiner and N.T.Ari, "Volterra series analysis of a laser diode predistorter for mobile communication systems," Microwave J., vol.47, no.9, pp. 190-197, September 2004.

[5.9] P.B.Kenington, "High-Linearity RF Amplifier Design,"Artech House, 2000.

[5.10] N.Pothecary, "Feedforward Linear Power Amplifiers," Artech House, 1999.

[5.11] S.Tanaka, N.Taguchi, T.Kimura and Y.Atsumi, "A predistortion type equi-path linearizer designed for radio-on-fiber system," IEEE Trans. Microwave Theory & Tech., vol.54, no.2, pp.938-944, February 2006.

[5.12] R.Kohno, "Collaboration among industry, academia and government for R&D of ultra wideband wireless technologies and contribution in standardization in wireless PAN," IEICE Trans. Fundamentals (Japanese Edition), vol.J86-A, no.12, pp. 1274-1283, December 2003.

[5.13] S.Tanaka, N.Taguchi, T.Kimura and Y.Atsumi, "Distortion canceller for radio-on-fiber link employing comb filter," 1st Asia-Pacific Microwave Photonics Conference, L-5, pp.366-369, April 2006.

[5.14] X.Shu, S.Jiang and D.Huang, "Fiber grating Sagnac loop and its multiwavelength-laser application," IEEE Photon. Technol. Lett., vol.12, no.8, pp. 980-982, August 2000.

[5.15] N.Taguchi, S.Tanaka, T.Kimura and Y.Atsumi, "Relative-intensity-noise reduction technique for frequency-converted radio-on-fiber system," IEEE Trans. Microwave Theory & Tech., vol.54, no.2, pp.945-950, February 2006.

[5.16] H.Uchida, H.Kamino, K.Totani, N.Yoneda, M.Miyazaki, Y.Konishi, S.Makino, J.Hirokawa, and M.Ando, "Dual-band-rejection filter for distortion reduction in RF transmitters,"IEEE Trans. Microwave Theory & Tech., vol.52, no.11, pp.2550-2556, November 2004.

Chapter 6

Wideband Balun for Radio-on-Fiber (RoF) System with Dual-Drive Mach-Zehnder Modulator

Existing radio-on-fiber (RoF) systems offer only an unbalanced (single-ended) radio frequency (RF) interface. In order to realize a balanced RF interface at the input, we propose to use a dual-drive Mach-Zender modulator as a wideband balan. The performance of this configuration is evaluated. An experiment using mixed-mode S parameters shows that the proposed arrangement offers common mode rejection ratio (CMRR) of at least 15 dB and insertion loss of 41±2 dB from 20 MHz to 6 GHz (bandwidth ≈ 199 %). Furthermore, the addition of an erbium-doped fiber amplifier (EDFA) improves the performance (CMRR over 30 dB and insertion loss of 8±2 dB). It is also validated that the proposed arrangement can be used as balun upto 18 GHz, from the comparison between CMRR and inbalances measured by the conventional network analyzer. Additionally, the received light power at the two types of photo diode is optimized from the standpoint of insertion loss, CMRR, and return loss. It is found that the optimum received light power depends on the type of photo diode.

6.1 Introduction

Radio-on-fiber (RoF) systems are widely used for wireless communication networks. RoF systems have RF input (E/O; electric to optical conversion) and output (O/E) ports, and most ports are unbalanced (single-ended) [6.1]–[6.5]. However, in the RF circuit field, balanced ports are often used for microwave communication systems, e.g., mobile phone terminals [6.6]. Even systems in the millimeter wave region have started to apply balanced ports [6.7]. In another important trend, RoF systems are also being used in precise electric field measurement systems as it can reduce measurement distortion and realize long distance transmission [6.8]. Many of the antennas used have balanced ports (e.g. dipole antenna [6.9]). These facts confirm

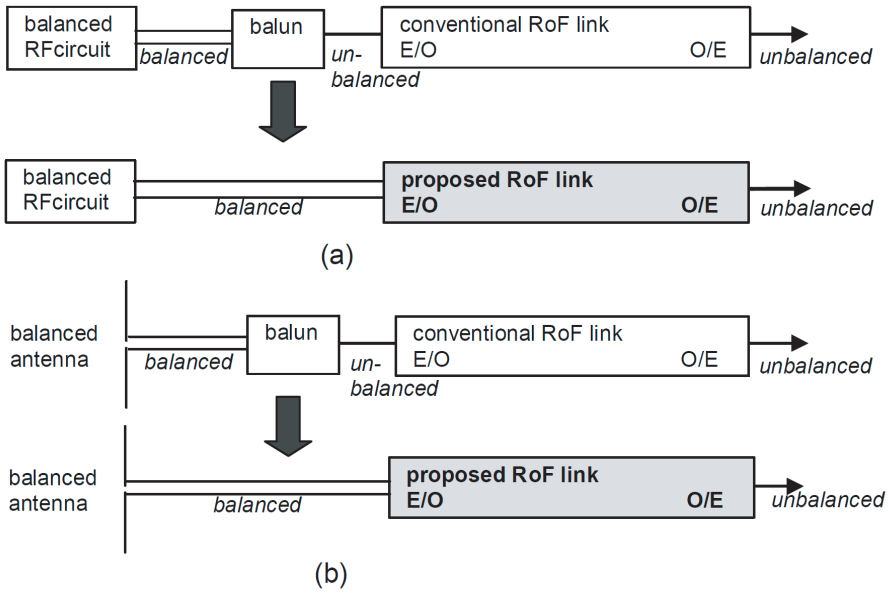

Figure 6.1: Applying proposed RoF link to support (a) balanced RF circuit and (b) balanced antenna system.

that baluns are needed between balanced RF devices and RoF systems, but there are difficulties to implement a wideband balun [6.10].

This Chapter proposes an RoF link that uses two input ports of dual-drive Mach-Zender modulator (DD-MZM) [6.11] to realize wideband balun properties. The link has a balanced input RF port and an unbalanced output RF port. Our target is to obtain a common mode rejection ratio (CMRR) of at least 15dB. As it can be expected that the DD-MZM has wideband property, the proposed link is evaluated as wideband balun. Two applications of this RoF link are shown in Fig.6.1. Figure 6.1(a) shows it supporting a balanced RF circuit; Fig.6.1(b) shows it supporting an balanced antenna system. In both cases, the balun is not needed with proposed RoF link.

First, in this Chapter, the circuit configuration of the proposed RoF link is shown in Section 6.2. Then, the experimental results of the balun, mixed-mode S parameters upto 6 GHz together with inbalances upto 18 GHz are shown and discussed in Section 6.3. Additionally, in Section 6.4, optimised received light power at the photodiode (PD) from the standpoint of insertion loss, CMRR, and return loss is shown. In Sections 6.3 and 6.4, RoF link employing uni-traveling-carrier photodiode (UTC-PD) [6.13] and positive-intrinsic-negative photodiode (PIN-PD) are measured and compared.

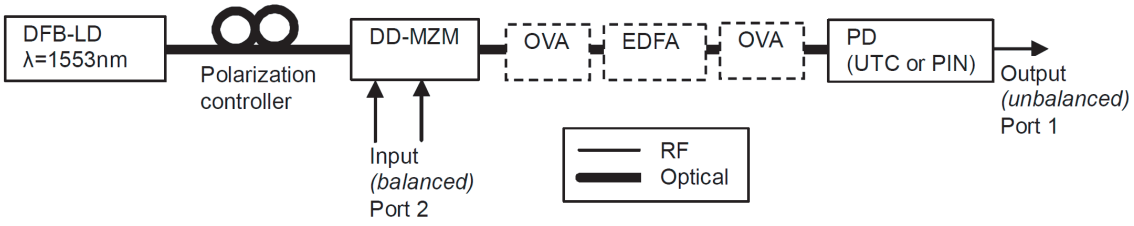

Figure 6.2: Circuit configuration of the proposed RoF link with wideband balun functionality.

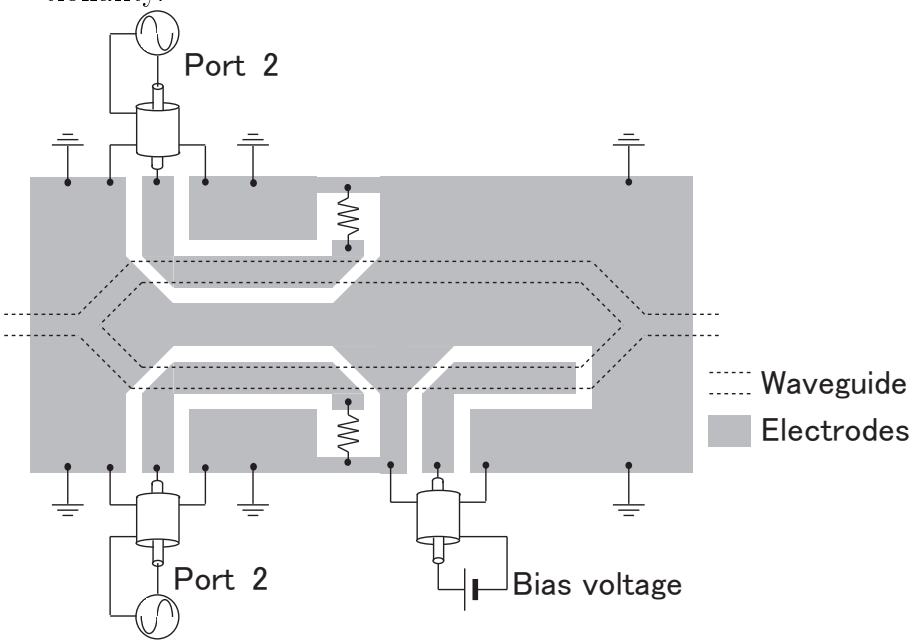

Figure 6.3: Configuration of dual-drive Mach-Zender modulator.

6.2 Circuit Configuration

Figure 6.2 shows the circuit configuration of the proposed RoF link. The light with wavelength λ = 1553 nm is emitted from a distributed feedback laser diode (DFB-LD) with RIN $\approx$ -163 dB/Hz at 2 GHz. The light is injected to a commercial DD-MZM after its polarization is set in a polarization controller so as to maximize the extinction ratio. At the DD-MZM, balanced RF signals modulate the light. After transmission through the transmission optical fiber (single-mode), the light is detected by a PD. Two types of PD, UTC-PD that with wideband property and PIN-PD with narrow band property were employed. The erbium doped fiber amplifier (EDFA) accompanied with optical variable attenuators (OVAs) shown in Fig.6.2 is optional. The effect of the EDFA is described in detail in the following sections.

The configuration of employed DD-MZM is shown in Fig.6.3. It is commercially available z-cut modulator with V_π = 5.1 V, optical insertion loss = 4.6 dB, extinction ratio = 45 dB. The ground of a pair of ports used as port 2 (balanced) and bias port are electrically connected to the ground of DD-MZM, as shown in Fig.6.3. The z-cut modulator has property that the convergence of electrical flux line varies signal phase very much, but chirp is degraded as the signal phase change is not same in hot and ground electrodes. In case of DD-MZM, two signals with same amplitude and oposite phase are injected into two electrodes, in order to obtain zero-chirp [6.11]. So we can expect that DD-MZM can be wideband balun, when two electrodes are used as balanced port.

In normal balun, one port of balanced port is connected to ground of unbalanced port [6.9]. However, the port with connection to ground cannot modulate light, so the balanced port is not connected to ground in this case. In the configuration shown in Fig.6.3, The ground of DD-MZM and that of PD is not connected electrically. This is because if those grounds are connected, electric line between DD-MZM and PD is needed so long distance transmission with low loss and low distortion measurement of electric field cannot be done. With this configuration, the degradation of transmission performance will be worried when the operation frequency reaches DC. But it is verified by the experiments that the transmission performance never degraded when operating frequency is higher than 30 kHz.

6.3 Experimental Results

The circuit shown in Fig.6.2 is elavuated experimentally as a wideband balun. We used a four-port network analyzer in order to measure the mixed-mode S parameters [6.12]. The measured S parameters with three single-ended ports (one for port 1 and two for port 2, see Fig.6.2) were converted into mixed-mode S parameters. S_{SD12} refers to the transmission characteristics from port 2 (differential mode) to single-ended port 1, so a large value (i.e., small insertion loss) is desired. S_{SC12} refers to the transmission characteristics from port 2 (common mode; it is undesired) to

single-ended port 1, so a small value is desired. CMRR is calculated as follows

$$CMRR = S_{SD12} - S_{SC12}[dB]. \tag{6.1}$$

Our target is CMRR $\geq$ 15 dB in this case. This target value is deternmined from the measured result of rat-race balun [6.14] and commercially available wideband ferrite balun [6.15]. As for the reflection characteristics, S_{DD22} at port 2 and S_{SS11} at port 1 are mainly determined by balun performance. The target value of these reflection S parameters are return loss $\geq$ 14 dB. This value is also deternmined from measured result, same as CMRR. As the single-ended impedances of three ports are all 50 ohms in our case, the impedances of balanced port 2 is 100 ohms. This value can be changed by designing of DD-MZM.

In this Chapter, the RoF link is mainly evaluated by the mixed-mode S parameters. However, RoF link employing UTC-PD, which has wideband property, is evaluated by mixed-mode S parameters and imbalances. In the case of imbalance measurement, the port 2 (balanced) shown in Fig.6.2 is used as port 2 and 3, and single-ended 3 port measurement was done. In Fig.6.2, input port is port 2 and output port is port 1. This port numbers setting is selected in order to maintain port number 1 in both measurement methods. Mixed-mode S parameters were measured upto 6 GHz (due to limitation of four-port network analyzer). Imbalances were measured upto 18 GHz.

6.3.1 RoF Link employing UTC-PD

Figure 6.4 shows the measured mixed-mode S parameters of the proposed RoF link employing UTC-PD without an EDFA. S_{SD12} is almost constant (from -39 dB to -43 dB) from 20 MHz to 6 GHz so the insertion loss of the proposed link is 41$\pm$2 dB. This is not small, but RF amplifiers after UTC-PD can recover this insertion loss. CMRR more than 15 dB is obtained from Fig.6.4(a), so our target is achieved by the configuration without an EDFA. Reflection characteristics are shown in Fig. 6.4(b). Return losses are more than 20 dB in both ports 1 and 2.

As mentioned above, the target CMRR is cleared without EDFA. However, Fig.6.4(a) shows that S_{SC12} contains noises very much. It is estimated that the noises are mainly caused by PD (shot noise or thermal noise), as the received light power at UTC-PD is around -2 dBm. So we can expect that S_{SC12} can be suppressed relative to S_{SD12} (i.e. CMRR is increased) by enlarging the light power. Therefore, EDFA shown in Fig.6.2 is added. The OVAs in front and behind of EDFA is employed for the protection of EDFA, and their attenuation levels were set to 0 dB at the time of measurement (the insertion loss of the OVA is around 2 dB when the attenuation level is set to 0 dB). The noise figure of the EDFA is 7.5 dB. Figure 6.5 shows the mixed-mode S parameters of the proposed RoF link with UTC-PD when EDFA is employed. The received light power at PD is adjusted to +19 dBm, and the reason for this value is investigated in detail in Section 6.4. Figure 6.5(a) shows that the S_{SD12} is improved

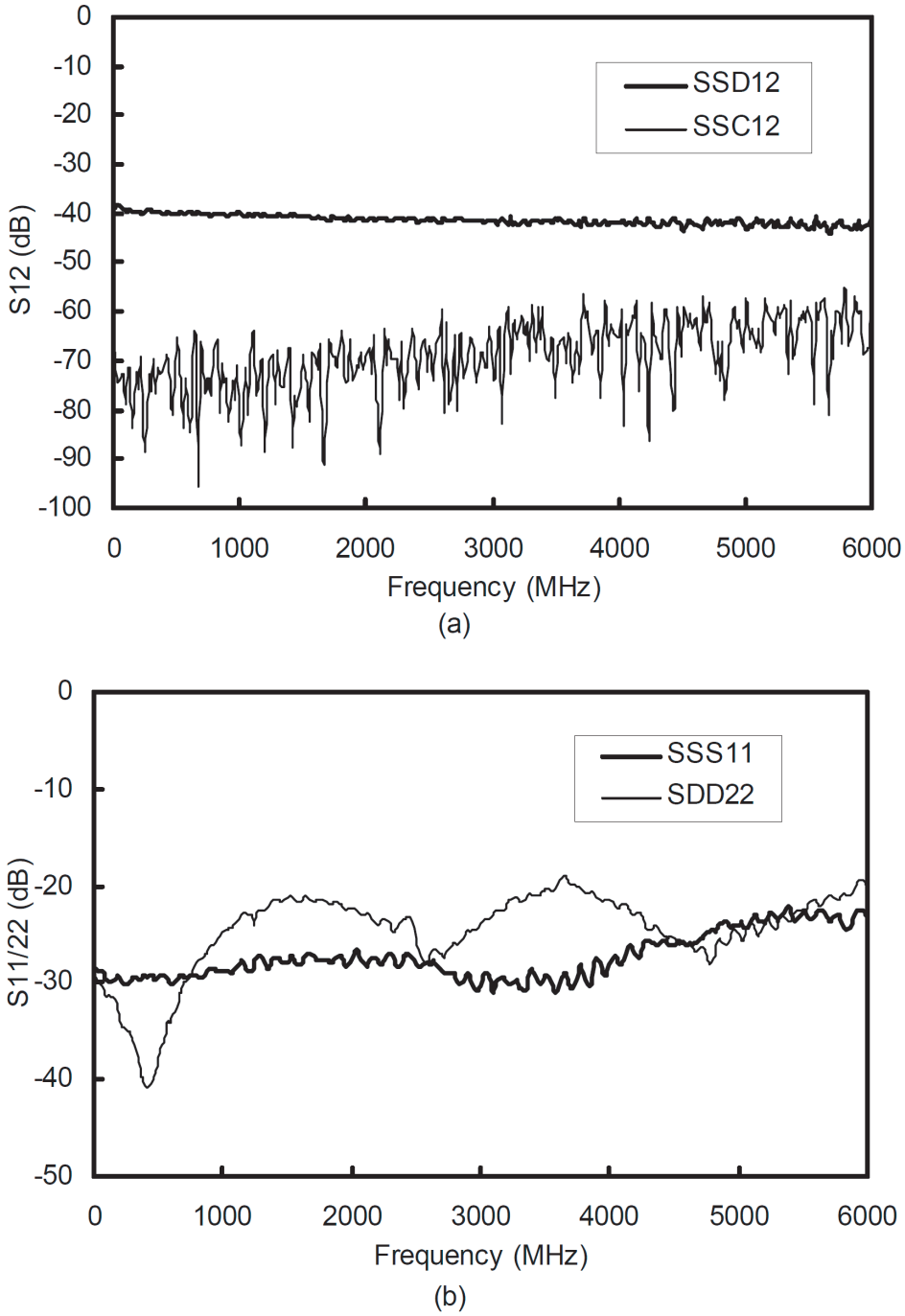

Figure 6.4: Measured mixed-mode S parameters of the proposed ROF link without EDFA, (a) transmission characteristics and (b) reflection characteristics.

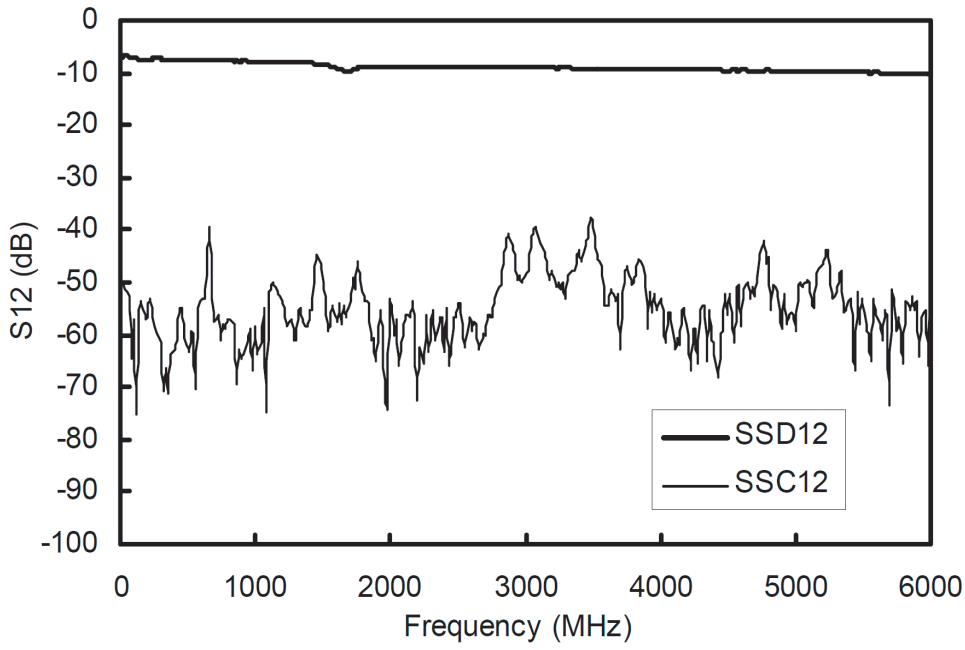

(a)

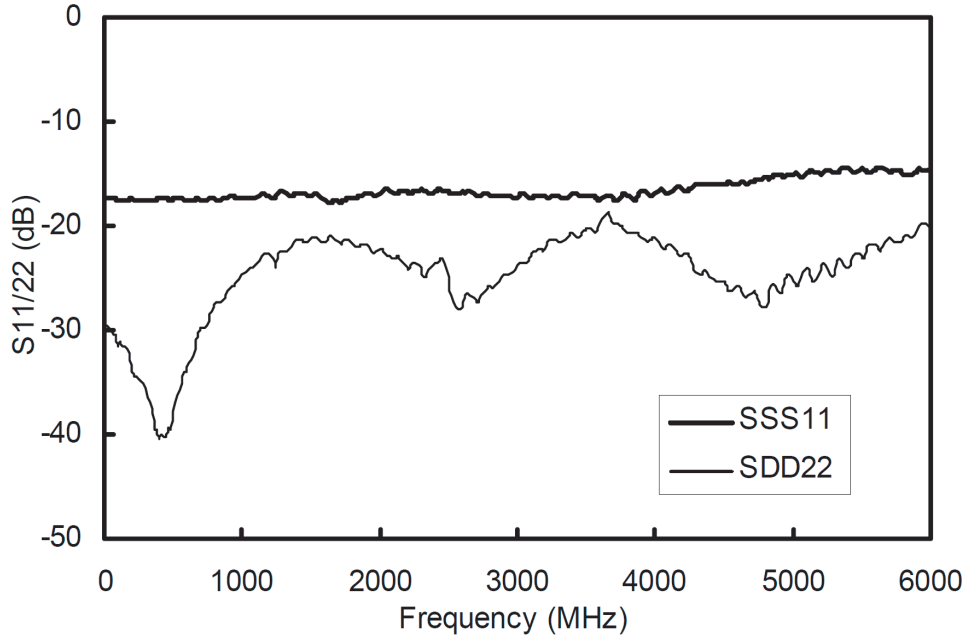

(b)

Figure 6.5: Measured mixed-mode S parameters of the proposed ROF link with EDFA, (a) transmission characteristics and (b) reflection characteristics (received optical power at PD = +19 dBm).

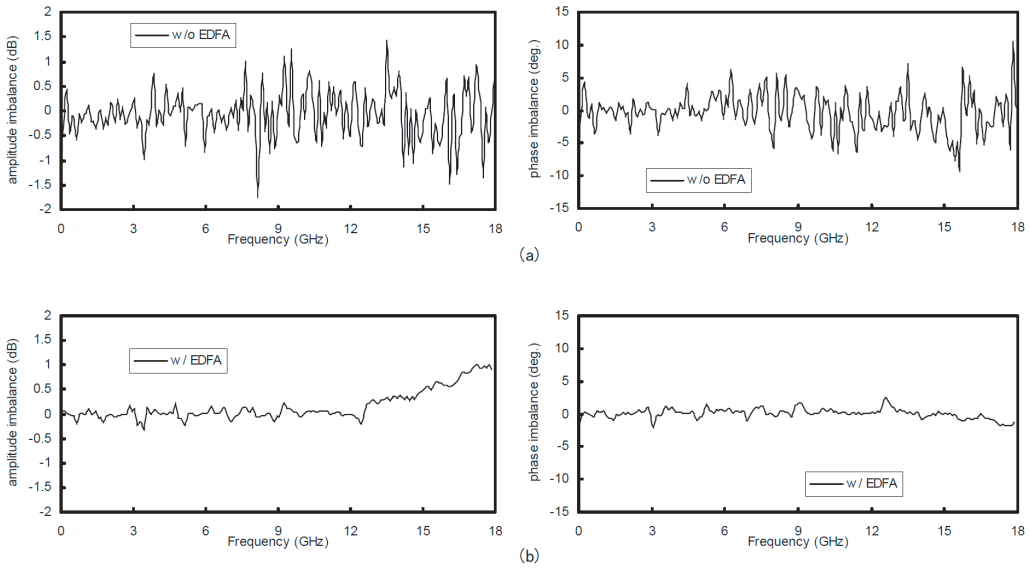

Figure 6.6: Measured imbalances of the proposed RoF link employing UTC-PD, (a) without EDFA and (b) with EDFA.

due to the insertion of EDFA, so the insertion losses are 8±2 dB from 20 MHz to 6 GHz. As is expected, the increase of S_{SC12} is suppressed (not equal to that of S_{SD12}), so CMRR is improved and is more than 30 dB.

As is observed in Fig.6.5(b), S_{SS11} is degraded by the addition of EDFA. But the return loss is still more than 14 dB so it is enough for normal operation. It is supposed that the degradation of S_{SS11} is caused by the increase of received light power at UTC-PD, and is investigated in Section 6.4. S_{SS22} is not changed by the addition of EDFA.

In order to investigate the performances at higher frequency range, S marameters were measured by the single-ended network analyzer from 50 MHz to 18 GHz. The input port shown in Fig.6.2 is used as ports 2 and 3, in this measurement. Figure 6.6 shows the measured amplitude imbalance (S_{12} [dB] - S_{13} [dB]) and phase imbalance (S_{12} [degree] - S_{13} [degree] - 180). Fig.6.6(a) is for RoF link without EDFA and Fig.6.6(a) is for RoF link with EDFA. The imbalances ±1.0 dB and ±5 degrees without EDFA are improved by the addition of EDFA to imbalances ±0.3 dB and ±3 degrees. It is supposed that these imbalances are improved due to the reduction of noises of S_{SC12} by the addition of EDFA. In other word, we can say that CMRR improvement shown in Fig.6.4 is caused by the improvement of the imbalances by the addition of EDFA. In 6-18 GHz, the imbalances ±1.8 dB and ±11 degrees without EDFA are improved by the addition of EDFA to imbalances ±1.1 dB and ±3 degrees. So we can say that the improvement by the additon of EDFA is observed when frequency is higher than 6 GHz. The imbalance with EDFA in 6-18 GHz is better

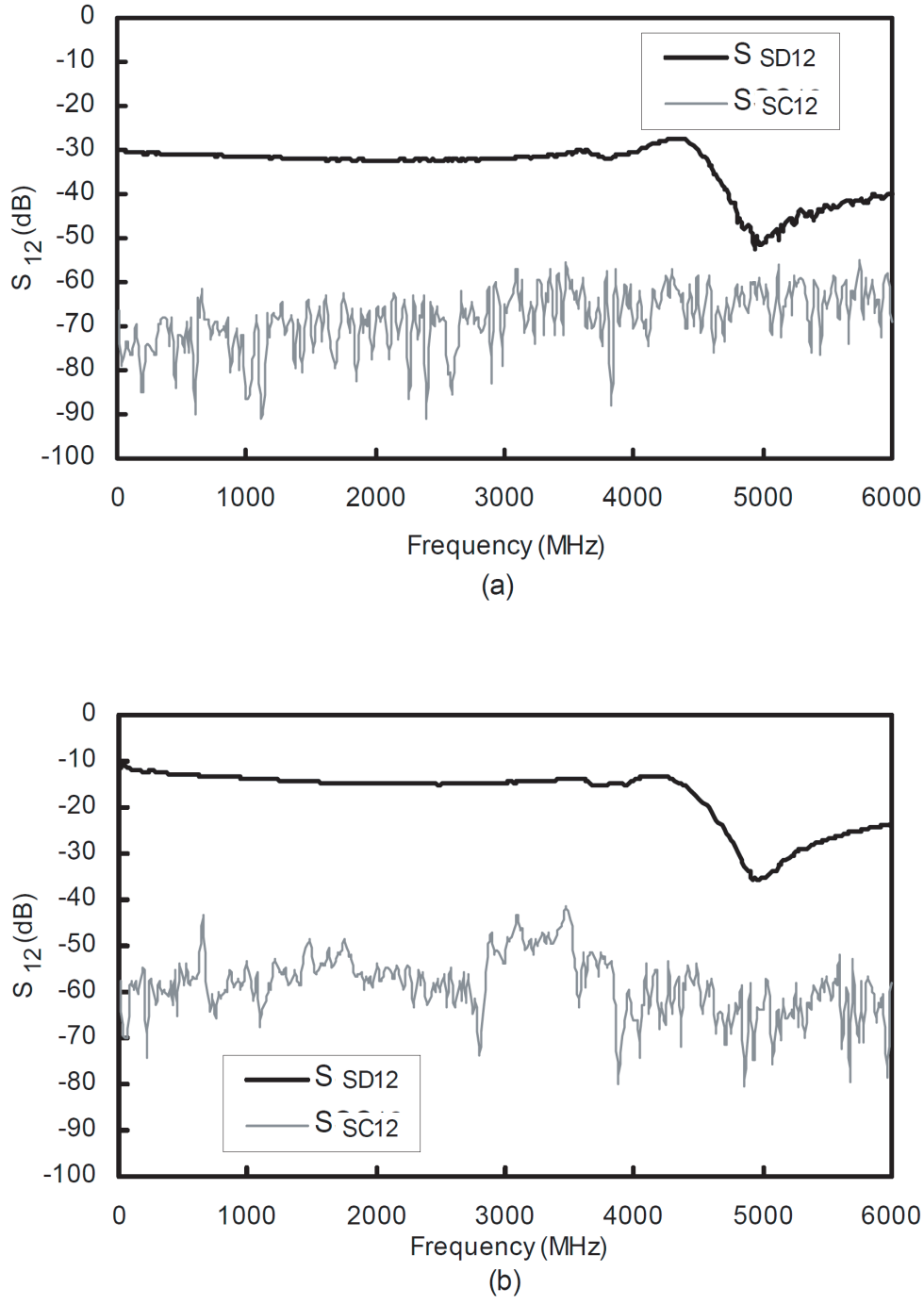

Figure 6.7: Measured mixed-mode S parameters of the proposed RoF link employing PIN-PD, (a) without EDFA and (b) with EDFA.

than imbalance without EDFA under 6 GHz, so it is supposed that the RoF link with EDFA can achieve CMRR $\geq$ 15 dB in 6-18 GHz range.

6.3.2 RoF Link employing PIN-PD

Figure 6.7 shows the measured mixed-mode S parameters of the proposed RoF link employing UTC-PD. Figure 6.7(a) is without EDFA (received light power at PD is +10 dBm) and Fig.6.7(b) is with EDFA, respectively. The bandwidth of the PD employed is upto around 4.5 GHz. However, its performances (insertion loss $\approx$ 30 dB, CMRR $\geq$ 30 dB) without EDFA is better than those employing UTC-PD without EDFA. The reason to this difference is supposed that the conversion efficiency of PIN-PD (0.85 mA/mW) is greater than that of UTC-PD (0.55 mA/mW). When employing EDFA, the insertion loss is improved to around 15 dB, but CMRR is almost same level to that without EDFA. The reason to this constant CMRR is supposed that the noise caused by PIN-PD is less than the relative intensity noise caused by other components. So, when employing PIN-PD, EDFA is not mandatory and RF amplifier after PIN-PD will be practical. S_{SS22} is not changed by the addition of EDFA, same as in case of UTC-PD. S_{SS11} is around -1 dB so matching is not in good condition, because the load impedance attached to PIN-PD is selected to 1 kohms (in order to obtain higher output power). The reflection performance will be described in detail in Section 6.4, including the effect of the change of received light power.

6.4 Optimization of Received Light Power at Photo Diode

As described in the previous Section, increasing the received light power at the UTC-PD is an effective way of improving CMRR and insertion loss, but the cost is a degradation in return loss at port 1. In order to find the optimum received light power at UTC-PD, mixed-mode S parameters were measured for different EDFA output powers. Same measurements were done for RoF link employing PIN-PD, and the optimum received light power will be discussed.

6.4.1 RoF Link employing UTC-PD

Figure 6.8 shows measured S_{SD12} versus received light power at UTC-PD. Six frequency points (0.66G, 1.46G, 2.86G, 3.48G, 4.76G and 5.22 GHz) were sampled from Fig.6.4(b). These frequency points were selected because S_{SC12} peaks at these frequencies in Fig.6.4(b), and thus the values represent the worst CMRR (refer to Fig.6.9). From Fig.6.8, we can find that S_{SD12} increases when received light power rises up to +18 dBm. However, when the power exceeds +20 dBm, S_{SD12} falls quickly. So the minimum insertion losses are obtained with received light powers from +18 dBm to +20 dBm.

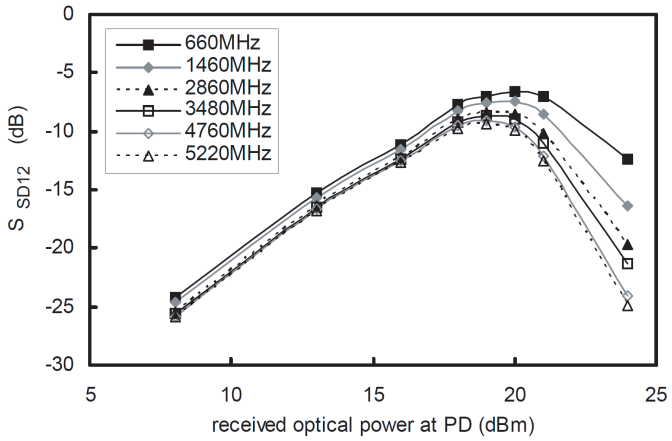

Figure 6.8: Measured S_{SD12} versus received optical power at PD (employing UTC-PD).

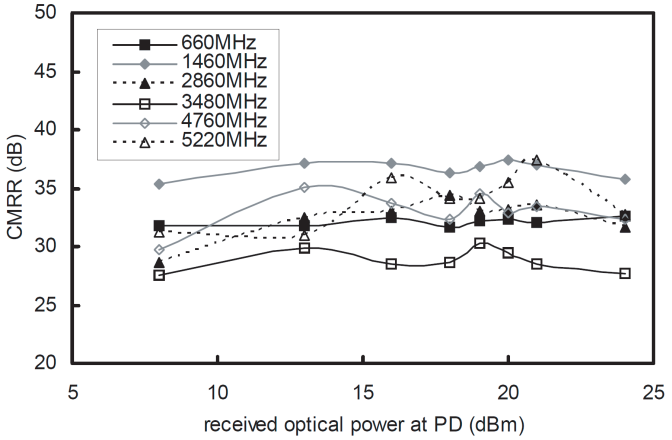

Figure 6.9: Measured CMRR versus received optical power at PD (employing UTC-PD).

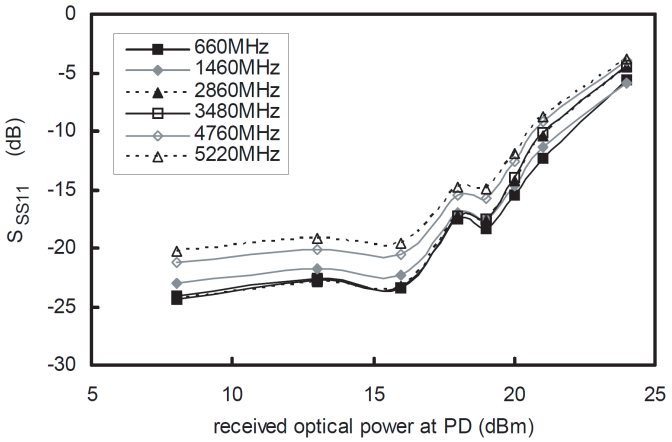

Figure 6.10: Measured S_{SS11} versus received optical power at PD (employing UTC-PD).

The measured CMRR versus received light power is shown in Fig.6.9. Fig.6.9 is slightly complicated as S_{SC12} contains noise, as shown in Fig.6.4(b). However, we can say that CMRR is almost constant against received light power from +13 dBm to +24 dBm. When received light power decreases from +13 dBm, CMRR also decreases as the noise caused by UTC-PD starts to be dominant.

Measured S_{SS11} versus received light power is shown in Fig.6.10. Figure 6.10 shows that S_{SS11} is almost constant when received light power is under +16 dBm. When the power increases over +16 dBm, S_{SS11} increases quickly. It is supposed that this increase of S_{SS11} is caused by the saturation of UTC-PD. So, the received light power must be limited to +19 dBm if return loss must be greater than 14 dB.

Overall, received light power at UTC-PD of around +19 dBm is optimum to terms of less insertion loss, large CMRR, and large return loss. The measured results shown in Fig.6.4(b) satisfy this condition. It is supposed that this optimum received light power depends on the types of PD, so same measurements were done using the RoF link employing PIN-PD.

6.4.2 RoF Link employing PIN-PD

Figure 6.11 shows measured S_{SD12} versus received light power at UTC-PD. Six frequency points (0.66G, 1.46G, 1.76G, 2.88G, 3.1G and 4.28 GHz) were sampled from Fig.6.7(b), same as in Fig.6.11. These frequency points were selected because S_{SC12} peaks at these frequencies in Fig.6.7(b), under 4.5 GHz of PIN-PD's bandwidth. From Fig.6.11, we can find that S_{SD12} increases when received light power rises up to +10 dBm. However, when the power exceeds +10 dBm, S_{SD12} falls quickly. So the minimum insertion losses are obtained with output powers from +8 dBm to +10 dBm.

The measured CMRR versus received light power is shown in Fig.6.12. Fig.6.12 is slightly complicated as S_{SC12} contains noise, same as in Fig.6.9. However, we can say that CMRR is almost constant against received light power from +3 dBm to +11 dBm. When received light power decreases from +3 dBm, CMRR also decreases as the noise caused by PIN-PD starts to be dominant. And only in the case of PIN-PD, when the power exceeds +11 dBm, S_{SD12} falls quickly.

Measured S_{SS11} versus received light power is shown in Fig.6.13. As is described in Section 6.3, impedance of used PIN-PD is not matched to 50 ohms, so the return loss is around 1 - 2 dB. However, it is almost constant when received light power is under +10 dBm. When the power increases over +10 dBm, S_{SS11} decreases quickly. It is supposed that this change of S_{SS11} is caused by the saturation of PIN-PD, same as in UTC-PD. This change is good for impedance matching, however, when the PIN-PD is matched to 50 ohms, the change is not desirable. So, the received light power must be limited to +10 dBm.

Overall, received light power at PIN-PD of around +10 dBm is optimum to terms of less insertion loss, large CMRR, and large return loss. The measured results shown in Fig.6.7(b) satisfy this condition. It is cleared that the optimum received light power

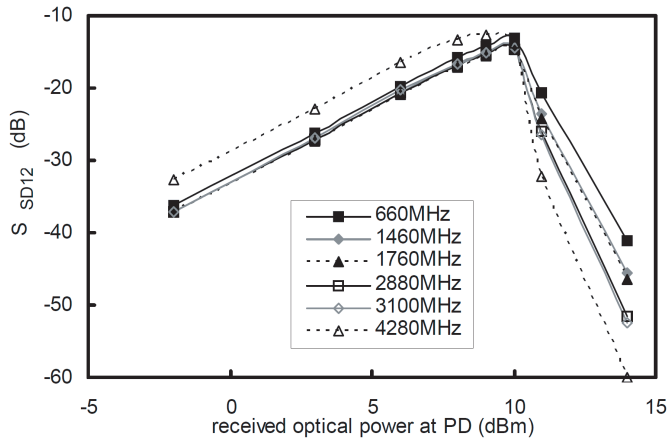

Figure 6.11: Measured S_{SD12} versus received optical power at PD (employing PIN-PD).

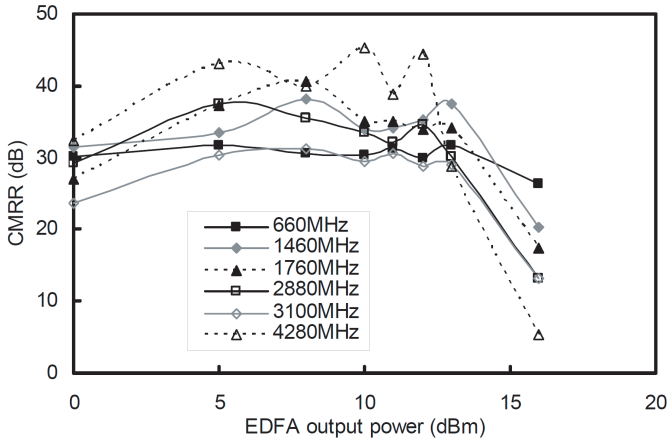

Figure 6.12: Measured CMRR versus received optical power at PD (employing PIN-PD).

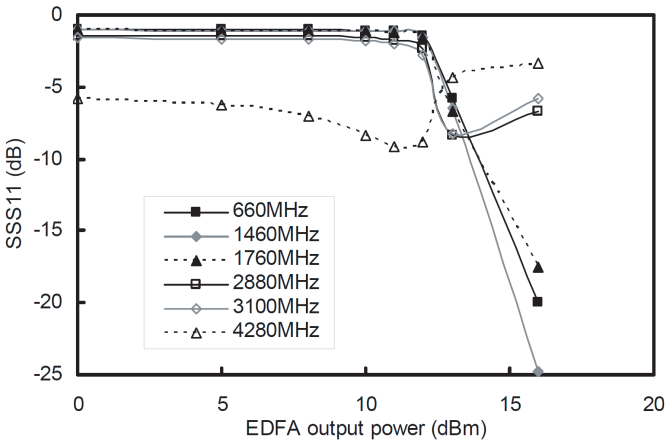

Figure 6.13: Measured S_{SS11} versus received optical power at PD (employing PIN-PD).

deponds on the types of PD.

6.5 Conclusion

We propose to add a dual-drive Mach-Zender modulator to an RoF (radio-over-fiber) link to provide it with wideband balun functionality. Its performance was evaluated in terms of mixed-mode S parameters. The proposed link exhibits CMRR (common mode rejection ratios) of more than 15 dB, return loss of more than 20 dB, and insertion loss of 41±2 dB from 20 MHz to 6 GHz (bandwidth ≈ 199 %) due to the use of microwave photonics technology. An EDFA (erbium doped fiber amplifier) can be employed in order to improve the link's CMRR and insertion loss. With the addition of an EDFA yielded CMRR over 30 dB and insertion loss 8±2 dB. The comparison between measured CMRR upto 6 GHz and measued imbalances upto 18 GHz shows that the proposed link can be used as balun upto 18 GHz. Optimum received light power at the link's photo diode was investigated from the standpoint of insertion loss, CMRR, and return loss. It was found that the received light powers of +19 dBm and +10 dBm are optimum for UTC-PD and PIN-PD, respectively. Due to its wideband properties, the proposed link is expected to be a powerful candidate for RoF systems that support balanced RF circuits and precise antenna measurement systems.

6.6 References

[6.1] W.I.Way, "Optical fiber-based microcellular systems: an overview," IEICE Trans. Commun., vol.E76-B, no.9, pp. 1091-1102, September 1993.

[6.2] H.Al-Raweshidy and S.Komaki, "Raio over fiber technologies for mobile communications networks," Artech House, 2002.

[6.3] N.Taguchi, S.Tanaka, T.Kimura and Y.Atsumi, "Relative-intensity-noise reduction technique for frequency-converted radio-on-fiber system," IEEE Trans. Microwave Theory & Tech., vol.54, no.2, pp.945-950, February 2006.

[6.4] S.Tanaka, N.Taguchi, T.Kimura and Y.Atsumi, "A predistortion type equipath linearizer designed for radio-on-fiber system," IEEE Trans. Microwave Theory & Tech., vol.54, no.2, pp.938-944, February 2006.

[6.5] S.Tanaka, N.Taguchi, T.Kimura and Y.Atsumi, "Distortion reduction filters for radio-on-fiber system," IEICE Trans. Electron., vol.E90-C, no.2, pp.365-372, February 2007.

[6.6] "SAWEP835MCM0F00 data sheet," Murata Manufacturing Co., Ltd., Japan, November 29, 2005.

[6.7] J.Lynch, E.Entchev, B.Lyons, A.Tessmann, H.Massler, A.Leuther and M.Schlechtweg, "Design and analysis of a W-band multiplier chipset," in IEEE MTT-S Int. Microwave Symp. Dig., June 2004, pp.227-230.

[6.8] K.Yamada, S.Horiuchi, S.Tanaka, Y.Yamada and N.Michishita, "Evaluation of electric field distributions in a car," Proc. Int. Symp. Antennas and Propagation, poster conf99a061, November, 2006.

[6.9] C.A.Balanis, "Antenna Theory,"John Wiley & Sons, 1997.

[6.10] A.C.Chen et al, "Development of low-loss broad-band planar baluns using multilayered organic thin filmes," IEEE Trans. Microwave Theory & Tech., Vol.53, No.11, pp.3648-3655, November, 2005.

[6.11] J.L.Corral, J.Marti and J.M.Fuster, "General expressions for IM/DD dispersive analog optical links with external modulation or optical up-conversion in a Mach-Zender electrooptical modulator," IEEE Trans. Microwave Theory & Tech., Vol.49, No.10, pp.1968-1976, October, 2001.

[6.12] D.E.Bockelman and W.R.Eisenstadt, "Combined differential and common-mode analysis of power splitters and combiners," IEEE Trans. Microwave Theory & Tech., Vol.43, No.11, pp.2627-2632, November, 1995.

[6.13] S.Tanaka, N.Taguchi and Y.Atsumi, "A study on wideband balun for radio-on-fiber link with dual-drive Mach-Zender modulator," IEICE Society Conf., C-14-1, p.249, September 2006.

[6.14] J.Reed and J.Wheeler, "A method of analysis of symmetrical four-port networks," IRE Trans. Microwave Theory & Tech., Vol.4, No.5, pp.246-252, October 1956.

[6.15] "TC1-15 data sheet Rev.C," Mini-Circuits, June 21, 2007.

Chapter 7

Conclusions

7.1 Overall Conclusions

Based on the growing demand for multiband/wideband handsets, several analog front-end components with high linearity are proposed in this dissertation. Two groups of analog components are studied; the one covers antennas and switches, the other covers radio-on-fiber (RoF) systems. Current analog front-end components including antennas, switches, divider/combiners, amplifiers and so on, are basically designed to operate at a single frequency with a narrow frequency band. To provide the high linearity needed, this study introduces antenna elements with different widths in a dipole construction to realize wideband antennas, and a multiband pin diode switch that uses a ladder circuit configuration.

Many current analog front-end components are based on non-linear (active) devices and the resulting distortion raises in-band and out-of-band spurious components. Therefore, predistortion type equi-path linearizer and optical/RF comb filters are applied to RoF systems. Also, an RoF link with a dual-drive Mach-Zender modulator as a wideband balan is proposed in order to realize a balanced RF interface at the input. These components can be used together as shown in Fig.1.1, in order to realize software defined radio systems and/or cognitive radio systems.

7.2 Conclusions from Chapter 2

Multiband SPDT switch design and fabrication was discussed for purpose of reducing the cost and increasing the reliability. The switch proposed demostrated isolation greater than 20 dB and insertion loss less than 2 dB at three different frequency bands: 1.6 GHz, 2.5 GHz, and 5.8 GHz. The use of the ladder circuit realizes a simple circuit configuration, the number of frequency bands is not limited to three, and the frequency range is not limited to 1-6 GHz. Simulations that considered the parasitic elements gave good agreement with the measured results. Ten prototype switches were fabricated on the lumped and semi-microstrip model to measure the variation

in switching characteristics for future mass production. Their variation in terms of resonance frequencies was investigated in detail. The semi-microstrip configuration gave quite stable resonance frequencies and the variation width was just 25 % or so of that of the lumped element switch. It was also found by measurements that the ladder circuit configuration did not influence switching speed or signal distortion. The prototypes showed good temperature stability from -30 ℃to +85 ℃. It was also found that the isolation of the multi-band switch can be improved by adding pin diodes without degrading the insertion losses. The switch configuration introduced here may become the key device in implementing bi-directional multi-band automobile communication systems.

7.3 Conclusions from Chapter 3

A folded loop antenna and a planer folded dipole antenna with wideband characteristics were proposed. While both antennas have the same characteristics, the folded loop antenna is suitable for compact applications and the folded dipole antenna is suitable for planer applications. The antennas have simple planar construction without a ground plane and are easy to assemble. Parameters for wideband and compact properties were elucidated by using an electromagnetic simulator based on the method of moments. Experimental results centered at 1.7 GHz for 50 ohm impedance matching show that both antennas have the bandwidth of more than 55 % (VSWR $\leq$ 2). The simulated and experimental results are in good agreement, and the gains of the antenna are almost constant (around 2 dBi) in this frequency band. The radiation patterns are very similar to those of a normal dipole antenna except for the cross polarization components, and it was also shown that the antenna has the self-balanced impedance property in this frequency band.

7.4 Conclusions from Chapter 4

A predistortion type equi-path linearizer was combined with a Fabry-Perot laser diode to create an RoF system based on W-CDMA. IM3 components are improved by over 20 dB in the RF frequency band of more than 60 MHz. The C/N level is not changed by the addition of the linearizer and the RoF link meets the specifications (IM3 $\leq$ -65 dBc and C/N $\geq$ 52 dB) with OMI range from 10 % to 30 %. The proposed configuration exhibits good temperature stability from 10 ℃to 40 ℃with a simple control circuit. It can be said that the improved stability is obtained by increasing the complexity of the RF circuit. However, compared to the feedforward technique (excluding temperature control circuit), the expensive optical portion is reduced and total circuit complexity is about the same. The circuit size of the prototype is quite large, but can be reduced by employing compact couplers and additional phase shifters from the first design stage.

It was also found that the phase difference between the carrier and the IM3 component generated by the non-linearity of the Fabry-Perot and distributed feedback laser diode is shifted by 90 degrees from that of the RF amplifier. This is, to our knowledge, the first report of this phase shift. This 90 degree phase shift was validated in experiments at various RF frequencies, frequency separations, and input powers.

7.5 Conclusions from Chapter 5

Three distortion reduction filters for radio-on-fiber systems were proposed and evaluated in the 2 GHz band. These filters have simple construction as they are composed of all passive components, and can reduce IM3 (spurious) components even in the saturation region, unlike conventional linearizers. The optical comb filter can reduce IM3 components by more than 20 dB and the noise level by around 10 dB, but insertion loss is large and stability against vibration is very poor. The proposed RF comb filter can reduce IM3 components by more than 20 dB and reduce noise by more than 3 dB; its insertion losses are 2 and 10 dB for frequency separations of $\Delta f = 100$ MHz and 5 MHz, respectively. An RF-DBRF for $\Delta f = 100$ MHz can reduce IM3 components by more than 30 dB and noise level by more than 3 dB. These results are summarized in Table 5.1. It can be said that RF-DBRF has the best properties for $\Delta f = 100$ MHz. Frequency deviations in the temperature range of -10 ℃to +50 ℃are within 5 MHz for all filters. The RF comb filter and the RF-DBRF are stable against vibration.

7.6 Conclusions from Chapter 6

A proposal was made to add a dual-drive Mach-Zender modulator to an RoF link to provide it with wideband balun functionality. Its performance was evaluated in terms of mixed-mode S parameters. The proposed link exhibits CMRR (common mode rejection ratios) of more than 15 dB, return loss of more than 20 dB, and insertion loss of 41±2 dB from 20 MHz to 6 GHz (bandwidth ≈ 199 %) due to the use of microwave photonics technology. An EDFA (erbium doped fiber amplifier) can be employed in order to improve the link's CMRR and insertion loss. With the addition of an EDFA, it yielded CMRR of over 30 dB and insertion loss of 8±2 dB. A comparison between measured CMRR up to 6 GHz and measured imbalances up to 18 GHz showed that the proposed link can be used as balun operating up to 18 GHz. Optimum received light power at the link's photo diode was investigated from the standpoint of insertion loss, CMRR, and return loss. It was found that the received light powers of +19 dBm and +10 dBm are optimum for UTC-PD and PIN-PD, respectively.

7.7 Future analog front-end components

The demand for multiband/wideband operation will only continue to increase. One of the candidates for wideband operation is microwave photonics (MWP) technology. As is mentioned in Chapter 6, photonic components have very wide bandwidth. So there is the possibility of extreme wideband operation through the use of MWP technology. The radio-on-fiber system mentioned in Chapters 4, 5, and 6 is an example of MWP applications.

Metamaterial technology is an exciting candidate. In particular, the so called composite right left handed (CRLH) construction offers non linear dispersion (phase) characteristics. Applying CRLH construction will yield compact and multiband/wideband components.

Of course, advances in micro electro mechanical system (MEMS) will also produce new types of analog front-end components. For applications such as switches, MEMS devices have started to exhibit extremely good performance. So, these three techniques and their combination will produce next-generation analog front-end components in the near future, and accelerate the use of software defined radio and/or cognitive radio systems.

Acknowledgments

I greatly thank many people for their support and assistance of my studies. First and foremost, I would like to express my deep gratitude to Professor Masao Nakagawa for his valuable advice and useful discussion, since I joined his laboratory in 1989. His unfailing support made me possible to accomplish this work.

I would also like to thank my thesis committee members, Professor Iwao Sasase, Professor Tadahiro Kuroda and Associate Professor Yukitoshi Sanada of Keio University for their helpful discussion, suggestions, and careful and critical reading of this dissertation.

I would like to express my thanks to Professor Hisashi Morishita, National Defense Academy, for his useful advice and favorable encouragement in my research on antennas and switches. I also thank Professor Yoshihide Yamada, National Defense Academy, and Professor Kazuhiro Hirasawa, Tokyo University of Agriculture and Technology, for their constructive discussions. Past and present members in Morishita Laboratory helped me in my fabricating and measuring antennas. Especially, I would like to thank Dr.Shogo Hayashida, Mr.Yongho Kim, Mr.Jun Ito, and Mr.Masao Sakuma.

I am pleased to acknowledge many individuals who helped me constantly in my research in Microwave Technology Research Department of Yazaki Research and Technology Center; Dr.Kunio Hashimoto, Senior Managing Executive Officer, Mr.Kazuharu Tsuchiya, General Manager, Mr.Yasunori Atsumi, Leader, Mr.Tsuneto Kimura, Leader, Mr.Yoichi Ido, Leader, and Mr.Hiroshi Miyamoto, Leader. I also very thank my colleagues; Mr.Noritaka Taguchi, Mr.Satoru Horiuchi, Dr.Shusuke Narieda, Mr.Kunihiko Yamada and many others.

Finally, I would like to express special thanks to my grandparents, my parents and my wife for supporting, encouraging and leading me to establish this study in Keio University with the glorious history longer than 150 years.

Appendix A

List of Papers by Author

A.1 Transaction Papers

[1] S.Tanaka, S.Hayashida, H.Morishita, and Y.Atsumi, "Wideband and compact folded loop antenna," IEE Electron. Letters, Vol.41, No.17, pp.945-946, August 18, 2005.

[2] S.Tanaka, N.Taguchi, T.Kimura and Y.Atsumi, "A predistortion type equi-path linearizer designed for radio-on-fiber system," IEEE Trans. Microwave Theory & Tech., vol.54, no.2, pp.938-944, February 2006.

[3] S.Tanaka,S.Horiuchi, T.Kimura and Y.Atsumi, "Design and fabrication of multi-band p-i-n diode switches with ladder circuits," IEEE Trans. Microwave Theory & Tech., vol.54, no.4, pp.1561-1568, April 2006.

[4] S.Tanaka, N.Taguchi, T.Kimura and Y.Atsumi, "Distortion reduction filters for radio-on-fiber system," IEICE Trans. Electron., vol.E90-C, no.2, pp.365-372, February 2007.

[5] S.Tanaka, N.Taguchi and Y.Atsumi,"Evaluation of wideband balun for radio-on-fiber system with dual-drive Mach-Zehnder modulator," IEICE Trans. Electron., vol.J91-C, no.1, pp.111-118, January 2008 (in Japanese).

[6] S.Tanaka, Y.Kim, H.Morishita, S.Horiuchi, Y.Atsumi and Y.Ido,"Wideband planar folded dipole antenna with self-balanced impedance property," IEEE Trans. Antenna & Propagation, vol.56, no.5, pp.1223-1228, May 2008.

A.2 Other Related Papers

[1] T.Mori, A.Kajiwara, S.Tanaka and M.Nakagawa, "Optimum channel threshold for DS/SSMA single-hop packet radio network with channel load sensing," IEICE Trans. Commun., vol.J75-B-II, no.1, pp.10-16, January 1992 (in Japanese).

[2] S.Tanaka, K.Ogawa, H.Yasuda, H.Yamashima, R.Kumagai, N.Kaneko, and T.Yoshizawa, "Outline of the new EMC center and EMC-related activities," Yazaki Technical Report, No.22, pp.73-77, December, 2000 (in Japanese).

[3] N.Taguchi, S.Tanaka, T.Kimura and Y.Atsumi, "Relative-intensity-noise reduction technique for frequency-converted radio-on-fiber system," IEEE Trans. Microwave Theory & Tech., vol.54, no.2, pp.945-950, February 2006.

[4] S.Horiuchi, K.Yamada, S.Tanaka, Y.Yamada and N.Michishita, "Comparisons of simulated and measured electric field distributions in a cabin of simplified scale car model," IEICE Trans. Commun., vol.E90-B, no.9, pp.2408-2415, September 2007.

A.3 International Conferences

[1] S.Tanaka and T.Kimura, "A pin diode switch operating at multi-frequency bands," 2004 IEEE MTT-S Int. Microwave Symp. Dig. (IMS), pp.1129-1132, June 2004.

[2] S.Tanaka, S.Yuminaga and T.Kimura, "On-board multi-layered microstrip antenna and associated RF circuits for multiple ITS applications," Proc. 11th World Congress on Intelligent Transport Systems (ITS), IS01, No.3059, October 2004.

[3] N.Taguchi, S.Tanaka, T.Kimura and Y.Atsumi, "Frequency Multiplexing Technique for Relative-Intensity-Noise Reduction," in OFC2005, Dig., Paper OThN4.

[4] S.Tanaka, N.Taguchi, T.Kimura and Y.Atsumi, "A predistortion type equipath linearizer designed for radio-on-fiber system," 2005 IEEE MTT-S Int. Microwave Symp. Dig. (IMS), TU1A-4, pp.15-18, June 2005.

[5] N.Taguchi, S.Tanaka, T.Kimura and Y.Atsumi, "Relative-Intensity-Noise Reduction Technique for Frequency-Converted Radio-on-Fiber System," 2005 IEEE MTT-S Int. Microwave Symp. Dig. (IMS), TU1A-6, pp.23-26, June 2005.

[6] S.Tanaka, N.Taguchi, T.Kimura and Y.Atsumi, "Frequency-tunable PIN diode switch for software defined radio," Proc. 35th European Microwave Conf. (EuMC), pp.1771-1774, October 2005.

[7] S.Tanaka, N.Taguchi, T.Kimura and Y.Atsumi, "Distortion canceller for radio-on-fiber link employing comb filter," 1st Asia-Pacific Microwave Photonics Conference (AP-MWP), L-5, pp.366-369, April 2006.

[8] S.Tanaka, Y.Kim, A.Matsuzaki, S.Hayashida, H.Morishita, Y.Atsumi and Y.Ido, "Wideband folded loop and folded dipole antennas," Proc. IEEE Antennas and Propagarion Society Int. Symp. (AP-S), pp.3711-3714, July 2006.

[9] N.Taguchi, S.Tanaka, T.Kimura and Y.Atsumi, "Distortion wvaluation of frequency-converted radio-on-fiber system employing RIN reduction technique," Int. Topical Meeting on Microwave Photonics (MWP), P36,October 2006.

[10] K.Yamada, S.Horiuchi, S.Tanaka, Y.Yamada and N.Michishita, "Evaluation of electric field distributions in a car," Proc. Int. Symp. on Antennas and Propagations (ISAP), poster, November 2006.

[11] S.Tanaka and H.Morishita, "Folded loop antenna and folded dipole antenna with wideband characteristics," Progress in Electromagnetics Research Symp. (PIERS), 3P3, p.1373, March 2007.

[12] S.Tanaka, Y.Kim and H.Morishita, "Folded loop antenna and folded dipole antenna with wideband properties," EMTS 2007, Int. URSI Commission B - Electromagnetic Theory Symposium, Session 05-62, EMTS52, July 2007.

[13] S.Tanaka, Y.Kim, H.Morishita, S.Horiuchi and Y.Atsumi, "Wideband and miniaturized triangular folded dipole antenna," Proc. Int. Symp. on Antennas and Propagations (ISAP), 2A4-4, pp.286-289, August 2007.

[14] S.Horiuchi, S.Tanaka, Y.Yamada and Y.Atsumi, "Design of a dual resonance folded dipole antenna in on-glass use," Proc. Int. Symp. on Antennas and Propagations (ISAP), No.1645037, October 2008.

[15] S.Narieda, S.Tanaka, Y.Ido, Y.Atsumi, A.Sanada and H.Kubo, "Planar dual-band omni-directional UHF antennas employing a composite right/left-handed double-sided metal layer structure," 2009 IEEE Radio & Wireless Symp. Dig. (RWS), January 2009 (to be published).

A.4 Technical Reports and Other Presentations (in Japanese)

[1] S.Tanaka, N.Taguchi, T.Kimura, K.Takahashi, M.Hirayama, M.Hamaguchi, Y.Iguchi and H.Kanno, "Radio on fiber equipment for IMT-2000," IEICE General Conf., B-10-153, p.590, March 2002.

[2] S.Tanaka, N.Taguchi, T.Kimura and M.Hirayama, "A study on influence of diode linearizer on IM5 and CTB," IEICE Society Conf., C-2-28, p.50, September 2002.

[3] S.Tanaka and T.Kimura, "A study on triplexer for three frequencies operation antenna," IEICE General Conf., C-2-41, p.73, March 2003.

[4] N.Taguchi and S.Tanaka, "A study on radio on fiber equipment for IMT-2000 with feedforward linearization," IEICE General Conf., C-14-10, p.341, March 2003.

[5] S.Tanaka and T.Kimura, "A study on pin diode switch with multi isolated frequency points," IEICE Society Conf., C-2-4, p.28, September 2003.

[6] N.Taguchi and S.Tanaka, "A study on frequency-converted ROF system using nonlinearity of FP-LD," IEICE Society Conf., C-14-1, p.330, September 2003.

[7] S.Tanaka, K.Yamada and N.Taguchi, "A trial of postdistortion type phase-shifted linearizer," IEICE Society Conf., C-2-10, p.26, September 2004.

[8] S.Tanaka and N.Taguchi, "Fabry-Perot laser diode linearized by predistortion type equi-path linearizer," IEICE Society Conf., C-14-6, p.304, September 2004.

[9] N.Taguchi and S.Tanaka, "Reduction of the optically reflected intensity noise by the simultaneous transmission of IF and LO," IEICE Society Conf., C-14-7, p.305, September 2004.

[10] S.Tanaka, N.Taguchi, T.Kimura and Y.Atsumi, "A study on frequency-tunable pin diode switch for SDR," IEICE General Conf., C-2-41, p.74, March 2005.

[11] S.Horiuchi, S.Tanaka, Y.Ido and Y.Atsumi, "Dual-band pin diode switch for WLAN," IEICE General Conf., C-2-42, p.75, March 2005.

[12] N.Taguchi and S.Tanaka, T.Kimura and Y.Atsumi, "RIN reduction by the simultaneous transmission of IF and LO under multi-reflection," IEICE General Conf., C-14-8, p.353, March 2005.

[13] S.Tanaka, S.Hayashida, H.Morishita and Y.Atsumi, "Wideband and compact folded loop antenna," IEICE Technical Report., AP2005-71, pp.37-42, September 8, 2005.

[14] S.Tanaka, N.Taguchi, T.Kimura and Y.Atsumi, "A trial of distortion canceller for ROF employing optical comb-filter," IEICE Society Conf., C-14-1, p.327, September 2005.

[15] N.Taguchi and S.Tanaka, T.Kimura and Y.Atsumi, "Distortion characteristics by the simultaneous transmission of IF and LO for RIN reduction," IEICE Society Conf., C-14-2, p.328, September 2005.

[16] S.Tanaka, N.Taguchi, T.Kimura and Y.Atsumi, "A study on predistortion type equi-path linearizer designed for radio-on-fiber system," IEICE Technical Report., MWP2005-10, pp.51-56, November 21, 2005.

[17] S.Tanaka, N.Taguchi, T.Kimura and Y.Atsumi, "A predistortion type equi-path linearizer for radio-on-fiber link and phase characteristics of 3rd order distortion components in laser diodes," IEICE Technical Report., MWP2005-20, pp.47-52, January 27, 2006.

[18] N.Taguchi and S.Tanaka, T.Kimura and Y.Atsumi, "Relative-intensity-noise reduction technique for radio-on-fiber system," IEICE Technical Report., MWP2005-21, pp.53-60, January 27, 2006.

[19] S.Horiuchi, K.Yamada, S.Tanaka, Y.Yamada, N.Michishita and T.Toba, "Evaluation methods for electric field distribution in a car," IEICE General Conf., B-1-179, p.179, March 2006.

[20] S.Horiuchi, K.Yamada, S.Tanaka, Y.Yamada, N.Michishita and T.Toba, "Evaluation methods for electric field distribution in a car," IEICE Technical Report., AP2006-42, pp.19-24, July 6, 2006.

[21] S.Tanaka, N.Taguchi and Y.Atsumi, "A study on wideband balun for radio-on-fiber link with dual-drive Mach-Zender modulator," IEICE Society Conf., C-14-1, p.249, September 2006.

[22] N.Taguchi and S.Tanaka and Y.Atsumi, "Distortion evaluation of radio-on-fiber system employing RIN reduction technique by the simultaneous transmission of LO," IEICE Technical Report., MWP2006-16, pp.39-44, November 20, 2006.

[23] S.Tanaka, N.Taguchi and Y.Atsumi, "Distortion Canceller for Radio-on-Fiber Link Employing Comb Filter," IEICE Technical Report., MWP2006-17, pp.45-50, November 20, 2006.

[24] S.Horiuchi, S.Tanaka, Y.Yamada and Y.Atsumi, "Improvement of wideband folded dipole antenna for on-glass application," IEICE Society Conf., B-1-52, p.52, September 2007.

[25] S.Tanaka, N.Taguchi and Y.Atsumi, "Wideband balun for radio-on-fiber system with dual-drive Mach-Zehnder modulator," IEICE Technical Report., MWP2007-16, pp.35-40, December 3, 2007.

[26] S.Horiuchi, S.Tanaka, Y.Yamada and Y.Atsumi, "Dual resonance folded dipole antenna for digital television," IEICE Technical Report., AP2007-145, pp.135-140, January 24, 2008.

[27] S.Tanaka, S.Horiuchi, H.Miyamoto and Y.Atsumi, "A study on wideband switch with transmission line between pin diodes," IEICE General Conf., C-2-2, March 2008.

A.5 Patents

[1] Shingo Tanaka and Satoru Horiuchi, "On-vehicle communication system and layout mothod of on-vehicle antenna," Publication number 2003-264415, September 19, 2003.

[2] Shingo Tanaka, "Distortion compensation circuit using diode linearizer," Publication number 2004-343296, December 2, 2004.

[3] Shingo Tanaka, "Signal transmission line and designing method therefore," Publication number 2004-363535, December 24, 2004.

[4] Shingo Tanaka, "Feedforward amplifier circuit," Publication number 2004-364106, December 24, 2004.

[5] Shingo Tanaka, "Predistortor and presidtortion linearizer system using it," Publication number 2005-020379, January 20, 2005.

[6] Shingo Tanaka, "Distortion compensation circuit using diode linearizer," Publication number 2005-073010, March 17, 2005.

[7] Shingo Tanaka, "Distortion compensation circuit using diode linearizer," Publication number 2005-073010, March 17, 2005.

[8] Shingo Tanaka, "High frequency switching circuit, on-vehicle communication system using the same, and band width adjustment method for the same," Publication number 2005-102139, April 14, 2005.

[9] Shingo Tanaka, "Design method for predistortion linearizer system," Publication number 2006-074544, March 16, 2006.

[10] Shingo Tanaka, "Method for compensating distortion of laser diode," Publication number 2006-237029, September 7, 2006.

[11] Shingo Tanaka, "Post-distortion linearizer," Publication number 2006-237671, September 7, 2006.

[12] Shingo Tanaka, "High frequency switching circuit," Publication number 2006-245996, September 14, 2006.

[13] Shingo Tanaka and Satoru Horiuchi, "High frequency switching circuit," Publication number 2007-049665, February 22, 2007.

[14] Yamada Yoshihide, Yamada Kunihiko, Satoru Horiuchi and Shingo Tanaka, "Electric field estimation apparatus," Publication number 2007-240175, September 20, 2007.

[15] Satoru Horiuchi and Shingo Tanaka, "High frequency switching circuit," Publication number 2007-274241, October 18, 2007.

[16] Shingo Tanaka and Noritaka Taguchi, "Balun," Publication number 2008-60681, March 13, 2008.

[17] Shingo Tanaka and Satoru Horiuchi, Not yet published, Application number 2006-313745, November 21, 2006.

[18] Shingo Tanaka and Satoru Horiuchi, Not yet published, Application number 2007-104513, April 12, 2007.

[19] Shingo Tanaka, Not yet published, Application number 2007-167524, June 26, 2007.

[20] Shingo Tanaka and Satoru Horiuchi, Not yet published, Application number 2008-060156, March 10, 2008.

[21] Shingo Tanaka and Satoru Horiuchi, Not yet published, Application number 2008-091997, March 31, 2008.

[22] Satoru Horiuchi and Shingo Tanaka, Not yet published, Application number 2008-181267, July 11, 2008.

[23] Shusuke Narieda and Shingo Tanaka, Not yet published, Application number 2008-181268, July 11, 2008.